A Cylindrical Cavity Resonator System for Characterisation of Hydrogen Gas

Anna Mathea Skar

Thesis for the degree of Master of Science (M.Sc.) in Ocean Technology
Measurement Technology and Instrumentation

Department of Physics and Technology
University of Bergen

June 2024

Abstract

This work presents the development of a high-pressure sensor system designed specifically for assessing hydrogen quality. The sensor system is based on a cylindrical cavity resonator which utilises microwaves to measure resonance frequency within the cavity. This enables the derivation of the dielectric constant which depends on the gas composition, temperature, pressure, and gas density. The purpose is to determine whether this type of measurement system can be used to determine impurities in gases, specifically on hydrogen.

The design of the cylindrical resonator cavity is grounded in theoretical principles and informed by previous research. Despite inherent limitations, a high-pressure sensor system was conceptualised, constructed, and tested quantitatively. The system underwent hydrostatic pressure testing up to 75 bar to ensure its suitability for high-pressure environments. Subsequently, it was measured quantitatively with nitrogen (N_2), carbon dioxide (CO_2), and a N_2/CO_2 mixture with a 0.8/0.2 ratio at room temperature under pressures up to 50 bar. Two measurement series were conducted, with a frequency range of 5-12 GHz in the first, and 5-9 GHz in the second.

The resonance frequencies were found for each gas at each pressure point. In calculating the measured dielectric constant, the N_2 served as a reference gas for the sample gases, CO_2 and the N_2/CO_2 mixture. The dielectric constant was found for the sample gases, concluding with an approximate uncertainty of $\pm 4 \times 10^{-4}$ for lower-order frequency modes, and $\pm 2 \times 10^{-4}$ for higher-order frequency modes.

The aim of these gas assessments is to provide a versatile framework applicable to hydrogen and its impurities. Impurities in hydrogen may originate from the production processes, or occur along the processing or transportation phases. Therefore, this research harbours potential applications in validating hydrogen quality throughout the hydrogen supply chain. This study contributes to advancing methodologies for assessing and maintaining hydrogen purity in critical industrial applications.

Acknowledgements

I would like to extend my sincerest gratitude to my supervisors, Kjetil Folgerø at the Norwegian Research Center (NORCE) and Camilla Sætre at the University of Bergen, for their excellent expertise, guidance, and encouragement throughout this journey.

A special thanks to Roald Langøen in the workshop in the Department of Physics and Technology for his collaborative efforts and skillful construction of the measurement cell utilised in my master's work.

My appreciation also goes to everyone at NORCE for welcoming me into their community, showing engagement and support. I am particularly grateful to Daniel Lie Carlsen and Morten Gunnar Aarra for sharing their specialised knowledge in the hydrogen lab, and to Frank Ådland for his assistance.

I sincerely thank UiBchat for the timely assistance and essential resources that have significantly supported both the research and composition phases of this master's thesis.

I am thankful for the insightful reviews and comments on this work from my classmates Mads, Gunnar, and Elias. Moreover, my appreciation extends to the entire Ocean Technology class of 2024 for some very memorable five years spent studying together.

Lastly, thanks to my family and friends for their support, encouragement, stress relief, and the occasional PC resuscitation in times of need.

Anna Mathea Skar
Bergen, 03.06.2024

Contents

List of Figures

List of Tables

List of Symbols

A_p	constant related to microwave power in a waveguide with TE_{niq} mode
A_ε	first virial Clausius-Moretti coefficient
a	cylinder internal radius [m]
$\mathbf{B}$	magnetic flux density vector [A/m]
B_{hp}	half-power bandwidth [Hz]
B_p	constant related to microwave power in a waveguide with TM_{niq} mode
b_ε	second virial Clausius-Moretti coefficient
C_1, C_2	mode-dependent complex constants
c	speed of light [m/s]
c_0	speed of light in vacuum [m/s]
c_ε	third virial Clausius-Moretti coefficient
$\mathbf{D}$	electric displacement vector [V/m]
d	cylinder cavity thickness [m]
$\mathbf{E}$	electric field strength vector [V/m]
$\mathbf{E}_r$	radial component of electric field strength [V/m]
$\mathbf{E}_T$	transverse component of electric field strength [V/m]
$\mathbf{E}_z$	axial component of electric field strength [V/m]
$\mathbf{E}_\phi$	tangential component of electric field strength [V/m]
f	frequency [Hz]
f_c	cut-off frequency [Hz]
f_d	relaxation frequency [Hz]
f_m	measured resonance frequency [Hz]
f_r	resonance frequency [Hz]
f_t	theoretical resonance frequency [Hz]

$\mathbf{H}$	magnetic field strength vector [A/m]
$\mathbf{H}_r$	radial component of magnetic field strength [A/m]
$\mathbf{H}_T$	transverse component of magnetic field strength [A/m]
$\mathbf{H}_z$	axial component of magnetic field strength [A/m]
$\mathbf{H}_\phi$	tangential component of magnetic field strength [A/m]
i	number of changing periods in r-direction
$\mathbf{J}$	current density vector [A/m^2]
J_n	nth order Bessel function of first kind
J'_n	nth order Bessel function of second kind
k	wave number [1/m]
k_0	wave number of free space [1/m]
k_B	Boltzmann constant
k_c	cut-off wave number [1/m]
l	cylinder internal length [m]
n	number of changing periods in θ-direction
N_A	Avagadro constant
P	molar polarisability [C/m^2]
p	pressure [bar]
p_{avg}	average pressure within a single measurement [bar]
p_{diff}	pressure difference within a single measurement [bar]
p_i	internal pressure [bar]
p_{max}	maximum pressure within a single measurement [bar]
p_{min}	minimum pressure within a single measurement [bar]
p_o	external pressure [bar]
Q_l	loaded Q-factor
q	number of changing periods in z-direction
r	radial cylindrical coordinate [m]
r_o	cylinder outer radius [m]
T	temperature [°C]
t	time [s]
$\tan\delta$	loss tangent

u_1, u_2	orthogonal coordinates
v	wave speed [m/s]
v_{ni}	ith root of J'_n for TE$_{ni}$ modes
x_h	hydrogen gas mole fraction
x_m	methane gas mole fraction
z	axial cylindrical coordinate [m]
α_a	attenuation coefficient
α_c	distribution factor
α_P	molecular polarisability related to temperature [C/m^2]
α_t	thermal expansion coefficient
β	phase change coefficient
Γ	voltage reflection coefficient
γ	propagation constant [1/m]
γ_{ni}	propagation constant of a TM$_{ni}$ or TE$_{ni}$ mode [1/m]
Δf_r	offset between f_t and f_m [Hz]
$\Delta\varepsilon_r$	offset between ε_t and ε'_m [Hz]
δ	skin depth [m]
ε	complex permittivity [F/m]
ε_0	permittivity of vacuum [F/m]
ε'	real part of permittivity
ε''	imaginary part of permittivity
ε'_m	real part of measured relative permittivity
ε'_r	real part of relative permittivity
ε''_r	imaginary part of relative permittivity
ε_r	complex relative permittivity
ε_s	static permittivity [F/m]
ε_t	theoretical relative permittivity [F/m]
ε_∞	infinite relative permittivity [F/m]
η_0	intrinsic impedance of vacuum [V/A]
θ	tangential cylindrical coordinate [rad]
λ	wavelength [m]

λ_c	cut-off wavelength [m]
λ_r	resonance wavelength [m]
μ	complex permeability [H/m]
μ_0	permeability of vacuum [H/m]
μ'	real part of permeability
μ''	imaginary part of permeability
μ_e	molecule electric dipole moment [C·m]
μ_{ni}	ith root of J_n' for TM$_{ni}$ modes
μ_r	relative complex permeability
ρ_c	charge density [C/m^3]
ρ_m	molar density [m^3/mol]
σ	conductivity [S/m]
σ_l	longitudinal stress [Pa]
σ_r	radial stress [Pa]
σ_t	tangential stress [Pa]
σ_{yp}	yield stress [Pa]
τ	relaxation time [s]
ω	angular frequency [rad/s]
ω_d	angular relaxation frequency [rad/s]

Chapter 1

Introduction

1.1 Background and Motivation

Hydrogen as an energy carrier has significant potential to contribute to clean and renewable energy solutions. For this reason, the European Union (EU) has set a target to produce 10 billion tonnes and import 10 billion tonnes of hydrogen by 2030 (European Commission 2020). As the hydrogen market escalates, the necessity for precise measurement technologies becomes increasingly critical. This master research contributes to the measurement technologies needed to ensure product quality in the hydrogen production and distribution processes.

This master work develops and tests a measurement system utilising a cylindrical cavity resonator used for detecting the dielectric constant of gases. The dielectric constant, or the relative permittivity of a gas varies on a few factors, namely gas composition, density, temperature, and pressure. The core hypothesis suggests that variation in the dielectric constant can serve as an effective indicator for detecting gas mixture components.

As opposed to other measurement systems for measuring dielectric properties, resonator methods are frequently used because of their high accuracy and sensitivity (Chen et al. 2004). A closed system with a small volume was chosen to be able to contain a gas under pressure, while also making it insensitive to most environmental conditions. This type of resonator measurement system has been tested on a limited range of gases with successful measurements of the dielectric constant, such as in studies performed by Ewing and Royal (2002a), Kano (2021), and Vanzura, Geyer, and Janezic (1993). No studies have however thus far been performed investigating hydrogen and its impurities with this type of measurement system.

There are many ways to produce hydrogen, with the most common ways being grey, blue, and green hydrogen production. Grey hydrogen is produced primarily through steam-methane reforming, a process where methane reacts with high-temperature steam to produce hydrogen, carbon monoxide, and small amounts of carbon dioxide (Timmerberg, Kaltschmitt, and Finkbeiner 2020). It currently accounts for about 96% of global hydrogen production (Petrakopoulou and García-Tenorio 2023). Blue hydrogen is, in similarity to grey, produced from natural gas but involves capturing and storing the emitted carbon dioxide, thus reducing its environmental impact (Timmerberg, Kaltschmitt, and Finkbeiner 2020). Green hydrogen is produced via water electrolysis, and is the most environmentally sustainable method. It is projected to contribute to 42% of hydrogen production by 2030 and 60% by 2035 (European Commission 2020). Despite the growth in green and blue hydrogen technologies, this thesis will focus on the impurities associated with grey hydrogen production, due to its current predominance in the market.

Steam-methane reforming is commonly performed in combination with pressure swing adsorption (PSA) to remove unwanted contaminants. Bacquart et al. (2018) performed a study discussing the most common contaminants after hydrogen production processes, including steam methane reforming with PSA, and found that although the contaminants potentially present in the hydrogen depend on the process technology and on the purification step, the most common impurity is carbon monoxide, occurring frequently as a contaminant.

Impurities in hydrogen may originate from the production processes, or occur throughout the hydrogen supply chain. Therefore, the purity of the hydrogen needs to be monitored and controlled at several steps along the hydrogen processes in order to reach certain standards. The international standard ISO 14687:2019 specifies the minimum quality characteristics of hydrogen fuel for distribution for stationary and vehicle applications (International Organization for Standardization 2019). It gives the minimum mole fraction of hydrogen, as well as the maximum concentration of individual impurity components. Beyond the stringent requirements of measuring hydrogen quality and impurities set by the ISO standards, the method proposed in this thesis also holds potential for a broader application in various industrial and scientific fields, delivering significant utility in enhancing safety measures, optimising production processes, and verifying gas compositions in critical environments.

The master thesis contributes to the Norwegian Centre for Hydrogen Research (HyValue) lead by Norwegian Research Center (NORCE 2023), where the aim is to develop knowledge, methodology and innovative solutions for hydrogen-based energy carriers with zero emissions.

1.2 Objectives

The primary objective of the thesis is to develop a measurement system using a cylindrical cavity resonator to determine the dielectric constant of gases, with a focus on hydrogen. The specific objectives of the thesis work are outlined as follows:

- Review existing literature and apply theoretical knowledge to design and construct a functional cylindrical cavity resonator.
- Perform a theoretical sensitivity analysis to assess the impact of temperature and pressure variations on the dielectric constant of H_2 gas.
- Pressure test the system and conduct preliminary quantitative measurements of the system using various pressurised gases.
- Analyse the experimental results, and compare them to the theoretical values of an ideal measurement system.
- Assess the measurement system's effectiveness for hydrogen applications and propose potential improvements for future usage.

1.3 Thesis Outline

The master thesis consists of 7 chapters and 5 included appendices. In Chapter 1, the motivation and background, and the objective of the work is presented. Chapter 2 presents the theoretical foundation upon which the thesis is built. Chapter 3 presents the sensor literature review and design discussions. Chapter 4 presents permittivity calculations and a sensitivity analysis from temperature and pressure. Chapter 5 describes the experimental part, including the final design, pressure testing, gas measurements and data processing. Chapter 6 presents and discusses the results, and lastly Chapter 7 concludes the work and discusses future work. Appendix A includes a Safe Job Analysis, identifying the measurement hazards. Appendix B includes a the measurement procedure. Appendices C, D, and E, present the pressure measurement data, the reflection coefficient data and a narrow view of reflection coefficient data, respectively.

Chapter 2

Theory

This chapter gives an overview of the theoretical framework foundational to this thesis, focusing specifically on electromagnetic concepts related to the permittivity of gases. In Section 2.1, electromagnetic waves are introduced with a short explanation on Maxwell's equations. Section 2.2 provides a general introduction to dielectric theory, and subsequently narrowing down to the dielectric properties of gases along with certain theoretical approaches useful in explaining the complex factors affecting dielectric behaviour. In Section 2.3, electromagnetic wave propagation and transmission line theory is explained, which leads up to an brief overview of certain broadband structures in Section 2.4, before explaining the propagation along a cylindrical waveguide in Section 2.4.2. Section 2.5 briefly reviews different methods for measuring permittivity, setting the context for Section 2.5.1, which explains the cylindrical cavity resonance method. Finally, Section 2.6 describes the practical theory and considerations differing from an ideal measurement system.

2.1 Electromagnetic Waves

Electromagnetic waves are oscillations of electric and magnetic fields that propagate through space, with the fields oriented perpendicular to each other and to the direction of wave travel. They travel with a constant velocity in vacuum of (Chen et al. 2004):

$$c = \frac{1}{\sqrt{\mu_0 \varepsilon_0}} = 3 \cdot 10^8 \text{ m/s}, \tag{2.1}$$

where μ_0 is permeability in vacuum and ε_0 is permittivity in vacuum. In a medium, the electromagnetic waves travel with a velocity of (Chen et al. 2004):

$$v = \frac{1}{\sqrt{\mu\varepsilon}} = \frac{1}{\sqrt{\mu_0\mu_r\varepsilon_0\varepsilon_r}}, \tag{2.2}$$

where μ and ε are the permeability and permittivity of the material, and μ_r and ε_r are the permeability and permittivity of the material relative to vacuum.

Maxwell's equations provide a mathematical model for electromagnetic radiation. The equations describe how electric and magnetic fields are generated and changed by charges, currents and changing fields, uncovering the nature and symmetry of the wave-like behaviour of electromagnetic radiation. They are given as follows (Chen et al. 2004):

$$\nabla \cdot \mathbf{D} = \rho_c \tag{2.3}$$

$$\nabla \cdot \mathbf{B} = 0 \tag{2.4}$$

$$\nabla \times \mathbf{H} = \frac{\partial \mathbf{D}}{\partial t} + \mathbf{J} \tag{2.5}$$

$$\nabla \times \mathbf{E} = -\frac{\partial \mathbf{B}}{\partial t}, \tag{2.6}$$

and have the following relations:

$$\mathbf{D} = \varepsilon\mathbf{E} = (\varepsilon' - j\varepsilon'')\mathbf{E} \tag{2.7}$$

$$\mathbf{B} = \mu\mathbf{H} = (\mu' - j\mu'')\mathbf{H} \tag{2.8}$$

$$\mathbf{J} = \sigma\mathbf{E}, \tag{2.9}$$

where **D** is the electric displacement vector, ρ_c is the charge density, **B** is the magnetic flux density vector, **H** and **E** are the magnetic and electric field strength vectors respectively. $\varepsilon = \varepsilon' - j\varepsilon''$ is the complex permittivity of the material and $\mu = \mu' - j\mu''$ is the complex permeability of the material, explained further in Section 2.2. **J** is the current density vector and σ is the conductivity of the permeated material.

Electromagnetic waves are split into different categories for different ranges of wavelengths. From the lowest to the highest wavelengths, these are gamma rays, X-rays, visible light, infrared light, microwaves and radio waves. In this work, microwaves will be used, with wavelengths spanning from approximately one millimeter to 30 cm. These wavelengths correspond to frequencies ranging between 1 GHz and 300 GHz.

The relationship between frequency and wavelength is given by (Hertz 1893):

$$f = \frac{\omega}{2\pi} = \frac{v}{\lambda}, \tag{2.10}$$

where ω is the angular frequency, v is the wave speed and λ is the wavelength.

2.2 Dielectric Theory

Permittivity describes the interaction of a material with an electric field applied to it, and permeability describes the interaction of a material with a magnetic field applied to it, as stated in Chen et al. (2004). In this study, permittivity will have the most focus. The relative value for permittivity in relation to vacuum, ε_r, is often used:

$$\varepsilon_r = \frac{\varepsilon}{\varepsilon_0}, \tag{2.11}$$

where ε is the permittivity of the material, and ε_0 is permittivity in vacuum. The relative permittivity ε_r is a complex number consisting of a real and an imaginary part. The complex value is used when the material is characterised as an insulator with losses. ε_r is then given by (Chen et al. 2004):

$$\varepsilon_r = \varepsilon_r' - j\varepsilon_r'', \tag{2.12}$$

where the real part, ε_r', measures the amount of energy stored in the material from an external electric field, and the imaginary part, $j\varepsilon_r''$, represents the material's loss in response to an electric field, created by the motion of dipoles within the material, which is the ability of the material to absorb electromagnetic energy (Griffiths 2023). The loss tangent $\tan\delta$ is a measure of the ratio between the imaginary part and the real part of the permittivity (Griffiths 2023):

$$\tan\delta = \frac{\varepsilon_r'}{\varepsilon_r''} \tag{2.13}$$

The loss factor ε_r'' is limited by the material's relaxation time τ, which describes the time it takes for a material to respond to changes in an applied electric field. The relaxation time can be described by the equation (Chen et al. 2004):

$$\tau = \frac{1}{\omega_d} = \frac{1}{2\pi f_d}, \tag{2.14}$$

where ω_d is angular relaxation frequency and f_d is relaxation frequency, which are the frequencies where the dielectric loss is at its maximal value (Keysight Technologies 2019).

In a dielectric material, loss may also occur when electrons collide with other electrons and atoms, called finite conductivity. The complex relative permittivity can then be rewritten, including conductivity loss (Chen et al. 2004):

$$\varepsilon_r = \varepsilon_r' - j\left(\varepsilon_r'' + \frac{\sigma}{\omega\varepsilon_0}\right), \tag{2.15}$$

where ω is the angular frequency, and σ is the conductivity in the material.

2.2.1 Dielectric Mechanisms

The primary dielectric mechanisms that contributes to a material's permittivity include ionic polarisation, dipolar polarisation, atomic polarisation, and electronic polarisation. Ionic polarisation is caused by relative displacements between positive and negative ions in ionic crystals, which the electric field tends to direct causing dipolar polarisation. Atomic polarisation is caused by a displacement of atoms or atom groups in a molecule under the influence of an external electric field. Lastly, electronic polarisation is due to the displacement of nuclear and electrons in the atom under the influence of an external electric field (Keysight Technologies 2019).

The polarisation types are frequency-dependent. In lower frequency ranges, the permittivity is primarily influenced by slower mechanisms such as ionic conductivity and dipolar relaxation. Conversely, at higher frequencies, atomic and electronic polarisation become more significant. This relationship is depicted in Figure 2.1. As seen, each dielectric mechanisms contributing to dielectric behavior have a characteristic cut-off frequency. The loss factor ε_r'' will correspondingly peak at each critical frequency. In the microwave region, dipolar polarisation is the most prevalent.

Figure 2.1 depicts both polar and non-polar materials. The electron bond and molecular structure of gas molecules decides whether molecules are polar or non-polar. Polar molecules either have ionic bonding, involving two or more ions coming together and staying together by charge differences, or they have an asymmetric molecular structure. Non-polar molecules have covalent bonds, involving sharing of electrons between two or more atoms (Greenwood and Earnshaw 2012). For instance, H_2 has covalent molecules and the molecules are linear and symmetric, and thus H_2 is non-polar. Although this thesis focuses mostly around non-polar gases, some polar gases can still

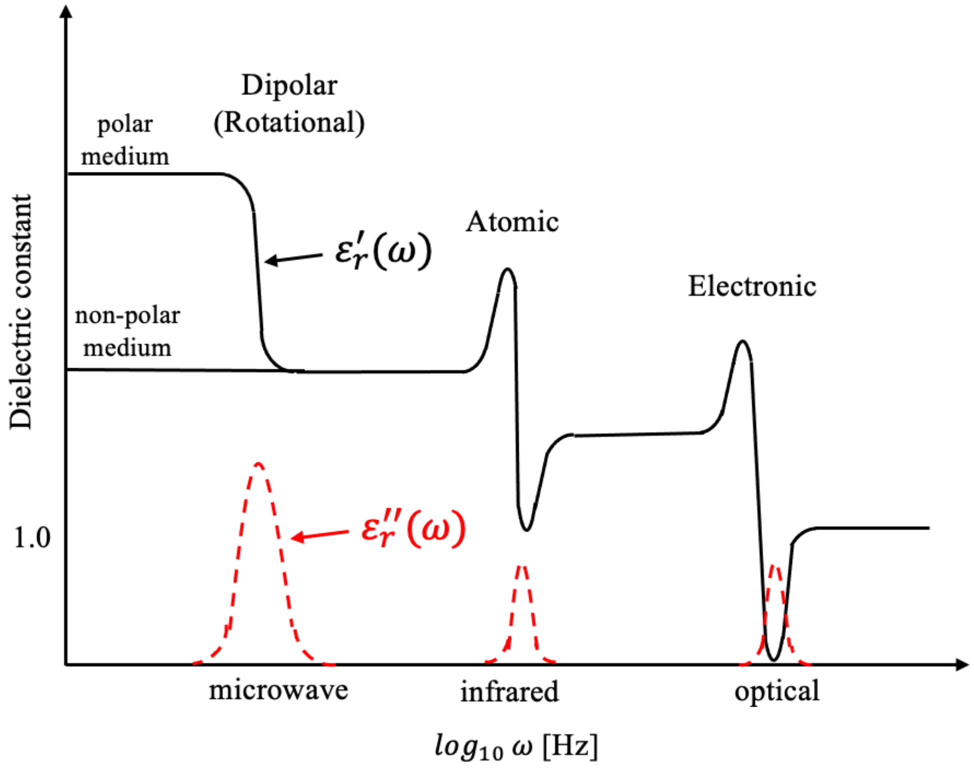

Figure 2.1: Frequency response of dielectric mechanisms for polar and non-polar mediums. Real part of relative permittivity ε_r' (black) and loss factor ε_r'' for a polar medium (red). Redrawn from Keysight Technologies (2019) and Royal (2000).

appear as impurities in H_2. Some polar gases include water vapor (H_2O), ammonia (NH_3), and carbon monoxide (CO) (NIST 2023).

2.2.2 Dielectric Theory of Gases

Dielectric theory of gases explain how gases respond to electric fields. Key factors affecting the permittivity of gases are explained below.

Firstly, all gases have a static permittivity ε_s. At low frequencies or under static conditions, gases exhibit a characteristic static permittivity value that reflects their dielectric behavior without significant molecular polarisation.

Secondly, while gases generally have a low and negligible loss factor ε_r'', they can experience small dielectric losses due to the dielectric mechanisms mentioned in Section 2.2.1. Polar gases have permanent dipole moments that can align in response to an electric field, increasing the gas's overall polarisability and thus its dielectric constant. Non-polar gases are composed of molecules without permanent dipole moments. Despite lacking inherent polarity, non-polar gases can still exhibit dielectric properties influenced by their molecular interactions and dynamics (Nyfors et al. 2000). However, in the microwave frequency range, non-polar gases show minimal dielectric losses (Royal 2000).

Thirdly, the permittivity of gases depends on the gases' density. Higher densities lead to stronger interactions between gas molecules, affecting their ability to respond to electric fields. Changes in temperature and pressure alter the density and distribution of gases, thus impacting the overall permittivity (Nyfors et al. 2000).

Finally, the gas composition will influence the dielectric properties. Even trace amounts of impurities or additional gases in a mixture can influence the dielectric properties (Nyfors et al. 2000). In the case of mixing a polar and a non-polar gas together, the molecules retain their individual properties. The non-polar gases typically contribute less to the overall dielectric constant of a gas mixture, while polar gases contribute more (Nyfors et al. 2000). Whether or not the mixture behaves as a polar or non-polar gas depends on the mixing ratio (Greenwood and Earnshaw 2012).

2.2.3 Debye Equation

The Debye equation is valuable for understanding how polar molecules in a material respond to an applied electric field. It describes the complex permittivity of a material due to dipolar and ionic relaxation, and is given by (Debye 1929):

$$\varepsilon_r = \varepsilon_\infty + \frac{\varepsilon_s - \varepsilon_\infty}{1 + j\omega\tau} - j\frac{\sigma}{\omega\varepsilon_0}, \tag{2.16}$$

where ε_∞ is the infinite dielectric constant, or the dielectric constant at high frequencies, and ε_s is the static, low frequency dielectric constant. ω is the angular frequency, and τ is the relaxation time.

2.2.4 Cole-Cole Equation

For complex materials, several different relaxation processes can take place simultaneously. This can be described as a sum of Debye processes with different relaxation times. Assuming the relaxation times are distributed equally about a common relaxation time τ, they can be represented by the introduction of an empirical factor, called the distribution factor α_c. This is represented by the Cole-Cole equation (Cole and Cole 1941):

$$\varepsilon_r = \varepsilon_\infty + \frac{\varepsilon_s - \varepsilon_\infty}{1 + (j\omega\tau)^{1-\alpha_c}} - j\frac{\sigma}{\omega\varepsilon_0}. \tag{2.17}$$

When α_c is zero, the Cole-Cole equation equals the Debye equation.

2.2.5 Clausius-Mosotti Equation and the Virial Expansion

Theoretical approaches to finding the dielectric constant ε_r commonly rely on the electric polarisation P rather than directly incorporating ε_r itself. Although there are no direct correlation between ε_r and P, some approximations have been made for both polar and non-polar fluids. Since the gases that are used in this work are non-polar, only this method will be explained.

For non-polar or weakly-polar fluids, the molar polarisability P as a function of molar density ρ_m, can be expressed with the Clausius-Mosotti relation (Tsankova et al. 2019; May, Moldover, and Schmidt 2009):

$$P = \frac{1}{\rho_m}\left(\frac{\varepsilon_r - 1}{\varepsilon_r + 2}\right). \tag{2.18}$$

The molar polarisability can be represented by the virial expansion (May, Moldover, and Schmidt 2009):

$$P = A_\varepsilon(1 + b_\varepsilon\rho_m + c_\varepsilon\rho_m^2). \tag{2.19}$$

In equation 2.19, A_ε represents the molar polarisability of the fluid at zero density, whereas b_ε and c_ε denote the second and third dielectric virial coefficients, respectively. These three macroscopic parameters are theoretically derivable through methods in quantum mechanics and statistical mechanics. The dominating coefficient is A_ε, which is a property of a single molecule given by (May, Moldover, and Schmidt 2009):

$$A_\varepsilon = \frac{N_A}{3\varepsilon_0}\left(\alpha_P(T) + \frac{\mu_e^2}{3k_BT}\right), \tag{2.20}$$

where N_A is the Avagadro constant, ε_0 is the permittivity of vacuum, $\alpha_P(T)$ is the molecule's polarisability related to the temperature, and k_B is the Boltzmann constant. μ_e is the molecule's electric dipole moment, which is zero for pure H_2, eliminating the last component of the equation. For many gases, the virial coefficients A_ε, b_ε and c_ε can be expanded into temperature dependent variables (Royal 2000; Harvey and

Lemmon 2005).

In the study of dielectric properties of gases, theoretical frameworks enhance the understanding of the intricate dielectric properties of gases (May, Moldover, and Schmidt 2009). Other equations of state, such as the Van der Waals-Berthelot equation, can also be helpful in determining the permittivity of non-polar gases specifically (Sobko 2017).

2.3 Electromagnetic Wave Propagation and Transmission Line Theory

Transmission-line theory is often used to understand the propagation and resonance of electromagnetic waves within a medium. Assuming a linear medium with no free charge or free current ($\mathbf{J} = 0$ and $\sigma = 0$), and considering sinusoidal variations over time in the electric field **E** and magnetic field **H**, Maxwell's equations (Eq. 2.3-2.6) can be used to analyse an electromagnetic wave along a transmission line. The wave equation for the electrical field **E** and magnetic field **H** is given by (Chen et al. 2004):

$$\nabla^2\mathbf{E} + k^2\mathbf{E} = 0 \tag{2.21}$$

$$\nabla^2\mathbf{H} + k^2\mathbf{H} = 0, \tag{2.22}$$

with the wave number k given as:

$$k = \omega\sqrt{\varepsilon\mu} = \frac{2\pi}{\lambda} \tag{2.23}$$

In transmission structures, the electromagnetic fields are decomposed into transverse and axial components:

$$\mathbf{E} = \mathbf{E}_T + \mathbf{E}_z \tag{2.24}$$

$$\mathbf{H} = \mathbf{H}_T + \mathbf{H}_z, \tag{2.25}$$

where T is the transverse component and z is the axial component.

There are three propagation modes existing for electromagnetic waves. The first is the transverse electric (TE) wave, where no electric waves exist in the axial direction,

$\mathbf{E}_z = 0$. If there are no magnetic waves in the axial direction, $\mathbf{H}_z = 0$, then the electromagnetic wave is called a transverse magnetic wave (TM) wave. The last type is when there are neither electric nor magnetic waves in the axial direction, $\mathbf{E}_z = 0$ and $\mathbf{H}_z = 0$, known as a transverse electromagnetic (TEM) wave (Chen et al. 2004).

2.4 Broadband Structures

Different types of structures are used to confine or lead electromagnetic waves along. TEM waves can only spread along broadband structures containing at least two conductors because a static electric field is needed (Chen et al. 2004). Common transmission structures of this sort are two parallel lines, coaxial line and stripline. While normally used to support TEM waves, these structures can also support TM and TE mode.

TM waves and TE waves can spread in hollow waveguides, normally made from highly conductive metal. Hollow metallic waveguides can be rectangular, circular and ridged. The circular waveguide is formed as a cylindrical pipe, as shown in Figure 2.2.

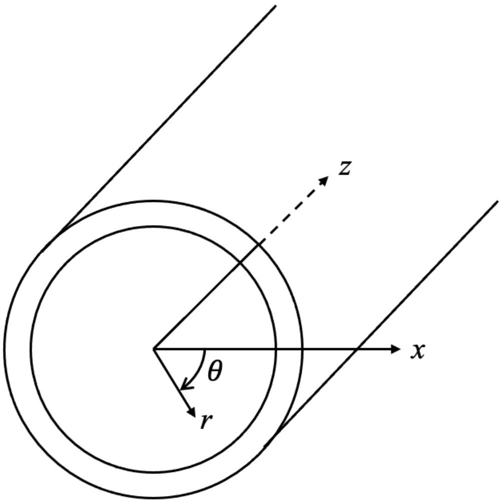

Figure 2.2: Cross-section of a circular waveguide with cylindrical coordinates: radial r, tangential θ, and axial z. Redrawn from Chen et al. (2004).

2.4.1 Hollow Metallic Waveguide

A hollow metallic waveguide is an enclosed system which prevents radiation loss. The wave propagation of a hollow metallic waveguide with infinite length can be described by (Chen et al. 2004):

$$\mathbf{E}(u_1, u_2, z, t) = C_1 \mathbf{E}(u_1, u_2) e^{j\omega t - \gamma z} \tag{2.26}$$

$$\mathbf{H}(u_1, u_2, z, t) = C_2 \mathbf{H}(u_1, u_2) e^{j\omega t - \gamma z} \tag{2.27}$$

$$\gamma^2 = -(k^2 - k_c^2), \tag{2.28}$$

where **E** and **H** are the electric and magnetic fields propagating in the waveguide along the z-axis, u_1 and u_2 are two orthogonal coordinates perpendicular to the z-axis with time t, and C_1 and C_2 are mode-dependent complex constants. The propagation parameter γ is related to wave frequency, medium properties, and field distributions. k_c is the cut-off wave number, explained below.

There is a critical point between transmission state and cut-off state in a hollow metallic waveguide where $\gamma = 0$. This frequency is called the cut-off frequency f_c, and the corresponding wavelength and wave number are called the cut-off wavelength λ_c and cut-off wave number k_c. The relationship between f_c and λ_c is given by (Chen et al. 2004):

$$k_c = \frac{2\pi}{\lambda_c}. \tag{2.29}$$

When the frequency in the system is high ($k > k_c$), then γ is an imaginary number (Chen et al. 2004):

$$\gamma = j\beta, \tag{2.30}$$

where β is the phase change coefficient, equaling

$$\beta = k\sqrt{1 - (k_c/k)^2}, \tag{2.31}$$

Then Equations 2.26 and 2.27 become (Chen et al. 2004):

$$\mathbf{E}(u_1, u_2, z, t) = C_1 \mathbf{E}(u_1, u_2) e^{j(\omega t - \beta z)} \tag{2.32}$$

$$\mathbf{H}(u_1, u_2, z, t) = C_2 \mathbf{H}(u_1, u_2) e^{j\omega t - \gamma z} \tag{2.33}$$

If the frequency is low ($k < k_c$), then γ becomes a real number:

$$\gamma = \alpha_a = k_c\sqrt{1-(k/k_c)^2}, \tag{2.34}$$

where α_a is the attenuation coefficient. Then Equations 2.26 and 2.27 become (Chen et al. 2004):

$$\mathbf{E}(u_1,u_2,z,t) = C_1\mathbf{E}(u_1,u_2)e^{\alpha_a z}e^{j\omega t} \tag{2.35}$$

$$\mathbf{H}(u_1,u_2,z,t) = C_2\mathbf{H}(u_1,u_2)e^{\alpha_a z}e^{j\omega t} \tag{2.36}$$

Equations 2.35 and 2.36 indicate that the phase of **E** and **H** does not change with the z-axis, which indicates that the wave is in a cut-off state. For this reason, the system works as a high-pass filter. The transmission requirement is then $k > k_c$ and $\lambda < \lambda_c$, and β can be rewritten (Chen et al. 2004):

$$\beta = \frac{2\pi}{\lambda}\sqrt{1-\left(\frac{\lambda}{\lambda_c}\right)^2}. \tag{2.37}$$

2.4.2 Circular Waveguide

A circular waveguide, as shown in Figure 2.2, can transmit TM and TE waves. In the wave analysis of a circular waveguide of radius a, cylindrical coordinates are used (r, θ, z), where r is the radial coordinate, θ is the tangential coordinate, and z is the axial coordinate. The propagation mode is denoted as TM$_{ni}$ or TE$_{ni}$, where n indicate the number of changing periods in θ-direction and i indicate the number of changing periods in r-direction. The field components of the TM$_{ni}$ and TE$_{ni}$ resonant modes in a circular waveguide are given as (Chen et al. 2004):

TM$_{ni}$ modes

$$\mathbf{E}_r = -A_p\gamma_{ni}\left(\frac{a}{\mu_{ni}}\right)J_n'\left(\frac{\mu_{ni}}{a}r\right)cos(n\theta) \tag{2.38}$$

$$\mathbf{E}_\theta = -A_p\frac{n}{r}\gamma_{ni}\left(\frac{a}{\mu_{ni}}\right)^2 J_n\left(\frac{\mu_{ni}}{a}r\right)sin(n\theta) \tag{2.39}$$

$$\mathbf{E}_z = A_p J_n\left(\frac{\mu_{ni}}{a}r\right)cos(n\theta) \tag{2.40}$$

$$\mathbf{H}_r = \frac{k_0}{j\gamma_{ni}\eta_0}E_\theta \tag{2.41}$$

$$\mathbf{H}_\theta = -\frac{k_0}{j\gamma_{ni}\eta_0}E_r \tag{2.42}$$

$$\mathbf{H}_z = 0, \tag{2.43}$$

where the constant A_p is related to the microwave power transmitted in the waveguide. The Bessel functions are solutions of Bessel's differential equation, where J_n is the nth order Bessel function and μ_{ni} is the ith root of J_n' (Chen et al. 2004). $\gamma_{ni} = \sqrt{k_c^2 - k_0^2}$ is the propagation constant calculated from the wave number at cut-off state k_c and the wave number of free space k_0. η_0 is the intrinsic impedance of free space.

TE$_{ni}$ modes

$$\mathbf{H}_r = -B_p\gamma_{ni}\left(\frac{a}{\nu_{ni}}\right)J_n'\left(\frac{\nu_{ni}}{a}r\right)cos(n\theta) \tag{2.44}$$

$$\mathbf{H}_\theta = -B_p n\gamma_{ni}\left(\frac{a}{\nu_{ni}}\right)^2 J_n\left(\frac{\nu_{ni}}{a}r\right)sin(n\theta) \tag{2.45}$$

$$\mathbf{H}_z = -B_p J_n\left(\frac{\nu_{ni}}{a}r\right)cos(n\theta) \tag{2.46}$$

$$\mathbf{E}_r = \frac{jk_0\eta_0}{\gamma_{ni}}H_\theta \tag{2.47}$$

$$\mathbf{E}_\theta = -\frac{jk_0\eta_0}{\gamma_{ni}}H_r \tag{2.48}$$

$$\mathbf{E}_z = 0, \tag{2.49}$$

where B_p is related to the microwave power transmitted, J_n is the nth order Bessel function and ν_{ni} is the ith root of J_n'.

Figure 2.3 shows the field distributions of certain basic TM$_{ni}$ and TE$_{ni}$ circular waveguide modes. Along the θ-direction, the field changes as a sinusoidal wave, and the period number ranges from 0 to 2π. In the radius direction, the field changes according to the Bessel function.

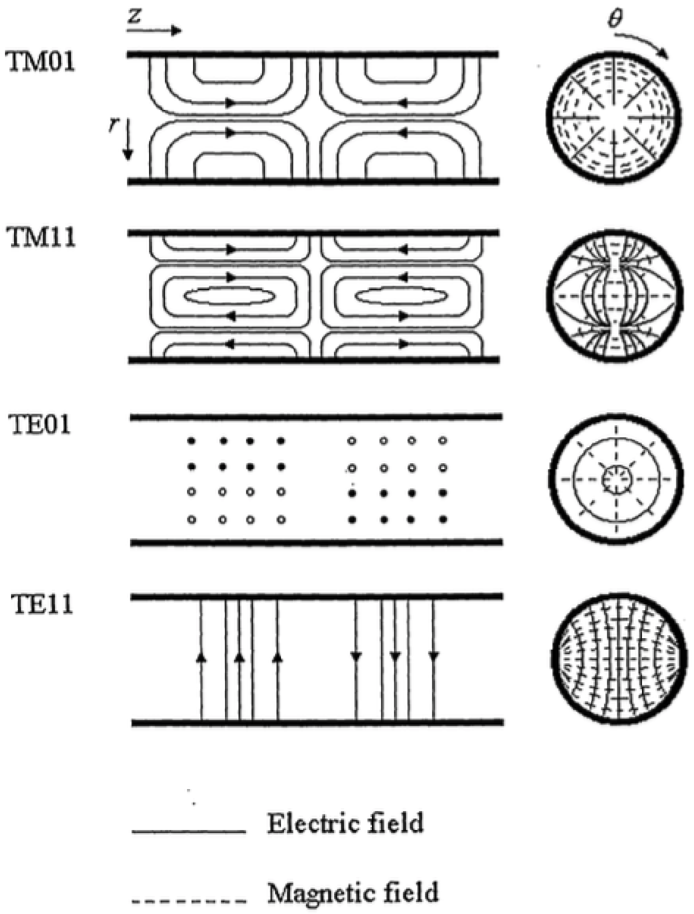

Figure 2.3: Cross-sections of TM$_{01}$, TM$_{11}$, TE$_{01}$ and TE$_{11}$ mode field patterns in a circular waveguide, with radial r, tangential θ and axial z coordinates (Waldron 1970).

The lowest order propagation mode is often called the fundamental or dominant mode. The fundamental mode have the lowest cut-off frequency and will give the lowest resonance frequency (Chen et al. 2004). In a circular waveguide, this is TE$_{11}$, which offers minimal degradation of signals (Petrescu 2018).

2.4.3 Degeneration Phenomena

The degeneration phenomenon is when two or more modes have the same resonant frequency, and typically occur for circular waveguides (Chen et al. 2004). There are two types, called polar degeneration and E-H degeneration. Polar degeneration refers to the phenomena where there are two kinds of field distributions that have the same shape, but their polarisation planes are perpendicular to each other. This goes for TM_{ni} and TE_{ni} modes where $n \neq 0$. E-H degeneration occurs because the roots for J_0' and J_1 are the same. This means that TM_{1i} and TE_{0i} have the same wavelength (Chen et al. 2004).

2.5 Microwave Property Measurement

Similarly to there being different broadband structures to lead electromagnetic waves, there are different structures used for material property characterisation. These are generally divided into resonant and non-resonant methods. Non-resonant methods are often used to get an overview of electromagnetic properties over a frequency range. In contrast, resonant methods are often used to get accurate knowledge of dielectric properties at a singular frequency or at several discrete frequencies (Chen et al. 2004). In this chapter, the cylindrical cavity resonance method is described.

2.5.1 Cylindrical Cavity Resonance Method

By closing the ends of a cylindrical waveguide, a cylindrical cavity resonator can be made. Figure 2.4 shows the design of a cylindrical cavity resonator with radius a and a finite length l. The resonant modes include TM_{niq} and TE_{niq}, corresponding to TM_{ni} and TE_{ni} modes of the circular waveguide. The subscripts n and i have the same significance as in a circular waveguide, while the subscript q denotes the number of changing cycles in z-direction.

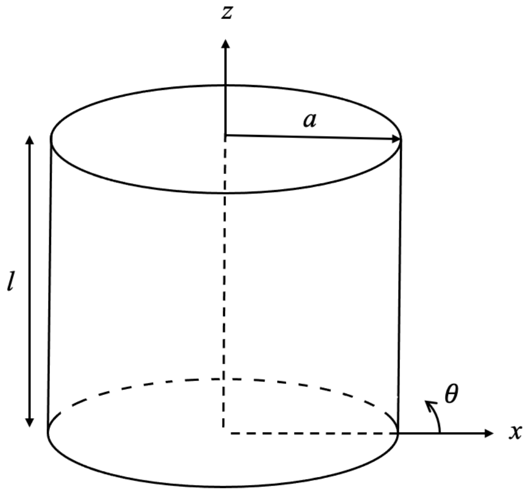

Figure 2.4: Design of a cylindrical cavity resonator with radius a and length l, and cylindrical coordinates in tangential θ, and axial z direction. Redrawn from Chen et al. (2004).

The field components of the TM$_{niq}$ and TE$_{niq}$ resonant modes in a cylindrical cavity are given below (Chen et al. 2004):

TM$_{niq}$ modes

$$E_r = -\frac{2B_p}{k_c} \cdot \frac{q\pi}{l} J_n'(k_c a) cos(n\theta) sin\left(\frac{q\pi}{l} z\right) \tag{2.50}$$

$$E_\theta = \frac{2B_p n}{k_c^2 a} \cdot \frac{q\pi}{l} J_n(k_c a) sin(n\theta) sin\left(\frac{q\pi}{l} z\right) \tag{2.51}$$

$$E_z = 2B_p J_n(k_c a) cos(n\theta) cos\left(\frac{q\pi}{l} z\right) \tag{2.52}$$

$$H_r = -j\frac{2B_p \omega \varepsilon n}{k_c^2 a} J_n(k_c a) sin(n\theta) cos\left(\frac{q\pi}{l} z\right) \tag{2.53}$$

$$H_\theta = -j\frac{2B_p \omega \mu}{k_c^2 a} J_n'(k_c a) cos(n\theta) cos\left(\frac{q\pi}{l} z\right) \tag{2.54}$$

$$H_z = 0, \tag{2.55}$$

with cut-off wave number k_c:

$$k_c = \frac{v_{ni}}{a}, \ (n = 0, 1, 2, ...; i = 1, 2, 3...). \tag{2.56}$$

n, i, and q are the corresponding cycles in θ-, r-, and z-direction respectively. The constant B_p is related to the microwave power transmitted, a is the radius, and l is the length. J_n is the nth order Bessel function and v_{ni} is the ith root of J_n'. The resonant wavelength in a cylindrical cavity in TM$_{niq}$ mode is (Chen et al. 2004):

$$\lambda_r = \frac{1}{\sqrt{\left(\frac{v_{ni}}{2\pi a}\right)^2 + \left(\frac{q}{2l}\right)^2}}. \tag{2.57}$$

Which gives the resonance frequency:

$$f_{niq} = \frac{c}{2\pi\sqrt{\mu_r \varepsilon_r}} \sqrt{\left(\frac{v_{ni}}{a}\right)^2 + \left(\frac{q\pi}{l}\right)^2}, \tag{2.58}$$

The quality factor or Q-value, is defined as the ratio of the energy stored in the cavity to the power losses within in the cavity. A higher Q-value suggests greater accuracy and a narrower bandwidth for the cavity resonator. For a TM$_{niq}$ mode, the waveform factor can be calculated from (Ishii 1995):

$$Q_0 \frac{\delta}{\lambda_r} = \frac{\sqrt{v_{ni}^2 + (\frac{q\pi a}{l})^2}}{2\pi(1 + \frac{2a}{l})}, \tag{2.59}$$

where δ is the skin depth of the conductor and λ_r is the resonance wavelength in the cavity.

TE$_{niq}$ modes

$$H_r = -j\frac{2A_p}{k_c} \cdot \frac{q\pi}{l} J_n'(k_c a) cos(n\theta) cos\left(\frac{q\pi}{l}z\right) \tag{2.60}$$

$$H_\theta = j\frac{2A_p}{k_c^2 a} \cdot \frac{q\pi}{l} J_n(k_c a) sin(n\theta) cos\left(\frac{q\pi}{l}z\right) \tag{2.61}$$

$$H_z = -j2A_p J_n(k_c a) cos(n\theta) sin\left(\frac{q\pi}{l}z\right) \tag{2.62}$$

$$E_r = \frac{2A_p \omega\mu n}{k_c^2 a} J_n(k_c a) sin(n\theta) sin\left(\frac{q\pi}{l}z\right) \tag{2.63}$$

$$E_\theta = \frac{2A_p \omega\mu n}{k_c^2 a} J_n'(k_c a) cos(n\theta) sin\left(\frac{q\pi}{l}z\right) \tag{2.64}$$

$$E_z = 0, \tag{2.65}$$

with the cut-off wave number k_c:

$$k_c = \frac{\mu_{ni}}{a}, \ \ (n = 0,1,2,...; i = 1,2,3...). \tag{2.66}$$

n, i, and q are the corresponding cycles in θ-, r-, and z-direction respectively. The constant A_p is related to the microwave power transmitted, a is the radius, and l is the length. J_n is the nth order Bessel function and μ_{ni} is the ith root of J'_n. The resonant wavelength of TE$_{niq}$ mode is given as (Chen et al. 2004):

$$\lambda_r = \frac{1}{\sqrt{\left(\frac{\mu_{ni}}{2\pi a}\right)^2 + \left(\frac{q}{2l}\right)^2}} \tag{2.67}$$

Which gives the resonance frequency:

$$f_{niq} = \frac{c}{2\pi\sqrt{\mu_r \varepsilon_r}} \sqrt{\left(\frac{\mu_{ni}}{a}\right)^2 + \left(\frac{q\pi}{l}\right)^2} \tag{2.68}$$

The Q-value for a TE$_{niq}$ mode is, similarly to TM$_{niq}$, found by using the waveform factor, calculated from (Ishii 1995):

$$Q_0 \frac{\delta}{\lambda_r} = \frac{\sqrt{\mu_{ni}^2 + (\frac{q\pi a}{l})^2}}{2\pi(1 + \frac{2a}{l})}. \tag{2.69}$$

Figure 2.5 shows the field distributions of some basic modes for cylindrical cavities as cross-sections lengthwise and crosswise.

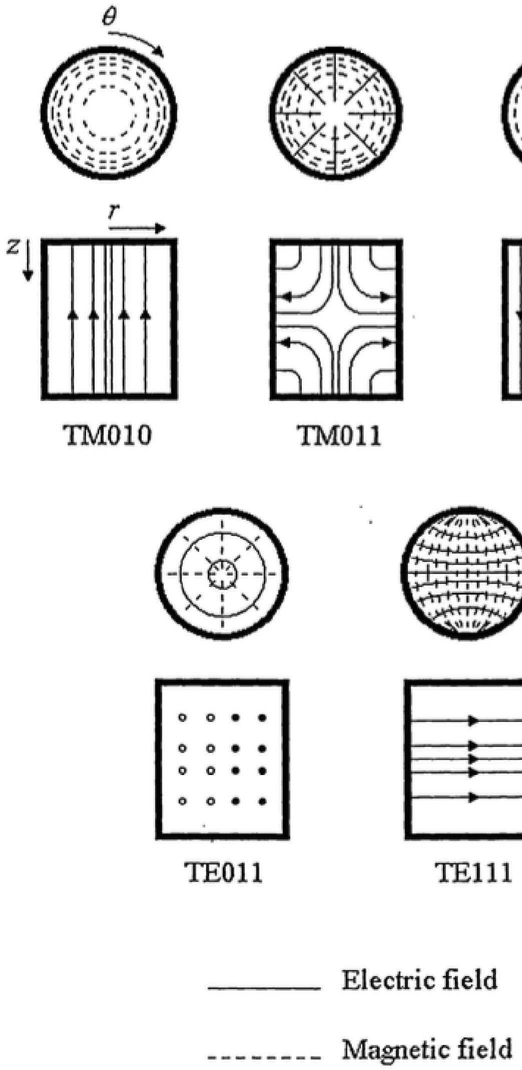

Figure 2.5: Cross-sections of TM_{010}, TM_{011}, TM_{110}, TE_{011} *and* TE_{111} *mode field patterns in a cylindrical cavity, with radial r, tangential* θ *and axial z coordinates (Waldron 1970).*

2.6 Measuring Resonance Frequency and Dielectric Constant

The resonance frequency can be measured in two different ways, by the reflection coefficient method or the transmission coefficient method. The reflection method requires a singular coupling, while the transmission method requires dual couplings. They have different advantages depending on the application (Nyfors et al. 2000). In this work, only a single coupling is used, and thus the focus is on the reflection coefficient method.

2.6.1 The Reflection Coefficient Method

The method of reflection coefficient implies that a wave is transmitted along a cable, into the resonator, and the reflected power is measured. The ratio of the reflected power to the incident power is the reflection coefficient Γ (Chen et al. 2004):

$$\Gamma = \frac{\text{reflected power}}{\text{incident power}}, \tag{2.70}$$

2.6.2 Measured Resonance Frequency and Q-factor

The reflection coefficient Γ is measured using a vector network analyser (VNA). The VNA emits a wave into the resonator which propagates along the transmission line and reflects back and forth at the ends. Resonance occurs when the incident field is in phase with the reflected waves. This alignment leads to constructive and destructive interference, resulting in the formation of a standing wave pattern. Such resonance is observed only at specific frequencies, known as the resonant frequencies f_r. At these resonance frequencies, the energy oscillates between the electric field and the magnetic field, both containing equal amounts of energy (Nyfors et al. 2000).

In practice, the reflection coefficient data can produce a reflection coefficient graph. The graph shows the reflection coefficient's amplitude and phase in relation to frequency. Figure 2.6 shown an example of the reflection coefficient as a function of frequency for a narrow frequency window.

The figure shows the minimum frequency which is the resonance frequency f_r and the half-power bandwidth is found at the -3 dB point. A broader resonance peak means that the loss is higher. The loaded Q-factor, determined by the resonance frequency f_r and the half-power bandwidth B_{hp}, determines the sharpness of the resonance (Nyfors et al. 2000):

$$Q_l = \frac{f_r}{B_{hp}} \tag{2.71}$$

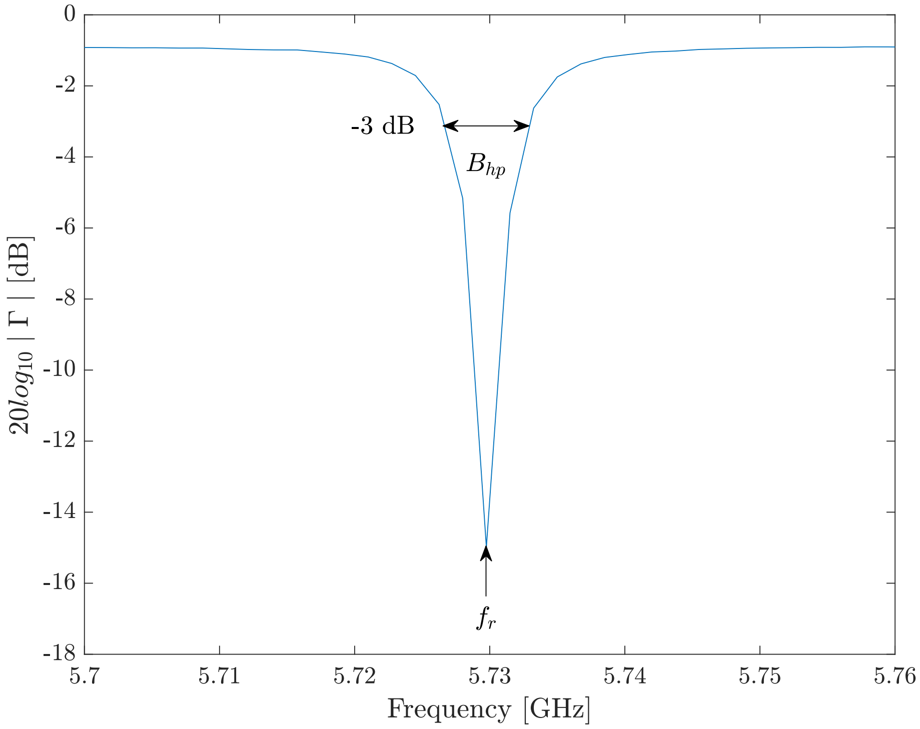

Figure 2.6: Reflection coefficient Γ *curve as a function of frequency, showing the resonance frequency* f_r *and the half-power bandwidth* B_{hp} *at -3 dB.*

2.6.3 Perturbation Mechanisms

Perturbation mechanisms are the disturbance mechanisms which differentiates the measured resonance frequency from the corresponding ideal cavity resonance frequencies and reduces the Q-factor. The ideal cavity resonators has perfect geometry, no mechanisms for energy loss, use ideal gases, and have fields exactly like calculated in Section 2.5.1. The disturbances in practical resonators are generally caused by loss from finite conductivity, imperfect geometry, coupling apertures, and non-ideal gases, explained below.

Firstly, practical resonators are made of materials which give rise to loss within the cavity walls. If the cavity has a high but finite electrical conductivity σ, such as for an aluminium alloy, then there will be a small tangential component of electric field penetrating the boundary surface, decaying exponentially within the wall (Royal 2000). The decay is characterised by the skin depth δ, defined as the depth at which the tangential electric field has fallen to $(1/\mathrm{e}) \cong 0.37$ of its initial value at the boundary surface (Chen et al. 2004). The skin depth perturbation causes the effective cavity length and diameter to be larger by approximately one skin depth at all cavity walls (Vanzura, Geyer, and Janezic 1993). The conductivity loss is mainly frequency-dependent, meaning that higher wavelengths penetrate the walls deeper and make the effective cavity dimensions bigger. The skin depth can be calculated from (Royal 2000):

$$\delta = \sqrt{\frac{1}{\pi f \mu_r \mu_0 \sigma}}, \tag{2.72}$$

where f is the operating frequency, σ is the conductivity of the metal, and μ_r and μ_0 is the relative permeability and the permeability of vacuum defined as $\mu_0 \approx 1.2566371 \times 10^6$ H/m (NIST 2023).

Secondly, the geometries of practical resonators are not perfect, often made in at least two parts joined together forming the cavity, which causes imperfect geometry. This leads to imperfect field mode patterns in comparison to the ideal field modes depicted in Figure 2.5. Lower-order modes are generally more affected by perturbations from imperfect geometry and volume changes because of their simple field mode patterns (Vanzura, Geyer, and Janezic 1993).

Thirdly, resonators also have coupling apertures from the gas and antenna couplings. When the coupling apertures are asymmetrical or not completely flush against the sides of the cylinder, they can again modify the distribution and intensities of the field mode patterns, thus affecting the resonance frequency and Q-factor. These perturbations are generally be frequency-dependent because the aperture dimensions relative to the wavelength inside determine their effect on the field distribution. Therefore, higher-order modes are generally more affected by perturbations from imperfect coupling apertures because of their complex mode patterns (Vanzura, Geyer, and Janezic 1993).

Lastly, all gases used in practice are not completely loss-free, which is assumed to be the case in an ideal resonator. Even if the dielectric properties of the gas are consistent, any inherent losses due to the gas itself, like absorption or dispersion, can lead to changes in the Q-factor of the resonator. The perturbations from non-ideal gases are pressure-dependent, with gases deviating more from ideal behavior under high pressure, leading to reduced resonance frequency. This is due to increased particle interactions and reduced volume per molecule, affecting the gas's bulk properties like permittivity and permeability, influencing the resonance frequency (Royal 2000). Considering N_2 and CO_2, CO_2 behaves more non-ideally at high pressures because of it being close to its critical point (NIST 2023).

These sources of non-ideality give rise to energy loss and will shift the resonance frequency from the ideal values (Royal 2000). The perturbation mechanisms can be explicit, such as the skin-depth perturbation, or implicit, like the perturbations due to the presence of coupling apertures inconsistencies in the internal dimensions (Royal 2000). The perturbations tend to amplify the losses, reducing the Q-factor. The perturbation mechanisms cause frequency shifts that are pressure and/or frequency-dependent, which in total create a pressure and frequency-dependent change in resonance frequency from an ideal cavity resonator (Royal 2000). In conclusion, most perturbation mechanisms can be difficult to quantify due to mathematical difficulties or the inability to fully characterise imperfections in the practical resonator. However, some effects can be accounted for, and others can be reduced through calibration.

2.6.4 Measured Dielectric Constant

The real part of the dielectric constant ε_r' can be determined by comparing measurements obtained from both gas-filled and an evacuated cavity. This is because the resonance frequencies within an idealised resonator are directly proportional to the phase velocity of light in the medium that fills the cavity (Ewing and Royal 2002a). For a non-magnetic gas, $\varepsilon_r = (c_0/c)^2$, where c_0 is the speed of light in vacuum defined as approximately 3×10^8 m/s and c is the speed of light in the gas. Given that $\varepsilon_r' >> \varepsilon_r''$, then ε_r' can be calculated from the resonance frequency of an evacuated resonator and that of a gas-filled resonator (Nyfors et al. 2000):

$$\varepsilon_r' = \left(\frac{f_{\text{vacuum}}}{f_{\text{sample gas}}} \right)^2, \tag{2.73}$$

where f_{vacuum} is the resonance frequency in an empty cavity and $f_{\text{sample gas}}$ is the resonance frequency in a gas-filled cavity. If no vacuum-filled cavity measurements are available, then ε_r' can be calculated with a reference gas instead, and the formula is rewritten:

$$\varepsilon_r'(p) = \left(\frac{f_{\text{reference gas}}(p)}{f_{\text{sample gas}}(p)} \right)^2 * \varepsilon_t(p), \tag{2.74}$$

where $f_{\text{reference gas}}(p)$ is the measured resonance frequency for the reference gas, $f_{\text{sample gas}}(p)$ is the measured resonance frequency for the sample gas, and $\varepsilon_t(p)$ is the theoretical relative permittivity of the reference gas found for the corresponding pressures, temperatures and gas compositions.

Chapter 3

Literature Review and Sensor Design

This chapter discusses and evaluates the sensor design using a literature study. As well as presenting certain studies from literature, the chapter discusses the following factors: Advantages and disadvantages of resonators, choice of cavity resonator, temperature and pressure control, material, internal dimensions, and wall thickness.

3.1 Literature Review on Cavity Resonators

3.1.1 Cavity Resonators - Advantages and Disadvantages

A metallic cavity resonator was chosen as opposed to other types of microwave sensors for its high sensitivity and accuracy. It also has the advantage of being a fully closed system, making it capable to contain a gas under pressure, also shielding it from external electromagnetic interference (Nyfors et al. 2000). In addition, cavity resonators are versatile and can be designed to operate over a wide range of frequencies.

Some disadvantages of cavity resonators are the complexity in design and fabrication. Symmetry is important in a cavity resonator because it helps minimize certain types of losses, such as radiation losses, resulting in higher quality factors (Chen et al. 2004). Metallic cavity resonators can also be quite sensitive to temperature variations because of their high conductivity, which can affect the resonator's frequency and Q-factor. Thus, careful temperature control and calibration may be necessary.

3.1.2 Choice of Cavity Resonator

Cavity resonators can be rectangular, cylindrical or spherical in shape, each having their advantages and disadvantages. Rectangular cavity resonators can be built from optically flat plates, which may make it difficult to obtain symmetry (Vanzura, Geyer, and Janezic 1993). A cylindrical cavity is easily built by connecting two lids to a hollow tube. This gives ease in fabrication, but will not give perfect symmetry. The sphere has the advantage of freedom from sharp edges but a high precision required to achieve a perfect sphere. Commonly, spherical resonators will have the most symmetry, rectangular resonators will have the least, and cylindrical will be in between (Nyfors et al. 2000).

Mode degeneracy is another factor to be considered, as it is less commonly found in rectangular resonators than in circular and cylindrical cavity resonators. This might cause signal reading problems for circular and cylindrical cavity resonators at some frequency ranges (Royal 2000).

The cylinder has ease in fabrication, and can be made with a relatively good symmetry. By making it out of a hollow tube with end-plates, the end-plates can also be interchangeable, which creates flexibility for future measurements. For these reasons, the cylindrical cavity resonator was chosen. The cavity designs evaluated in Section 3.1.3 are therefore all cylindrical in shape.

3.1.3 Cylindrical Cavity Resonators From Literature

In this chapter, some cylindrical cavity resonator designs from recent studies are compared. In addition to the hollow cylindrical cavity resonator type, there in another type called a re-entrant cylindrical structure which was also considered for this work. These types have a post which protrudes into the cavity from one of the end plates (Royal 2000). One of these types are also evaluated here, because of its inherent applicability to multi-phase fluids, making it well-suited for moisture fluid detection. They also provide higher quality factors and reduced sensitivity to geometric imperfections (Tsankova et al. 2016).

The cylindrical resonators compared here are a simple resonator from Ewing and Royal (2002a), a multi-purpose resonator from Kano (2021), and a re-entrant resonator from Tsankova et al. (2016). The simple type from Ewing and Royal (2002a) is shown in Figure 3.1 and the re-entrant type from Tsankova et al. (2016) is shown in Figure 3.2.

The resonator designed by Ewing and Royal (2002a) has a simple design. It has a small internal volume of just 5.7 cm^3 constructed by a brass cylinder with top and bottom plates, as shown in Figure 3.1. Similarly, Kano (2021) uses a simple cavity design with an internal volume of 90 cm^3. A bigger internal volume means that the frequency has to be lower in order to achieve the same mode patterns as a cavity with a

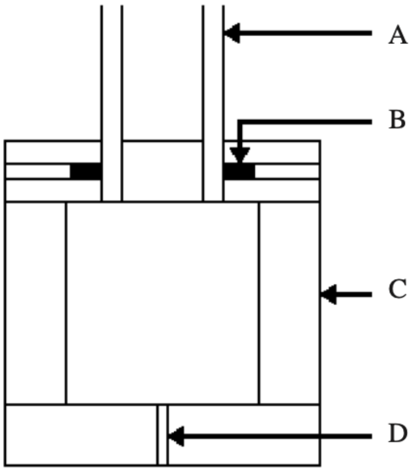

Figure 3.1: Schematic drawing of the Ewing and Royal (2002a) cylindrical resonator; A, coaxial cable; B, grub screw; C, the cylindrical resonator; D, the gas in-let opening.

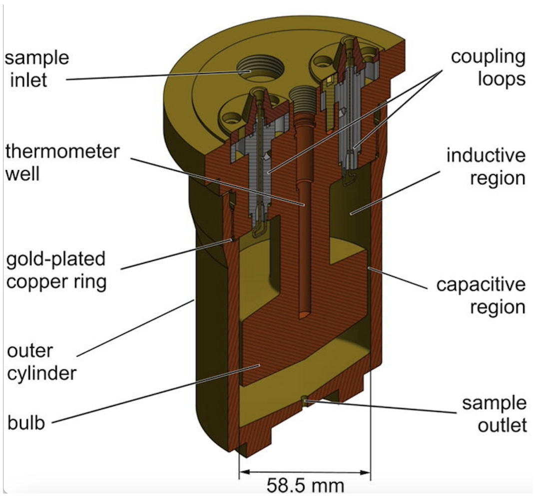

Figure 3.2: Cross-section illustration of the Tsankova et al. (2016) microwave re-entrant cavity.

smaller internal volume. In the design by Kano (2021), electromagnetic measurements for measuring permittivity are used in combination with acoustic measurements in the same measurement cell. While Ewing and Royal (2002b) measure on nitrogen gas at 40 bar, Kano (2021) measures on argon gas with a pressure of $1-5$ bar. The design by Ewing and Royal (2002a) resulted in a fractional uncertainty of relative permittivity at 0.95 probability level better than $\pm 5 \times 10^{-6}$, and the design by Kano (2021) resulted in a relative standard uncertainty of the relative permittivity of $\pm 4 \times 10^{-6}$.

Microwave re-entrant cavities have been developed significantly in the last few decades by Goodwin, Mehl, and Moldover (1996), May et al. (2001), May et al. (2004), Kandil, Marsh, and Goodwin (2005), Tsankova et al. (2017), and Sampson et al. (2019). The re-entrant measurement cavity from the study by Tsankova et al. (2016) was refurbished and used to measure multi-phase fluids. Over many years, the measurement system was tested on a range of different fluid mixtures, most relevantly on gas mixtures with carbon dioxide and small components of hydrogen (Tsankova et al. 2019). The CO_2 had mole fractions of approximately 0.95 and 0.75, and H_2 contributed to 0.05 and 0.25 respectively. The focus of the study was to find dew points, dielectric permittivity and densities for the fluid mixture. For both mixtures the the results showed that the relative combined expanded uncertainty ($k = 2$) for the dielectric permittivity was estimated to an accuracy of $\pm 0.34\%$ for pressures under 30 bar and $\pm 0.04\%$ for pressures between 30 and 82 bar. Furthermore, the experimental dew points for the 0.95 CO_2-mixture agree within 0.7%, while the ones for the 0.75 CO_2-mixture were within 2.5% of values predicted with the current reference data (Tsankova et al. 2019).

The resonators referred to in this chapter are further compared in table 3.1. The table firstly compares manufacturing parameters such as inner radius, length, volume, and construction material. Consequently, measurement parameters such as the material under test (MUT), operating pressure and temperature, measurement frequency window, and uncertainties are then compared. The Kano (2021) resonator measures on both argon gas and *trans*-1-chloro-3,3,3-trifluoropropene, however only the measurements on argon gas are listed for simplicity.

Table 3.1: Property comparison of cylindrical cavity resonators from Ewing and Royal (2002a) and Ewing and Royal (2002b), Kano (2021), and Tsankova et al. (2019).

	Ewing and Royal	**Kano**	**Tsankova et al.**
Inner radius	9.5 mm	24 mm	58.5 mm
Inner length	20 mm	50 mm	-
Internal volume	5.7 cm^3	90 cm^3	93 cm^3
Thickness	6 mm	-	5 mm
Material	"Solvol" chrome polished brass	Oxygen-free copper	Beryllium-copper alloy plated with silver and gold
MUT	Nitrogen gas	Argon gas	Hydrogen-Carbon dioxide mixtures
Operating pressure	$1-40$ bar	$1-5$ bar	$1-82$ bar
Operating temperature	300 K	$288-308$ K	$250-297$ K
Uncertainty	$u(\varepsilon_r) = \pm 5 \times 10^{-6}$[1]	$u(\varepsilon_r) = \pm 4 \times 10^{-6}$[2]	0.35 %[3], 0.4 %[4]
Frequency window	12−14 GHz sweep	6−17 kHz sweep	≈394 MHz

[1] Fractional maximal uncertainty of relative permittivity at 0.95 probability level.
[2] Relative standard uncertainty.
[3] Relative combined uncertainty for pressures below 30 bar.
[4] Relative combined uncertainty for pressures above 30 bar.

3.1.4 Temperature and Pressure Control

As mentioned, the pressure and temperature in the measurement system will need to be accurately monitored. This is mainly because of the sensitivity of the dielectric constant from temperature and pressure, which is analysed in Section 4.3. However, changes in internal pressure may also cause dimensional changes such as expansion and bulging, and temperature changes might cause expansion in the metal. For these reasons, the cavity resonators evaluated in Section 3.1.3 each have different forms of temperature and pressure control, discussed below.

The simple cylindrical design from Ewing and Royal (2002b) used a thermostat bath with a thermometer inside to control and maintain the measurement system's temperature. Within the thermostat bath, the resonator was placed in a pressure vessel, used to pressure-compensate the cylinder. A platinum resistance thermometer was also placed in the pressure vessel base. The combined acoustic and microwave resonator from Kano (2021) also utilised a pressure chamber and pressure sensor for pressure control. For temperature control, they used an internal thermostat and an outer water jacket. Similarly, the re-entrant cavity resonator from Tsankova et al. (2016) also used a pressure vessel outside of the cavity itself. The re-entrant resonator did not use a thermostat bath, but monitored the temperature with a thermometer from within the bulbous coaxial extension in a thermometer well, as shown in Figure 3.2.

In conclusion, all the reviewed microwave cavity studies use pressure chambers in order to compensate for the pressure internally and externally. While both a thermostat bath and a pressure vessel were considered in this work, simplicity was also a key factor considered. Since the measurements were planned to do in a lab with a stable room temperature, a thermostat bath was not prioritised. A fitting pressure chamber was not available, and would therefore likely have to be constructed especially for this work. For these reasons, neither a thermostat bath nor a pressure vessel was used for the experiments in this work. The cavity cell was however designed to endure high pressures by material choice, discussed in Section 3.2, and by wall thickness, discussed in Section 3.4. The temperature was monitored simply by a room thermostat, and the pressure was monitored with a pressure sensor attached to the gas inlet, as explained in the experimental setup in Section 5.2.

3.2 Choice of Material

In terms of choosing a material for use in a high-pressure resonator, some factors were considered, namely electrical conductivity, risk of hydrogen embrittlement, thermal expansion, strength, and availability. These factors are discussed below.

Firstly, using a metal with a higher electrical conductivity will lower the surface resistance, which will give measurements with a low rate of resistive energy losses. This will enhance the quality factor of the resonator, which gives a narrower bandwidth, leading to more distinct resonance peaks (Nyfors et al. 2000). Metals with high conductivity generally also have good thermal conductivity, which helps in dissipating potential heat in the measurements. High conductivity metals will also have a smaller penetration depth, allowing for less perturbation into the walls at high frequencies, further discussed in Section 2.6.3.

Secondly, hydrogen embrittlement is a phenomenon which might impact some metals in contact with hydrogen. When hydrogen embrittlement occurs, the hydrogen gas atoms enter the structure of a metal, making the it more brittle and prone to breaking (Lee and Woods 2016). With an increase in pressure, the susceptibility of hydrogen embrittlement generally increases. Hydrogen embrittlement has been noted to occur across a broad spectrum of temperatures, but its most pronounced effects are typically observed near room temperature for many materials (Vehoff 2007). Hydrogen embrittlement occurs in steels, as well as iron, nickel, titanium, cobalt and their alloys (Lee and Woods 2016). Embrittlement in steel or stainless steel can be avoided by choosing the proper alloy according to the temperature and pressure expected, following the Nelson curves (Nelson 1983). Metals such as copper, aluminium and stainless steel has lower susceptibility to hydrogen embrittlement according to Lee and Woods (2016). Another option in the choice of material is to use hydrogen barrier coatings which separate the metal from the gas, usually gold or silver, which also increase the electrical conductivity (Wetegrove et al. 2023).

Thirdly, a material with a small thermal expansion coefficient should be used. Thermal expansion is the ability of a material to change size with a change in temperature (Chen et al. 2004). The dimensions impact the resonance frequency, and thus it is important that they are not changing with small changes in temperature, especially if the temperature is not controlled such as with a thermostat bath. The thermal expansion is quantified by the thermal expansion coefficient. Aluminium alloys have a thermal expansion coefficient of $22-24$ ppm/°C, meaning that it expands between 22 and 24 parts per million of its original length. Different grades of stainless steel have a thermal expansion coefficient between $10-17$ ppm/°C (Callister et al. 2007).

In conclusion, a strong material with high conductivity, low suseptibility of hydrogen embrittlement, and a low thermal expansion will be a good choice for this application. In evaluation of the materials that were available, the most suitable option was aluminium alloy 6082, a light-weight metal with high electrical conductivity, high fracture toughness and good ductility. While the ductility is positive because it can make the material less prone to rupture or breaking, it might also have a downside of the ability to undergo significant plastic deformation causing changes to the internal dimensions. However, the strength was prioritised to increase the system's applicability in enduring high internal pressure. As for the hydrogen embrittlement effect, it is not significant for aluminium alloys for dry hydrogen gas near room temperature and up to pressures of 690 bar, according to Lee and Woods (2016).

3.3 Internal Dimensions

Depending on the location of the probe antenna on the cavity resonator, the tangential magnetic field or the normal electric field will penetrate the cavity and couple with the resonance mode. When the antenna is situated on one of the cylinder's end-plates, TM modes tend to dominate. This is caused by the more effective interaction between the magnetic field components, which are perpendicular to the direction of propagation, and the electric field component that circulates around the cylinder's axis. Conversely, positioning the antenna on the cylinder's sidewall typically enhances the prevalence of TE modes, due to more effective interactions with electric field components that are perpendicular to the direction of propagation (Nyfors et al. 2000).

Evaluating Equation 2.58 for TM_{niq} modes, it is shown the resonance frequencies occurring for a dielectric material within a cylindrical cavity resonator depends on the dimensions of the cavity a and l, the mode, and the dielectric properties of the material under test. As the dielectric properties of different gases do not differ in great extents, different internal dimensions can be adjusted to see the expected resonance frequencies, and a mode distribution can be chosen. Theoretical values for the permeability $\mu_r = 1$ and permittivity $\varepsilon_r = 1.0002$ for hydrogen at $T = 20°\text{C}$ and atmospheric pressure was used. Using a between 1 cm and 5 cm, some of the lowest resonance frequency modes were plotted for $l = 10$ cm in Figure 3.3. All the modes plotted here might not appear in a practical scenario, because of the geometrical imperfections in an actual cavity resonator.

The figure shows that the resonance frequency of all modes are higher for lower values of the radius. Modes where $q = 0$ have no changing cycles in z-direction, and are therefore theoretically independent upon the length l of the cylinder. The only degenerate modes for all lengths are TM_{012} and TM_{022}, which are two yellow curves overlapping in Figure 3.3. A steeper f_r curve, such as for TM_{110} and TM_{111}, indicates that f_r is more sensitive to dimensional changes. Based on Figure 3.3, choosing a radius was based on wanting an even separation between each mode. For this reason, $a = 2$ cm was chosen as the radius. In practice, some of these modes will not occur because of imperfect geometry in the cavity resonator.

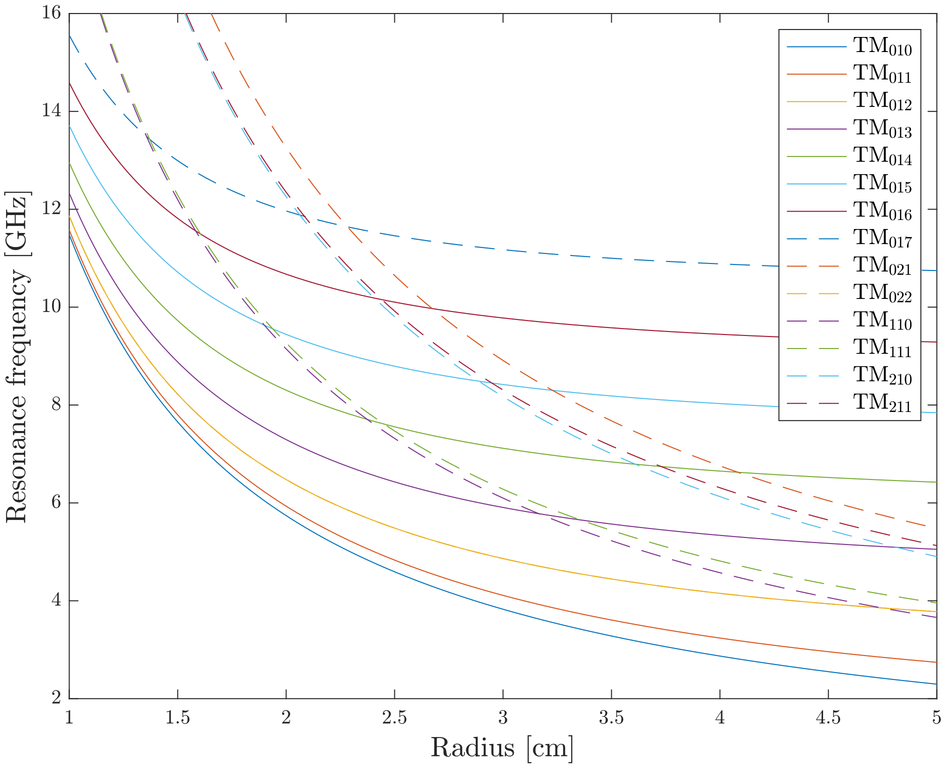

Figure 3.3: Resonance frequency in a hydrogen-filled cavity with length $l = 10$ *cm for different TM modes.*

3.4 Wall Thickness

The thickness of the cylinder walls has to accommodate for an internally high pressure, without enduring cracking or deformations. The cavity wall thickness calculations were based on the formula of some failure theories for thick-walled pressure vessels. A thick-walled pressure vessels means that that the wall thickness d is bigger than 1/10 of the internal radius a, meaning that the stress can not be assumed to be evenly distributed (Masikh, Tariq, and Sinha 2014).

The stress occurs in three directions: longitudinal stress σ_l, radial stress σ_r, and tangential stress σ_t (Khurmi and Gupta 2005). The longitudinal stress acts along length of the pipe, the radial stress acts to push the pipe outward from the center when internal pressure is bigger than external pressure, and the tangential stress stress acts around the circumference of the circle. The stresses for thick-walled cylinders can be calculated using Lamé's equations (Khurmi and Gupta 2005):

$$\sigma_l = p_i \frac{a^2}{r^2 - a^2} \tag{3.1}$$

$$\sigma_r = \frac{p_i a^2 - p_o r_o^2}{r_o^2 - a^2} + \frac{a^2 r_o^2 (p_0 - p_i)}{r^2 (r_o^2 - a^2)} \tag{3.2}$$

$$\sigma_t = \frac{p_i a^2 - p_o r_o^2}{r_o^2 - a^2} - \frac{a^2 r_o^2 (p_o - p_i)}{r^2 (r_o^2 - a^2)} \tag{3.3}$$

Where p_i is internal pressure, p_o is external pressure, a is the inner radius, r_o is the outer radius, and r is the radius to a point in the cylinder wall ($a < r < r_o$). Hoop stress is the largest principal stress, and therefore failure by fracture in cylindrical vessels is dominated by the hoop stress, according to Moss (2004). The external pressure p_o will equal atmospheric pressure, but is often approximated as 0 Pa (Khurmi and Gupta 2005). Eq. 3.3 can then be simplified:

$$\sigma_t = \frac{p_i a^2}{r_o^2 - a^2} - \frac{p_i a^2 r_o^2}{r^2 (r_o^2 - a^2)} \tag{3.4}$$

By setting $r = a$, and σ_t to the allowable yield stress σ_{yp} of the metal, the equation equals the maximum principal stress theory. This theory simply asserts that yielding occurs when the largest principal stress equals the yield strength, and is often used as the basis of designs (Moss 2004).The equation can then be solved for r_o to find the outer radius (Khurmi and Gupta 2005):

$$r_o = a\sqrt{\frac{1 + p_i/\sigma_{yp}}{1 - p_i/\sigma_{yp}}} \tag{3.5}$$

The allowable yield stress of an aluminium alloy 6082-T6 cylinder is typically 240 MPa (Astrup 2023). The inner radius a is set as 0.02 m. Solving for a maximal inner pressure p_i of 100 bar or 10 MPa, the outer radius becomes $r_o \approx 0.0209$ m and the thickness d comes out to 0.9 mm. This means that the cylinder thickness has to be a minimum of 0.9 mm in order to withstand an internal pressure of 100 bar.

While the maximum principal stress theory can provide a simplified analysis, it will not ensure total durability or resilience to failure. Failure can also happen due to defects in material or poor fabrication and quality control (Moss 2004). In addition to failure by fraction, the ratio of internal radius to its thickness will affect how much the cylinder expands with a high internal pressure. Pressure exerted on the internal surface without pressure compensation from the outside will dilate the internal dimensions, depending on the mechanical properties of the material from which the resonator is constructed, the temperature of operation, and the internal and external pressures (Royal 2000).

Thus by choosing a bigger thickness, the cylinder will be less prone to expansion under high pressures (Moss 2004). Another practical aspect, was that in order to secure the end-plates onto the cylinder, they would be screwed into the cylinder walls, and thus there was a need to accommodate for the screws. For these reasons, a thickness of $d = 10$ mm was chosen.

Chapter 4

Theoretical Dielectric Constant Calculations and Sensitivity

The permittivity of different gas compositions were found using the Thermodynamic Reference & Engineering Data (TREND) software package (Span et al. 2020). TREND utilises a range of different equations of state depending on their accuracy and the range of validity. The temperatures, pressures, and gas compositions are entered into the program, and the relative permittivity ε_r, as well as a range of dielectric properties, are given in return. All theoretical permittivity values used throughout this work are sourced from TREND.

4.1 Permittivity of Various Gases

In Figure 4.1, the relative permittivity values of the pure non- and weakly-polar gases hydrogen, argon, nitrogen, carbon dioxide, and methane are plotted against pressures between 1 and 100 bar at a temperature of 20°C.

The figure shows that the dielectric constant of gases rises with increasing pressure. Notably, hydrogen exhibits the least sensitivity to pressure changes, while carbon dioxide is the most affected. For instance, at 100 bar, the dielectric constant of hydrogen is approximately 1.024. This value is equivalent to the dielectric constants of nitrogen at 43 bar and carbon dioxide at 22 bar, as shown with the dotted line. Carbon dioxide reaches a critical point at 57 bar because it reaches a supercritical state, changing from a gas phase to a liquid phase at this point, but settling again at $\varepsilon_r \approx 1.47$ (Wei et al. 2020).

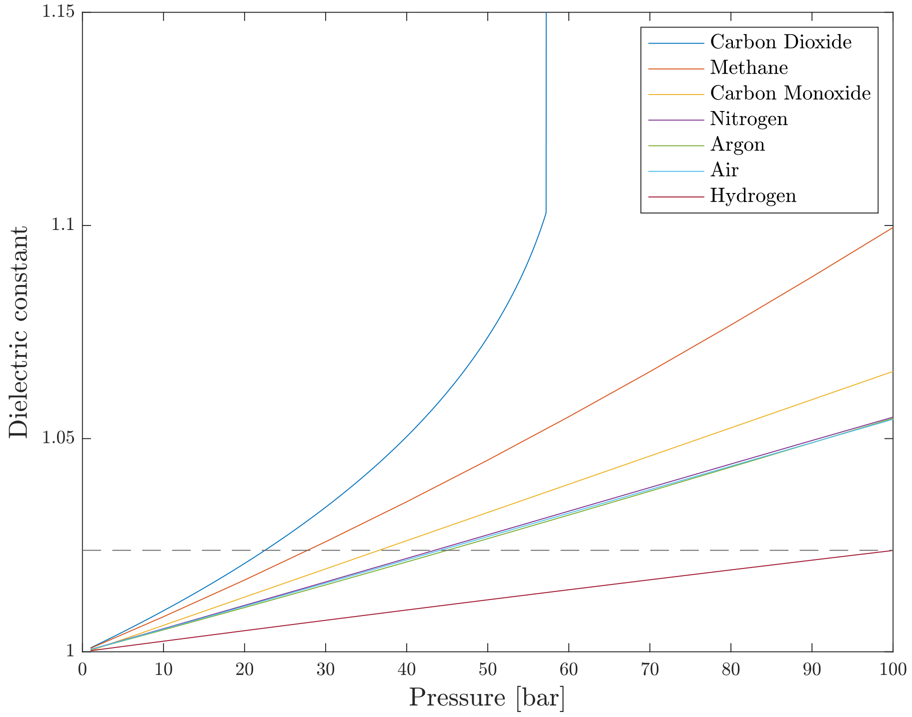

Figure 4.1: Pressure effect on gas dielectric constant for various gases at room temperature (20°C).

4.2 Permittivity of Hydrogen-Methane Mixtures

In order to look at the dielectric effect of small impurities in hydrogen gas (H_2), small mole fractions of of methane gas (CH_4) were added as an impurity in the H_2. The mole fraction is the ratio of molecules of a component to the total number of molecules in a gas mixture (Harvey and Lemmon 2005). The effects of temperature and pressure changes are investigated simultaneously.

The calculations were carried out with H_2 mole fraction x_h between 0.95 and 1.00, and corresponding CH_4 mole fractions x_m between 0.05 and 0.00. Figure 4.2 shows the pressure effect on dielectric constant for H_2/CH_4 gas mixtures at 20°C. The pressure p ranged from 1 to 100 bar. As shown, the methane contributes to a higher dielectric constant in the gas mixture. At higher pressures, the distinction between the gas mixtures becomes more significant. A change from 0 to 0.01 parts CH_4 in H_2 at 20°C contributes to a change in dielectric constant of $+10^{-5}$ at 1 bar, $+2.7\times10^{-4}$ at 50 bar and $+5.5\times10^{-4}$ at 100 bar.

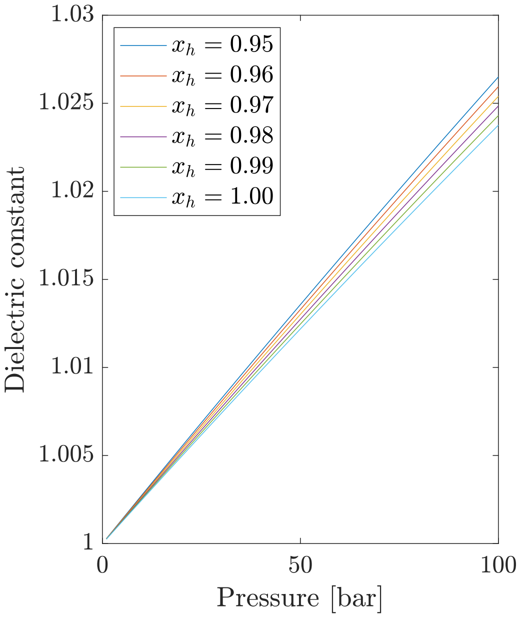

Figure 4.2: Pressure effect on dielectric constant for hydrogen-methane with hydrogen mole fractions of $0.95 < x_h < 1.00$ *at 20 °C.*

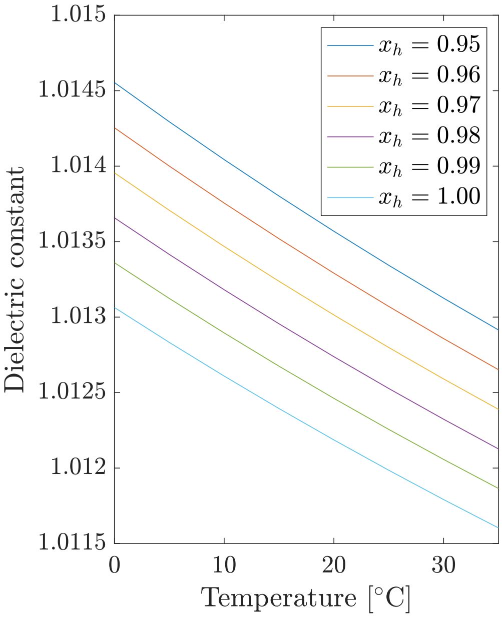

Figure 4.3: Temperature effect on dielectric constant for hydrogen-methane mixture with hydrogen mole fractions of $0.95 < x_h < 1.00$ *at 50 bar.*

The temperature effect, as shown in Figure 4.3, contributes to almost linear shifts in the dielectric constant with an increased impurity ratio. A temperature change of ±1 °C will change the dielectric constant by $\pm 4.6 \times 10^{-5}$ for any impurity ratio. As shown, the dielectric constant of hydrogen decreases with an increase in temperature.

In conclusion, the temperature and pressure affect the dielectric constant of a gas mixture significantly, an thus they have to be monitored in experiments in order to accurately determine the purity of the gas in question. In order to estimate the uncertainty that the temperature and pressure inflict on the dielectric constant, a sensitivity analysis is performed in Section 4.3.

4.3 Sensitivity From Temperature and Pressure Changes

An analysis is performed on pure H_2 in order to quantify the impact of changes in temperature and pressure on the dielectric constant ε_r. The method solely considers the theoretical impact from temperature and pressure on the dielectric constant in an ideal measurement system, and does not evaluate the total sensitivity in a realistic measurement system, which might include factors such as measurement drift, calibration errors, etc. The uncertainty $u(\varepsilon_r)$ is found from the standard uncertainties of measured temperature and pressure, and the respective sensitivity coefficients of the dielectric constant for temperature and pressure, as described in Section 4.2. The method supposes independent input quantities. The following equation is used (Bentley 2005):

$$u(\varepsilon_r)^2 = \left[\frac{\partial \varepsilon_r}{\partial T} u(T)\right]^2 + \left[\frac{\partial \varepsilon_r}{\partial p} u(p)\right]^2 \tag{4.1}$$

The standard uncertainties of the temperature and the pressure are assumed to be $u(T) = 0.1°\text{C}$ and $u(p) = 0.01$ bar, given the equipment that is available to use experimentally (Paroscientific, Inc. 2005). Table 4.1 shows values of $u(\varepsilon_r)$ calculated for temperatures between 0 and 30 °C and pressures between 1 and 100 bar. $\frac{\partial \varepsilon_r}{\partial T}$ and $\frac{\partial \varepsilon_r}{\partial p}$ are found numerically for small changes in T and p.

Table 4.1: Uncertainty in dielectric constant $u(\varepsilon_r)$ in units $\times 10^{-6}$ from changes in temperature T and pressure p for pure H_2.

p\T	**0 °C**	**10 °C**	**20 °C**	**30 °C**
1 bar	3.3	2.5	2.4	2.4
25 bar	4.0	3.3	3.2	3.0
50 bar	5.6	5.0	4.7	4.4
75 bar	7.5	6.8	6.3	6.0
100 bar	9.4	8.6	8.0	7.5

As shown, increasing pressure and decreasing temperatures will increase the sensitivity, and hence the uncertainty $u(\varepsilon_r)$. The uncertainty is below 10^{-5} for all temperatures above 0 °C and pressures below 100 bar. For instance, at 20 °C, the uncertainty will be $\pm 2.4 \times 10^{-6}$ at 1 bar, $\pm 4.7 \times 10^{-6}$ at 50 bar, and $\pm 8.0 \times 10^{-6}$ at 100 bar. In Section 4.2, it was found that a change in purity from pure H_2 to a 0.99/0.01 H_2/CH_4 mixture will contribute to a change in dielectric constant of $+10^{-5}$ at 1 bar, $+2.7 \times 10^{-4}$ at 50 bar, and $+5.5 \times 10^{-4}$ at 100 bar for 20 °C. By comparing these two results, a hypothetical scenario of an added impurity of 0.01 parts CH_4 into pure H_2 is considered. The ratio of uncertainty $u(\varepsilon_r)$ to a change dielectric constant with the added impurity is 3.8 for 1 bar, 57.9 for 50 bar, and 68.6 for 100 bar. This shows that the change in dielectric constant, because of a 0.01 CH_4 impurity added to H_2, is significantly larger than the uncertainty contribution for the dielectric constant because of temperature and pressure measurements.

It can be concluded that uncertainties in dielectric constant from temperature and pressure are low in comparison to an added impurity for high pressures. While an increased pressure is beneficial in the measurement system, it should be decided with safety precautions.

Chapter 5

Experimental

5.1 Final Design

5.1.1 Probe Antenna

The custom-built coaxial probe antenna is, simply put, composed of a coaxial transmission line with an electrically open end, as shown in Figure 5.1. The pressure rating for the probe antenna performed by NORCE has resulted in a maximum pressure of over 1000 bar (K. Folgerø from NORCE, personal communication, May 23, 2024). It is made of stainless steel with a plastic material between the inner and outer conductor. The inner conductor has a radius of 1.5 mm and the outer conductor has a radius of 5 mm (Folgerø et al. 2019; Haukalid and Folgerø 2016).

Figure 5.1: Picture of the coaxial probe antenna used for the experiments.

5.1.2 Cylindrical Cavity Resonator

The final design of the cylindrical cavity resonator is pictured in Figure 5.2. The resonator cell itself, along with a stand, was produced with help from the workshop at the Department of Physics and Technology at University of Bergen.

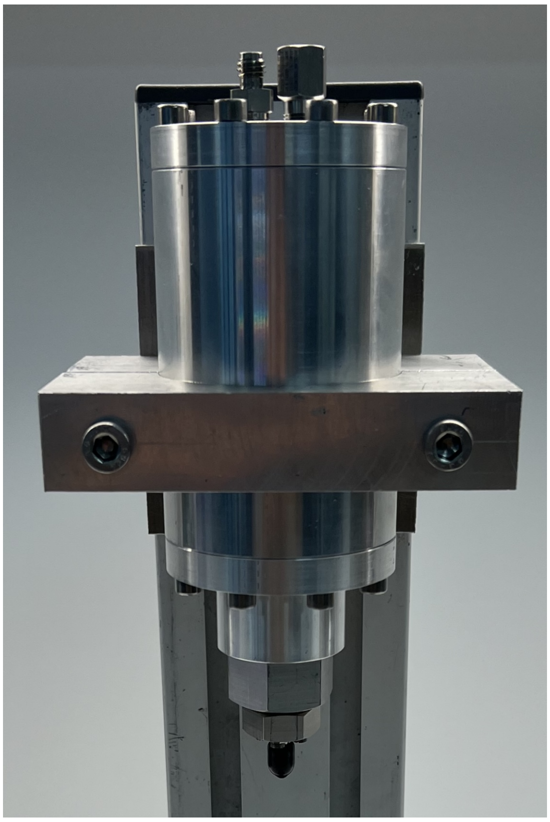

Figure 5.2: Picture of the measurement cell on a stand. The probe antenna is placed on the lower lid and the gas inlet and outlet are on the top lid.

The resonator cell was made from a hollowed out tube of aluminium alloy 6082 T6 cylinder. The internal dimensions have a radius of $a = 2$ cm and length of $l = 10$ cm, which makes an internal volume of 125.66 cm^3. The thickness is $d = 1$ cm for both the cylinder wall and the end-plates. The inner surface was buffed out in order to have a smooth surface.

One end-plate was made to fit the probe antenna. The threaded hole was placed in the middle of the lid with a diameter of 12.7 mm. The end of the probe antenna was made to fit flush on the inside lid, with no protrusion into the cavity. Below the antenna head, the screw thread had a length of 26 mm. Since the lid was only 10 mm, a nut with length 16 mm was made to fit between the head and the lid. On the side of the nut facing the lid, and on the antenna head facing the nut, there were tracks to fit two O-rings, sealing the construction.

Another end-plate was also made in order to fit two smaller antennas from Kemlon Products (1999). This construction could be used in a transmission method where one port transmits signal and the other port receives the signal, as explained in Section 2.6. Using this method might give more information about the resonance properties of the gas, but there is also an uncertainty regarding the inability to make these types of connectors flush against the end-plate, which might cause more asymmetry within the cavity. For this reason, this measurement system was not prioritised during this work.

The gas inlet and outlet were placed on one end-plate next to each other. They had screw holes which narrowed down to smaller holes on the inside, as instructed by the pipe adapter data sheets (Autoclave Engineers 2013; Swagelok 2024). The tubes connected to the pipe adapters were 1/8” steel piping.

There were tracks on either side of the cylinder to fit 21.95×1.78 mm Viton O-rings in order to seal the lids onto the tube, making it withstand high pressures. The end-plates were screwed on to the cylinder with 8 stainless steel screws on each side. The screws had a 5 mm diameter and were 16 mm long in order to provide structural compression. They were also coated with a silver paste, providing lubricity and resistance to corrosion.

5.1.3 Component Data

Table 5.1 shows the components used in the cylindrical cavity resonator system. The components used in the experimental setup are also included. The table includes the component name, the type and manufacturer, as well as the the maximum working pressures of each component.

According to Table 5.1, all components of the measurement cell have been evaluated for maximum working pressure, except for the measurement cell itself whose capacity is not formally tested. The O-rings that connect the end-plates to the hollow cylinder are assumed to be the weakest components, with a maximum tensile strength of 125 bar (Dichtomatik 2010). The O-rings connecting the antenna to the end-plate, however, are not subjected to direct internal pressure and are therefore unlikely to be the weak points. The overall maximum pressure that the measurement cell can withstand will depend on specific cases and conditions. Detailed results from pressure testing are documented in Section 5.2.2.

Table 5.1: Measurement system component name, manufacturer and type, and maximum working pressure. Citations and abbreviations in table footnotes.

Component	**Manufacturer and type**	**Maximum working pressure [bar]**
Measurement cell	IFT[1] workshop	> 50
O-ring (lid)[2]	21.95 x1.78 mm Viton	125
Screws[3]	A4-80 Stainless steel M5x16 mm	≈ 5600
Open-ended probe antenna[4]	NORCE workshop	>1000
O-ring (probe antenna)	-	-
Piping[5]	SS-316 1/8" OD,[6] 0.85 mm thickness	885
Pipe adapter	Autoclave Engineers NPT 15M22N1	1034
Pipe adapter	Swagelock 316 WAO	1378
Needle valve	Autoclave Engineers 10V2071	758
Needle valve	Autoclave Engineers 10V2081	1034
Tee fitting	Autoclave Engineers ST2220	758
Water pump[7]	Quizix QX	345
Back pressure regulator[8]	Equilibar Mity Mite S91XW	413
Pressure sensor[9]	Paroscientific Digiquartz Intelligent Transmitter 1001K-01	690

[1] Institute for Physics and Technology
[2] (Dichtomatik 2010)
[3] (ASTM International 2007)
[4] (K. Folgerø from NORCE, personal communication, May 23, 2024)
[5] (AIR-WAY Global Manufacturing 2024)
[6] Outer diameter
[7] (AMETEK, Inc. 2023)
[8] (Equilibar 2021)
[9] (Paroscientific, Inc. 2005)

5.2 Experiments

5.2.1 Initial Test

Initial tests with the measurement system were performed in order to evaluate the outcome of the reflection coefficient, analyse which modes appeared, and decide the vector network analyser (VNA) settings. The tests were performed with air at room temperature and atmospheric pressure. The gas connectors were connected, but no tubes were attached, as shown in Figure 5.2.

The coaxial cable was connected to the Rohde & Schwarz ZVL network analyser. The other side of the coaxial cable was then calibrated with the Rohde & Schwarz ZV-Z135 calibration kit, calibrating with an open/short/load method. The coaxial cable was held in a position close to the position it would be in if it were connected to the probe antenna throughout the calibration. After calibrating, the coaxial cable was connected to the probe antenna, and the reflection coefficient was measured. The VNA had a frequency range of 9 kHz−13.6 GHz. No resonance modes will peak below 4 GHz, as shown in Figure 3.3, and therefore the range was measured between 4 GHz and 13.6 GHz, as shown in Figure 5.3.

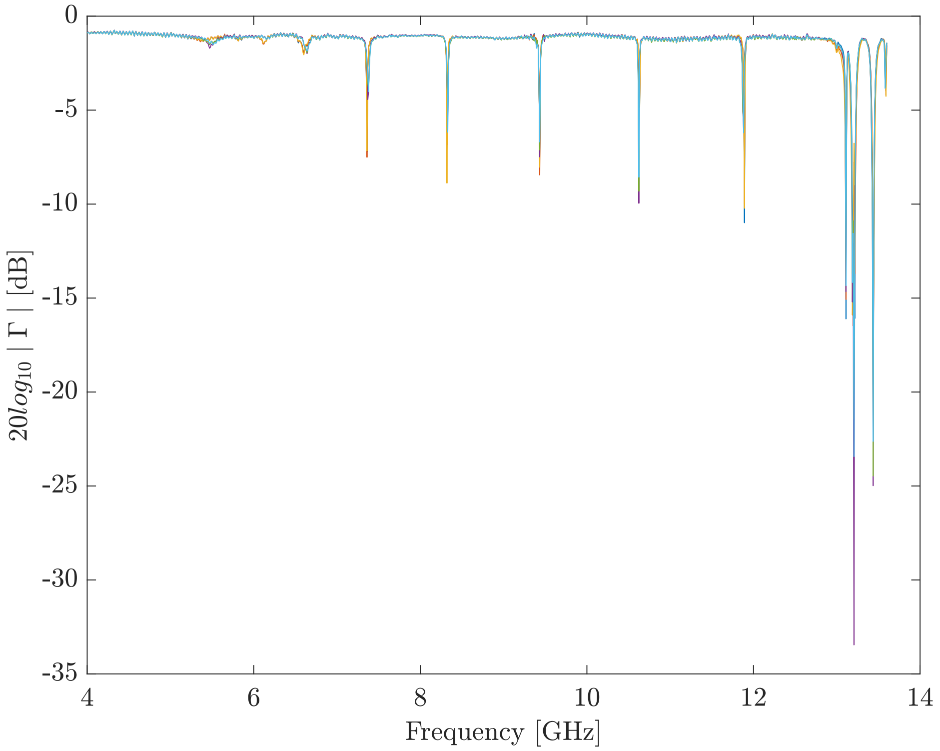

Figure 5.3: Logarithmic reflection coefficient Γ *against frequency for initial air measurements, probe antenna placed on the top lid.*

As shown, there were no resonance frequencies in the range below 5 GHz. In the range over 13 GHz, the resonance frequencies appeared very close together. In between, there were distinguishable resonance peaks, and for that reason, the initial frequency range in the gas experiments was chosen to be between 5 GHz and 12 GHz. The initial measurements were also performed in order to see whether placing the probe antenna lid on the top or bottom of the resonator would have an effect on the results. There was no distinguishable change in results between the two different methods.

The maximum measurement points in the VNA was 4001, so in order to get the most accurate data, this was chosen. The intermediate frequency (IF) bandwidth is the width of the filter used in the receiver part of the VNA to isolate and measure the response at each frequency, and a low IF bandwidth will give higher accuracy (Chen et al. 2004). A low IF bandwidth is favourable, but it increases the measurement time, and thus the pressure control during the measurement could be inaccurate. By choosing a bandwidth of 100 Hz, one measurement would take 88 seconds, which would give enough data but not take too long.

5.2.2 Hydrostatic Pressure Test

A hydrostatic pressure test was carried out in order to determine whether the system could withstand an internal pressure without leakages. The pressure test was performed using water because of its advantage of being nearly incompressible in comparison to gas. This means that less water is needed in order to increase the pressure considerably. In case of failure, it will also only release a small amount of energy, inflicting less of a safety hazard. The standard of hydrostatic pressure testing of gas cylinders is to pressure test with a minimum 150 % of the maximum working pressure (National Archives 2024).

The working pressure was decided by looking at the dielectric constant of different gases at room temperature in Figure 4.1. As mentioned, the dielectric constant of H_2 at 100 bar corresponds to the dielectric constant of N_2 at 43 bar, and CO_2 at 22 bar. Thus, lower-pressure measurements of N_2 and CO_2 could be compared to higher-pressure measurements of H_2. In addition, safety and the maximum working pressures in Table 5.1 were considered, and thus 50 bar was decided to be a safe working pressure to begin with. This would mean pressure testing the system up to 75 bar.

A Safety Job Analysis (SJA) was made for safe execution of the experiment, and is attached in Appendix A. The experiment was carried out in a suitable laboratory at NORCE with supervision and help from laboratory supervisors both in preparation for and during the test. The measurement cell was placed on the stand within a sturdy cabinet. All valves were placed on the outside of the cabinet so that the cabinet could be closed at all times when the pressure was on, and the pressure could be controlled from the outside.

A schematic drawing of the hydrostatic pressure test procedure is shown in Figure 5.4, and a step-by-step procedure plan is attached in Appendix B. In Figure 5.4, it is shown that the Quizix water pump was connected to a valve outside the cabinet before entering the cell from the top input. The output from the cylinder was connected to a valve on the outside of the cabinet before leading to a cross port valve which in turn lead to a precision back-pressure regulator (BPR) and a bucket which received deposit water. The water pump measured the cumulative volume data or the amount of volume entering the system, which was logged on a PC.

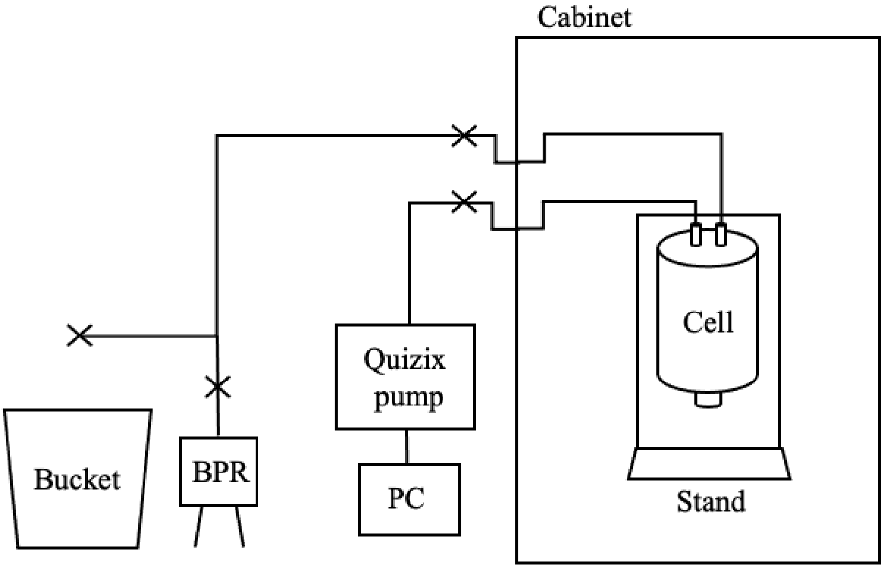

Figure 5.4: Schematic drawing of the measurement system for the hydrostatic pressure test.

To start the hydrostatic pressure test, the procedure went as follows. The bucket valve and BPR valve was closed, while the other valves remained open. The pump pressure was increased to approximately 5 bar and then the BPR valve was opened and flooded against. The back-pressure on the BPR, which was at approximately 10 bar, was then turned on. The pressure was then increased to above 10 bar, and the BPR valve was then closed. Then, the pressure could be increased incrementally. The pressure was increased before closing the input valve and then letting in stay for 10-15 minutes, logging possible drops in pressure.

The test was conducted in two rounds. In the first round, the pressure was dropping slightly for each pressure increment. In the end of the test, some minor leaks were found from the valve on the outside of the cabinet. The faulty valve and adjacent piping was then replaced. In round two, the pressured was measured at approximately 50 bar and 75 bar. The pressure was considerably more stable in the following round, as shown in Table 5.2.

Table 5.2: Hydrostatic pressure test results. Cum Vol: Cumulative volume obtained in the duration the pressure was held at.

Pressure [bar]	**Duration [min:sec]**	**Cum Vol [ml]**	**Operating Rate [ml/min]**
49.94±0.07	11:00	0.028	0.00255
74.93±0.07	11:00	0.031	0.00282

The cumulative volume data measures the amount of volume entering the system. If the cumulative volume was high when the system was closed, this would be an indication of leakage. As shown, the operating rate of water into the system was approximately 0.003 at both 50 bar and 75 bar, however slightly higher at 75 bar, which is to be expected given higher forces on the system. In conclusion, the measurement system system tolerated the hydrostatic test well at pressures up to 75 bar. There were only some minor leakages, but they were too small to locate. Both tests showed no visible leakage of water from the measurement cell itself.

5.2.3 Gas Measurements

Gas measurements were conducted in two rounds. In the first measurement series, measurements were conducted with N_2 and CO_2 gas. The gases had a purity of 99.999 % (Grade 5). In the second measurement series, measurements were conducted again with N_2 and CO_2, as well as a N_2/CO_2 gas mixture, containing 0.8 parts N_2 and 0.2 parts CO_2, and had a purity uncertainty of ±0.02. The experimental setup for the gas measurements is shown in figure 5.5.

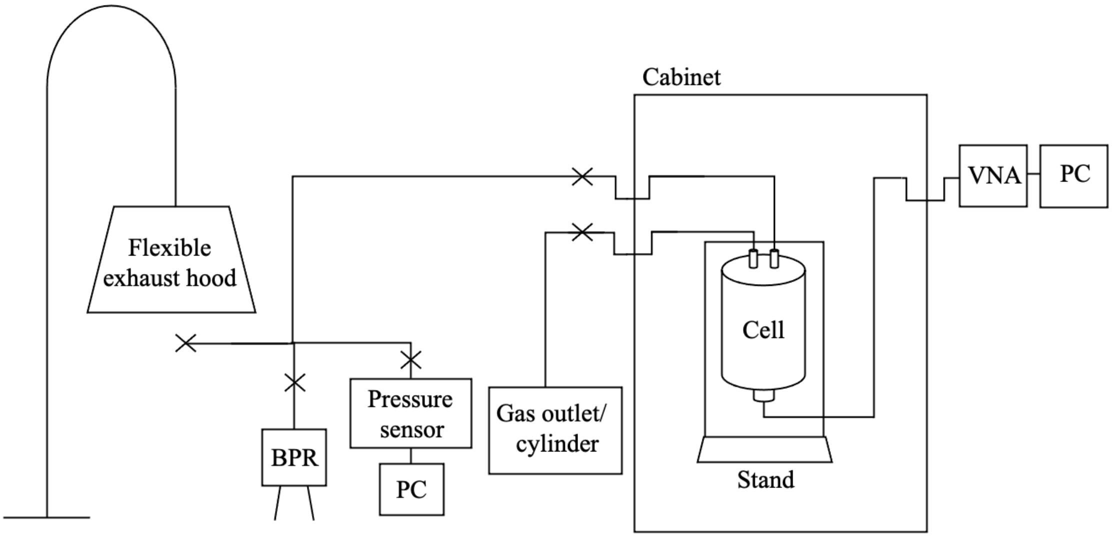

Figure 5.5: Schematic drawing of the pressurised gas test.

As shown, the changes from the system setup from the pressure test were the addition of a flexible exhaust hood placed over the gas outlet to remove fumes from the laboratory environment. A gas pressure sensor was added to the cross-port valve and controlled with a PC using the compatible software for the pressure sensor. The pressure sensor was set to perform and log one pressure measurement every second. The probe antenna was connected with a the coaxial cable to a vector network analyzer (VNA) for measurement. The VNA had a frequency range of 5-12 GHz, measuring

4001 points with a IF bandwidth of 100 Hz, measuring for 88 seconds per measurement. The VNA was calibrated with the Rohde & Schwarz ZV-Z135 calibration kit prior to each round of experiments. Before the calibration, the temperature of VNA, measurement cell, and cables was allowed to stabilize at the experimental temperature. The gas-supply was placed at the gas-inlet to replace the water pump. For the N_2 gas, the supply came from a wall outlet with a maximum pressure of 130 bar, the CO_2 came from a gas cylinder with a maximum pressure of approximately 40 bar, and the N_2/CO_2 mixture came from a 20 L gas cylinder with an initial bottle pressure of 200 bar. The VNA was set to measure continuously.

The procedure is described step-by-step in Appendix B, and the safety cautions in the SJA in Appendix A were followed. For both measurement rounds, the temperature was only monitored as a general room temperature, which was stable at 20.8 °C during the first experiment round, and at $21.1\ ^{\circ}C$ throughout the second experiment round.

For each gas, the system was flushed and depressurised 3 times before starting the measurements, which ensured that most of the previous gas was removed. The pressure data was logged and frequency sweeps were set to run continuously. For the first measurements of N_2 at 10 and 20 barg, the pressure was stabilised by continuously adjusting the pressure from the outlet. At 30 barg however, a new method was tested, and the gas inlet valve was closed, which proved to give a more stable pressure measurement. This method was therefore used for the rest of the experiments. In the first experiment round, measurements were done in 10 bar increments, going up and down. 2-4 measurements were carried out at each pressure point. The measurement setup was then deconstructed between the experiments, removing the probe antenna as well unscrewing the top and bottom lids of the measurement cell.

In the second experiment, the VNA settings were changed to a 5-9 GHz frequency range, keeping the 4001 measurement points and the 100 Hz bandwidth. The measurements were ran continuously, and the pressure measurements were taken every second. This time, the pressure started at maximum pressure, 50 bara for N_2 and the N_2/CO_2 mixture and 40 bara for CO_2, before decreasing the pressure in 5 bar increments. 3-4 measurements were taken at each pressure point.

A remark during both the experiments was that the pressure was holding better with CO_2 than with N_2 and the mixture. This might be caused by the molecular structure of CO_2 being larger than the that of N_2, leaking less through the small gaps in the system. This might cause a problem for measurements with H_2, being even smaller and lighter than N_2 molecules and having shorter bond lengths (NIST 2023).

5.3 Data Processing

5.3.1 Pressure Data Matching

The reflection coefficient measurement data were matched with the timing of the pressure data, adding the pressure data at the 88 second time slots of each measurements before calculating an average p_{avg} for each reflection measurement. The maximum and minimum pressure, p_{max} and p_{min}, for each time slot were also found, calculating a pressure difference $p_{\mathrm{diff}} = |p_{\mathrm{max}} - p_{\mathrm{min}}|$. The measurements with a pressure difference $p_{\mathrm{diff}} > 0.2$ were disregarded in further analysis. The average pressure p_{avg}, as well as the temperature T, was used to find the corresponding theoretical relative dielectric constant ε_t using the TREND software. For the N_2/CO_2 gas mixture, it was assumed to be in an exact 0.8/0.2 ratio when finding the ε_t.

The continuous pressure data, and the individual pressure measurements for the measurement time slots are plotted for N_2 February 6th in Figure 5.6. Here, the half-time point pressure average p_{avg}, pressure maximum p_{max}, and pressure minimum p_{min} point are shown. Similar figures for each gas measurement are shown in Appendix C.

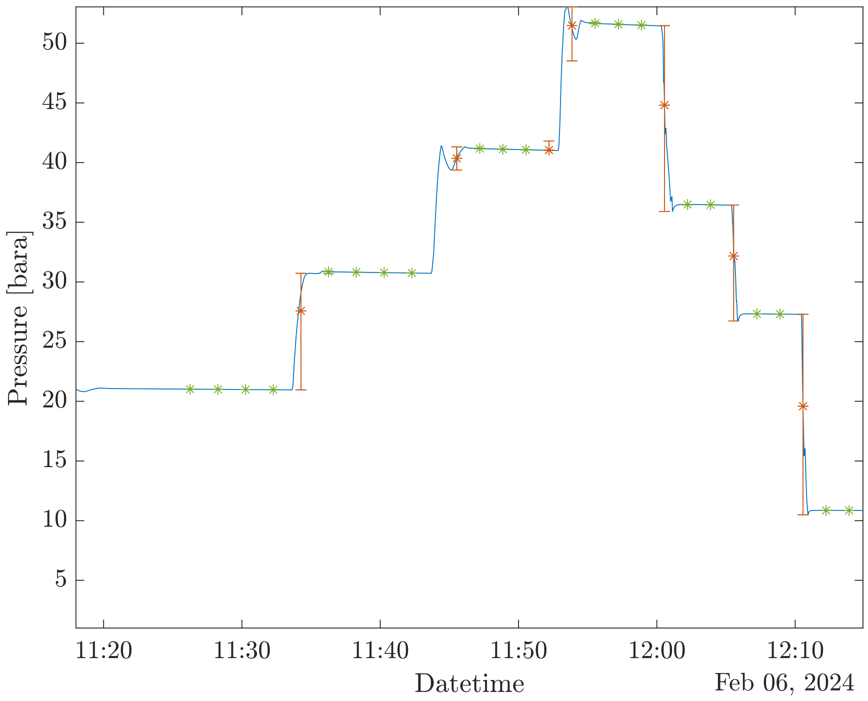

Figure 5.6: Continuous pressure measurements of N_2 (blue) and average pressure during individual measurements (red) at half-time including error bars for minimum and maximum pressure.

5.3.2 Measured Resonance Frequency

The reflection coefficient raw data were plotted in MATLAB in a logarithmic scale, as shown for the N_2 measurements from the first measurement series in Figure 5.7. Figure 5.8 shows the same plot, but with a narrowed down frequency range, showing TM_{014} mode. Here, the arrows show the approximate corresponding average pressure p_{avg} at which the measurements were taken, mirroring the changes in resonance frequency. The reflection coefficient data are plotted for all gas experiments at the full frequency range in Appendix D, and in a narrow frequency range, showing TM_{014} mode, in Appendix E.

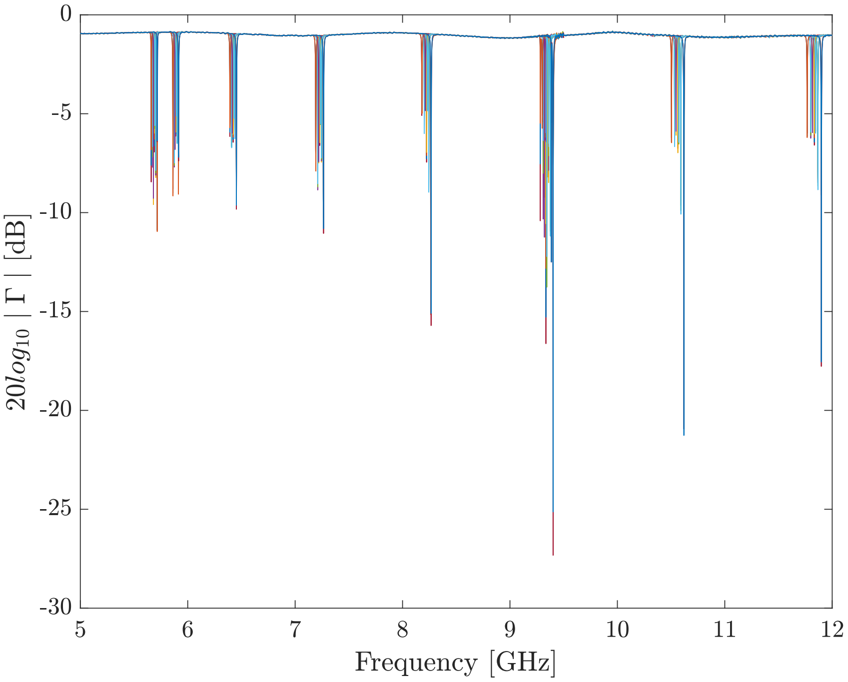

Figure 5.7: Logarithmic reflection coefficient for February 6th N_2 measurements with stable pressure along the frequency range.

As seen in Figure 5.8, an increase in pressure results in a reduced resonance frequency. In order to automatically find the measured resonance frequencies f_m for each measurement and mode, the measurements were iterated over, and the individual minimum points for every mode were collected.

5.3.3 Theoretical Resonance Frequency

The theoretical modes calculated from Eq. 2.58 were matched with the appearing modes in Figure 5.7. The variables used were the permeability μ, which was assumed equal to 1 for the gases used in this work, the theoretical dielectric constant ε_t, the

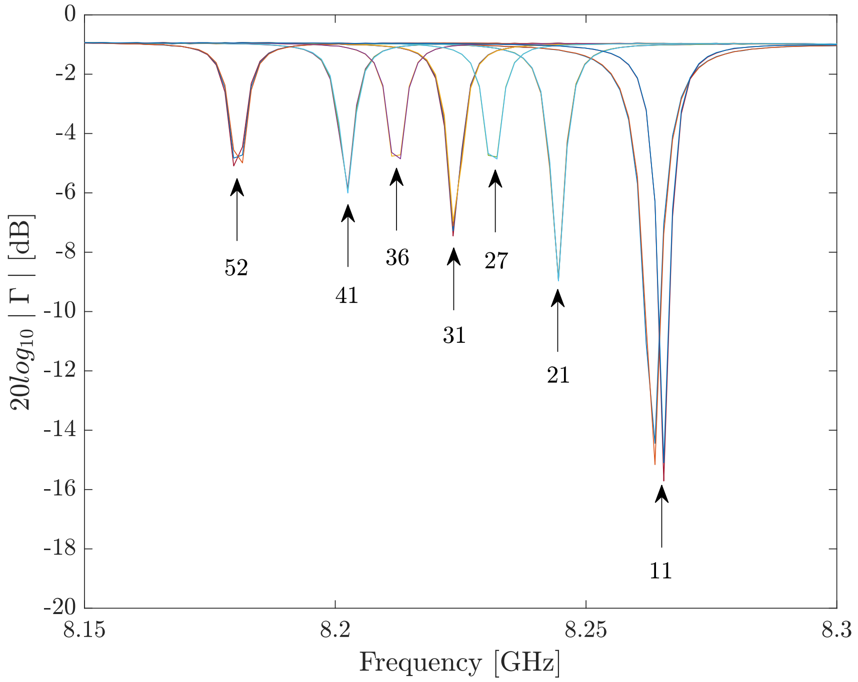

Figure 5.8: Logarithmic reflection coefficient for measurement series 1 N_2 measurements with stable pressure for a narrow frequency range, showing TM_{014} mode. Arrows showing the corresponding pressure [bara].

temperature T, and the internal dimensions $a = 0.02$ m and $l = 0.1$ m. It was found that the appearing modes were TM_{01X}, with $0 < X < 7$. In addition, there were some interfering modes in the frequency range of 9−9.5 GHz, discussed further in Section 6.1.1. The theoretical resonance frequencies f_t for modes $TM_{010}-TM_{017}$ were then calculated for all gas measurements at each value of ε_t. The measured and theoretical resonance frequencies are plotted together and discussed in Section 6.1.

5.3.4 Measured Dielectric Constant

In order to calculate the measured relative dielectric constant for a sample gas, Eq. 2.74 was used. The N_2 measurements in the corresponding experiment were used as the reference gas for CO_2 and the N_2/CO_2 mixture. Since the measurements of resonance frequencies for the reference gas and the sample gas were not performed at the exact same pressures, the resonance frequency of N_2 was found by linear interpolation over the measured resonance frequencies for each frequency mode, finding the resonance frequencies at the pressure points at which the measurements of the sample gas were taken. Then, the measured relative dielectric constant values were found for each mode as a function of pressure. The measured and theoretical dielectric constants are plotted and discussed in Section 6.2.

Chapter 6

Results and Discussion

6.1 Resonance Frequency

6.1.1 Resonance Frequency

The measured resonance frequencies $f_m(p)$ for all gas measurements were plotted in Figure 6.1 below. $N_{2,1}$ and $CO_{2,1}$ denote the measurements from the first measurement series, while $N_{2,2}$, $CO_{2,2}$ and Mix_2 denote the measurements from the second measurement series, where Mix_2 is the N_2/CO_2 mixture. Only measurements with $p_{\text{diff}} < 0.2$ are included. The calculated theoretical values for resonance frequency $f_t(p)$ are also included. The theoretical values for resonance frequency are based on an ideal cylindrical cavity, with perfect dimensions and a perfectly smooth internal surface, experiencing no losses, no temperature fluctuations, or external interferences. The theoretical value of the N_2/CO_2 mixture assumes the mixture to be in an exact 0.2/0.8 ratio.

Each plot in Figure 6.1 shows a frequency range depicting the different resonance modes, from TM_{010} to TM_{017}. The gas composition of CO_2 causes it to have a generally lower resonance frequency than that of N_2, while the resonance frequency of the N_2/CO_2 mixture lies in between, but closer to N_2.

As shown for f_t, the temperature difference between the two measurement series, from 20.8 °C to 21.1 °C, is almost negligible. At 1 bar, there is zero difference between f_t at different temperatures, while at maximum pressure, the change in temperature contributes to a change in f_t of 130 kHz for N_2 and 460 kHz for CO_2. This is the maximum change, occurring at TM_{014} mode.

By studying f_m, it appears that the least stable resonance frequencies occur for TM_{015} mode. The reason for this is that there are other interfering modes in the frequency

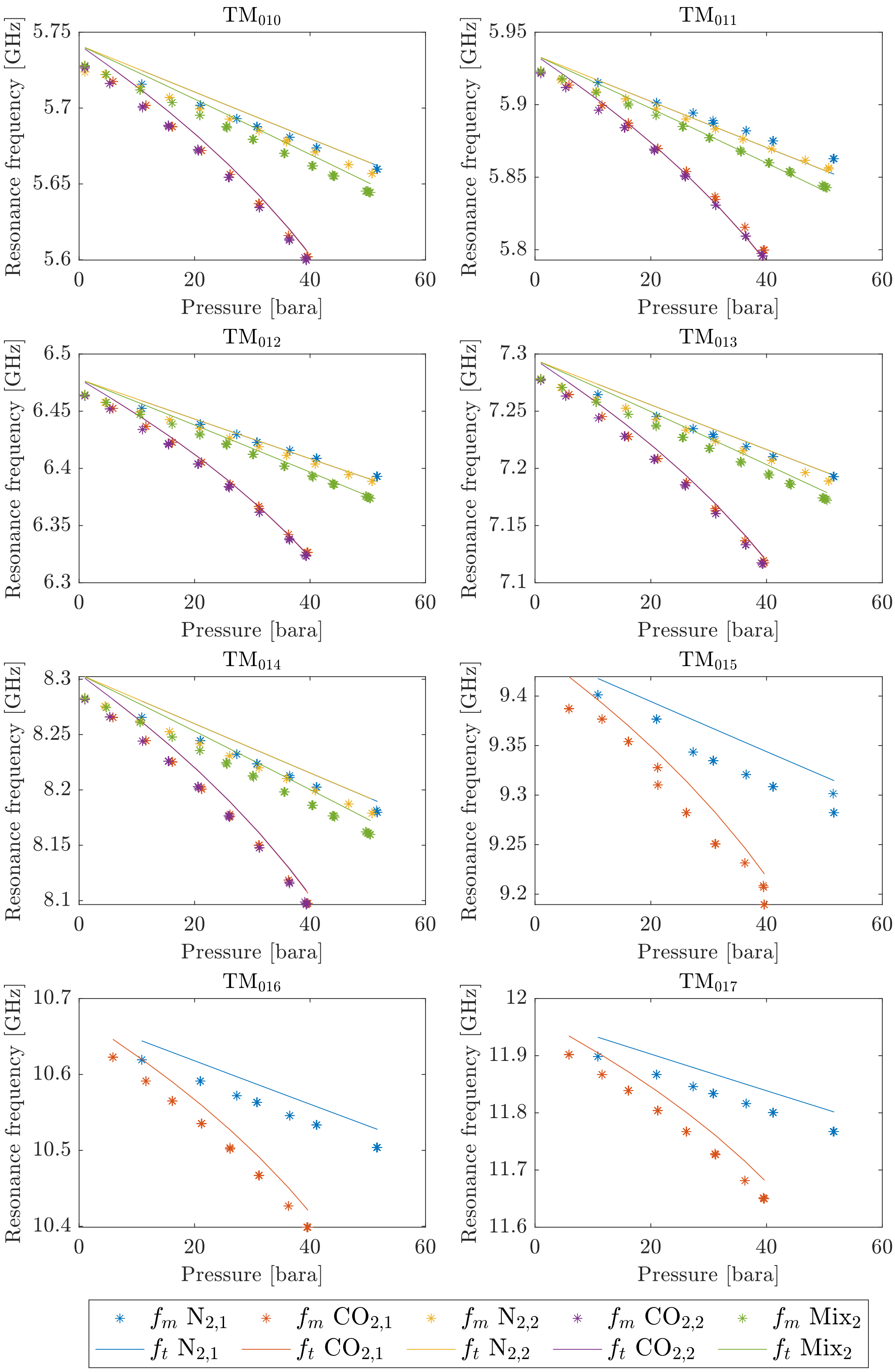

Figure 6.1: Measured and theoretical resonance frequency for TM$_{010}$-TM$_{017}$ mode of N$_{2,1}$, CO$_{2,1}$ from experiment 1, and N$_{2,2}$, CO$_{2,2}$, and Mix$_2$ from experiment 2.

range 9.1-9.5 GHz most likely caused by asymmetry in the measurement cavity. By studying the resonance frequencies of some nearby modes, the interfering modes were possibly identified to be either TM_{111} or TE_{011}, which are both located at a slightly lower resonance frequency than TM_{015}. As discussed in Section 3.3, TM modes are most likely to be prevalent in the cavity when the antenna is placed at an end-plate, but it is not impossible for TE modes to also occur. The remaining modes however, have stable resonance frequency curves.

As shown, there is a shift occurring between the measured resonance frequencies from the first to the second measurement series, as can be seen for the N_2 and CO_2 measurements. The reasons for this might be due to: (1) asymmetry from readjusting length of the cylinder, (2) asymmetry from readjusting the antenna, and/or (3) calibration fault and uncertainty within the vector network analyser. The network analyser will drift over time and it's measurements are sensitive to temperature. In this scenario, the VNA was turned on for a while before starting the measurements to reach its normal temperature, thus this is the least likely cause of the three. The most likely cause are both 1 and 2, which are investigated below.

Evaluating the Equation 2.58 for calculating the theoretical TM_{niq} modes, it is apparent that the TM_{010} mode is independent from the length l, as mentioned in Section 3.3, because of its lack of changing cycles in z-direction. Since TM_{010} mode is theoretically independent of the length, an attempt was made for TM_{010} mode to change the radius a in order to analyse the cause of the offset between the two measurement series. In reality, a change in a is unlikely, but it will shown whether some of the shift is caused by readjustments of the antenna. The radius from the first measurement series was adjusted to $a = 20.03$ mm, while the second measurement series was adjusted to $a = 20.04$ mm. The new values are shown for N_2 and CO_2 in Figure 6.2.

Since TM_{010} experiences a shift, it is likely due to the readjustment of the probe antenna. Readjustments of the probe can have a big effect on the measurements, making a change in the field patterns, as explained in Section 2.6.3. This is not to say that the general shift is not also caused by changes in the length, or small drifts from the vector network analyser. As shown in Figure 6.2, because of its larger format, the theoretical values matches the measured values best for low pressures. This indicates that the measurements for some of the modes, including TM_{010} mode, are more pressure dependent, which is discussed further in Section 6.1.2.

In conclusion, changes in the field pattern due to readjustments will change the resonance frequency significantly. Thus it in further measurements, it should be considered whether the measurement cell and antenna should be remounted between measurement

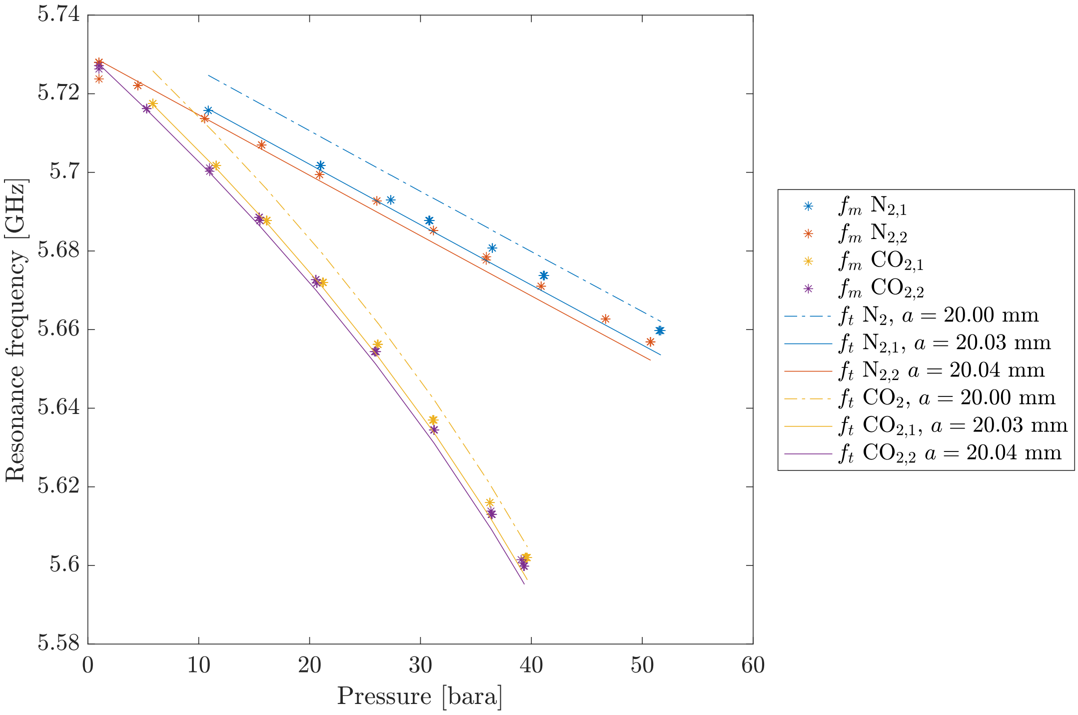

Figure 6.2: Measured resonance frequency f_m and theoretical resonance frequency f_t for N_2 and CO_2 at TM_{010} mode for the original radius and adjusted radii a and $l = 100$ mm.

series. If they are remounted, it is likely that a calibration procedure will be necessary.

6.1.2 Resonance Frequency Offset

The offset Δf_r between the theoretical resonance frequency f_t and the measured resonance frequency f_m is plotted against pressure for modes TM_{010}-TM_{017} in Figure 6.3. In calculating the theoretical values, the original values of $a = 0.02$ m and $l = 0.1$ m were used.

As shown, each measurement series has a consistent offset which degenerates in different ways for each mode. Modes TM_{010}-TM_{014} show a systematic behaviour, with $\Delta f_r = f_t(p) - f_m(p)$ decreasing with increasing pressure, indicating that f_m increases in comparison to f_t with the increasing pressure. Some pressure-dependent factors that might affecting these modes are: (1) dimensional changes by thermal expansion or contraction, as explained in Section 3.1.4, (2) mechanical stress or strain due to increased pressure, as explained in Section 3.4, and/or (3) non-ideal gases, as explained in Section 2.6.3. These factors are discussed below.

Firstly, in order for the system to undergo any significant thermal expansion, the pressure would have to be increased so rapidly that the quick compression of gas would

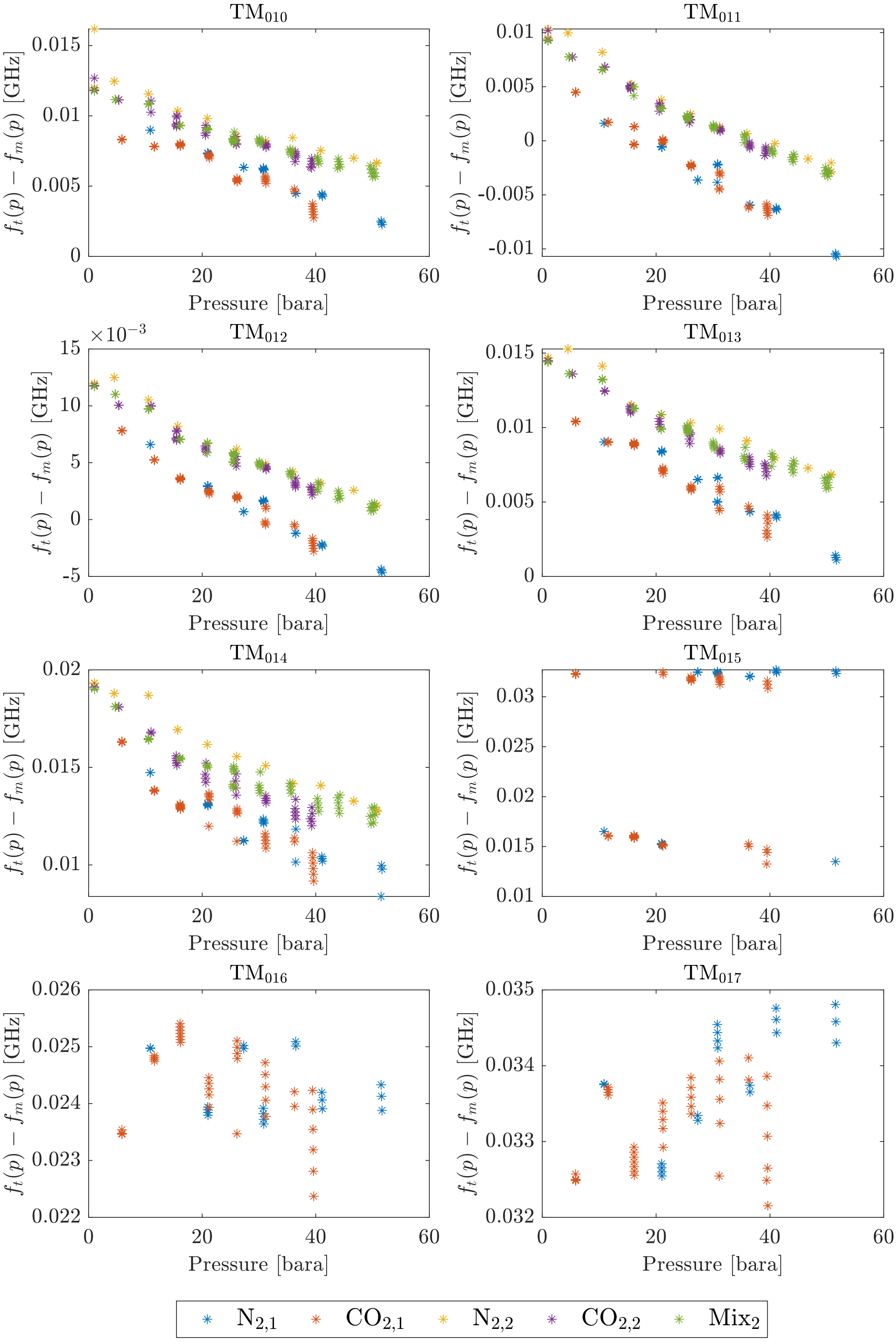

Figure 6.3: Offset between theoretical resonance frequency f_t and measured resonance frequency f_m for TM$_{010}$-TM$_{017}$ mode of $N_{2,1}$, $CO_{2,1}$ from experiment 1, and $N_{2,2}$, $CO_{2,2}$, and Mix$_2$ from experiment 2.

cause a significant temperature increase within the cavity. In the first measurement series, the pressure was adjusted incrementally, firstly increasing, then decreasing the pressure. In the second, the pressure was increased to maximum pressure, then decreased. In executing the pressure increases, it was performed in a slow manner in order to minimize this effect. Thus it is unlikely that a temperature change would cause any significant thermal expansion in the metal. Aluminium alloy 6082 also has a high conductivity, thus an increase in temperature would likely also decrease rapidly, thus not causing the consistent pattern seen in Figure 6.3.

Secondly, mechanical stress and strain from internal pressure can cause expansion or contraction in longitudinal or radial direction. Both Royal (2000) and Vanzura, Geyer, and Janezic (1993) state in their analyses about the sources of non-ideality in measured resonance frequencies for cylindrical cavities, that dimensional changes is the most significant source. Lower-order frequency modes are generally more sensitive to dimensional changes because of their simpler mode patterns, as explained in 2.6.3. However, by studying Equation 2.58, it is apparent that the resonance frequencies of an ideal cylindrical cavity are inversely proportional to a and l. Thus in theory, when increasing the dimensions as a function of pressure, f_t decreases, thus not explaining the Δf_r decreasing against pressure for modes TM_{010}-TM_{014}.

Lastly, the final pressure-dependent mechanism is the effect of gases behaving non-ideally, as explained in Section 2.6.3. At higher pressures, the non-ideality of a gas in a cylindrical cavity resonator generally contributes to a lower measured microwave resonance frequency. Thus, this explanation does not completely account for the pressure dependency observed in lower frequency modes.

As for mode TM_{015}, there are likely one or more interfering modes disrupting the signal, as discussed in Section 6.1.1. When looking at the offset of TM_{016} and TM_{017} mode, they seem to be less affected by the pressure-dependency affecting $\text{TM}_{010}-\text{TM}_{014}$ mode. This agrees with the fact that higher-order modes generally are less sensitive to pressure because of their complex mode field patterns, as explained in Section 2.6.3. Although TM_{016} and TM_{017} mode have closely gathered Δf_r points, they do however have an increasing offset with TM_{016} below 0.026, and TM_{017} below 0.035, indicating that f_m might be subject to frequency-dependent perturbation mechanisms. As explained in Section 2.6.3, higher order modes are generally more sensitive to imperfections or asymmetries such as those introduced by coupling apertures because of their complex field patterns. This phenomenon might cause some offset, but it is difficult to account for without conducting more experiments on these modes.

Another frequency-dependent perturbation mechanism mentioned in 2.6.3, is the skin depth perturbation. As explained, it affects the low frequencies more because of the larger wavelengths entering the metal. The skin depth perturbation was calculated for the minimum frequency, 5 GHz, to calculate the maximum impact. Entering for relative permeability $\mu_r = 1$, permeability of vacuum $\mu_0 \approx 1.2566371 \times 10^6$ H/m, and conductivity of aluminium alloy 6082 $\sigma = 3 \times 10^7$ S/m, the skin depth perturbation comes out to 1.3×10^{-6} m or 0.0013 mm (Astrup 2023). This is not an extremely significant impact when comparing f_t to f_m, however it can easily be adjusted for in future measurements.

In conclusion, it is apparent that the measured resonance frequency is a factor of many non-ideal mechanisms separating it from the theoretical value, making it a complex issue. The lower-order modes are more sensitive to the overall geometry in the cavity, while higher-order modes are more sensitive to local imperfections or asymmetries, such as those introduced by coupling apertures. Even though the exact causes of the offset between theoretical and measured resonance frequencies were not found, it seem to be systematic for all gases at both measurement series. The systematic offsets can be used for calibration and fine-tuning of the system in further testing.

6.2 Dielectric Constant

6.2.1 Dielectric Constant

The measured dielectric constant $\varepsilon'_m(p)$ is plotted for $\mathrm{CO}_{2,1}$, $\mathrm{CO}_{2,2}$, and Mix_2 in Figure 6.4. The theoretical dielectric constants $\varepsilon_t(p)$ found for the same temperatures and pressures from TREND are also plotted. Since mode TM_{015} have interfering modes close to it, it is not included. $\mathrm{TM}_{010}-\mathrm{TM}_{014}$, TM_{016} and TM_{017} are included.

As shown, the measured relative dielectric constants $\varepsilon'_m(p)$ match up well with the theoretical relative permittivity $\varepsilon_t(p)$. By calculating the dielectric constant as a ratio of two gases from the same experiment, this reduces the effect of most pressure-dependent and frequency-dependent mechanisms which affected the resonance frequency offset values. The only effect not fully accounted for is the non-ideality of the individual gases.

Ideally, the N_2 measurement from one experiment could be used as a general reference gas for both experiments. Because of the uncertainty from the resonance frequency shift described in Section 6.1, it will give highly inaccurate results in this case.

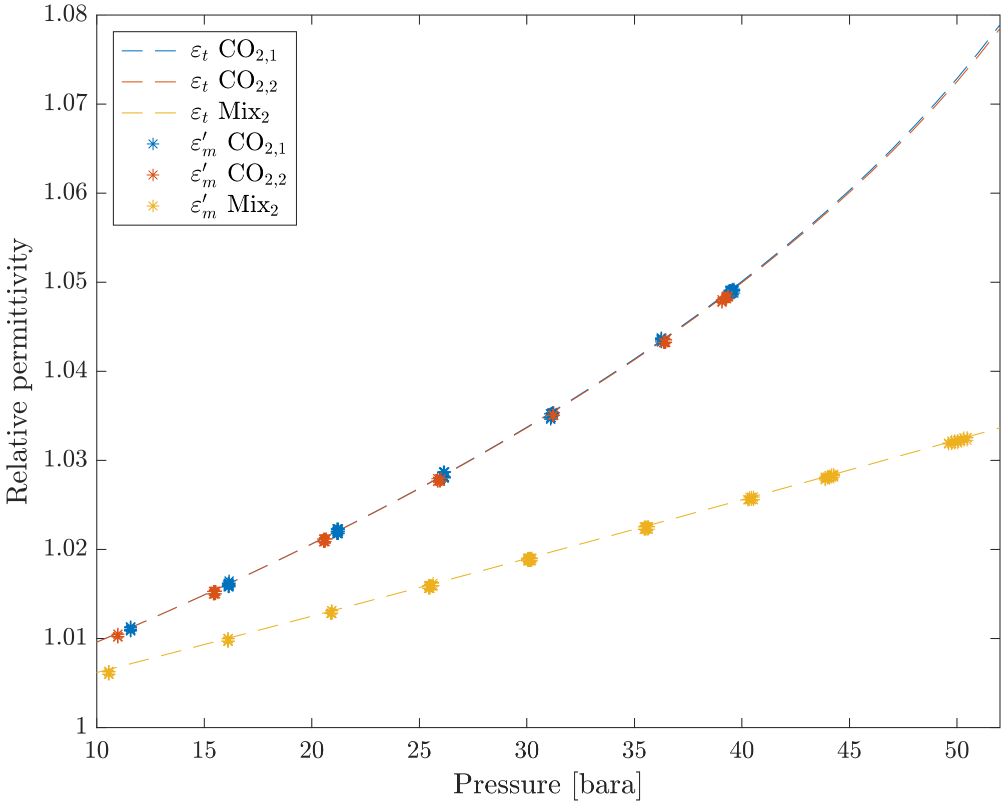

Figure 6.4: Measured real part of the dielectric constant ε'_m and theoretical dielectric constant ε_t against pressure for $CO_{2,1}$, $CO_{2,2}$, and Mix_2 with N_2 from the corresponding experiment as the reference gas.

6.2.2 Dielectric Constant Offset

Figure 6.5 shows the dielectric constant offset $\Delta\varepsilon_r$ between the theoretical relative permittivity $\varepsilon_t(p)$ and the measured real part of relative permittivity $\varepsilon'_m(p)$ for $CO_{2,1}$, $CO_{2,2}$, and Mix_2 plotted against pressure for modes $TM_{010}-TM_{014}$, TM_{016} and TM_{017}.

As shown, the offset is small with values consistently below 8×10^{-4}, but with the majority of values below 4×10^{-4}. The offset is a little lower for high pressures in comparison to low pressures, specifically in the $CO_{2,2}$ and Mix_2 measurements. This is likely caused by the increased spread of ε_r for higher pressures, as described in Section 4.1, and agrees with the comparative studies performed in Section 3.1.3. Inaccurate resonance frequency measurements might also be generating some deviating offset values, perhaps contributing to the offsets at high-pressure for $CO_{2,1}$. $\Delta\varepsilon_r$ is positive for the most part, meaning that the theoretical dielectric constant is generally slightly higher than the measured dielectric constant. The reason for this might be contributed to a few factors.

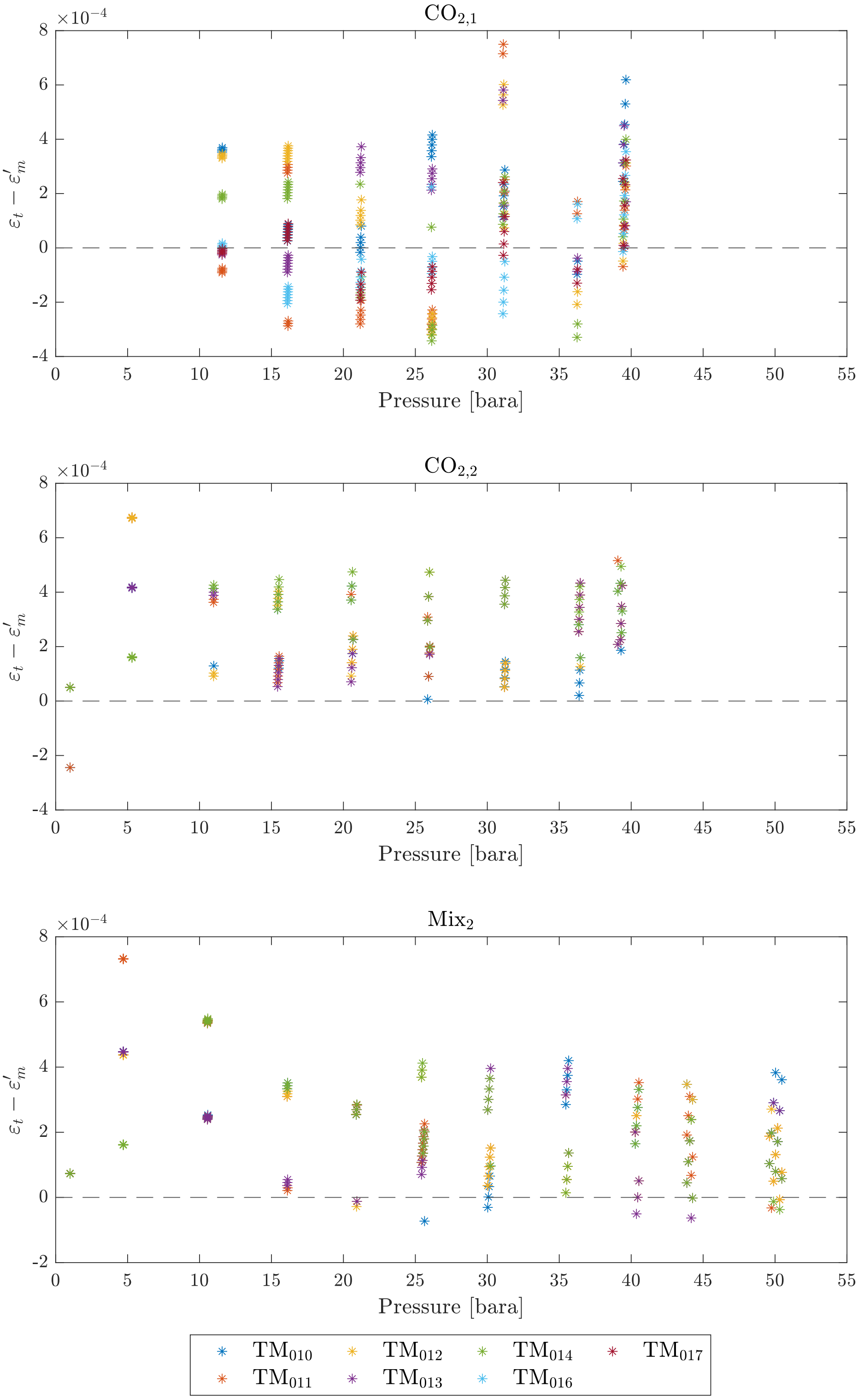

Figure 6.5: Offset between measured and theoretical permittivity for $CO_{2,1}$, $CO_{2,2}$, and Mix_2 for modes TM_{010}−TM_{014}, TM_{016} and TM_{017} against pressure.

Firstly, as mentioned, there might be a non-ideality of each individual gas which is not accounted for.

Secondly, there might be a very small loss factor $j\varepsilon_r''$, as discussed in Section 2.2. But as discussed, the loss factor is generally almost negligible for non-polar and weakly-polar gases. Though difficult to quantify for these kinds of gases, the loss factor of each gas would likely increase with ε_r' due to the increasing pressure. For this reason, the loss factor is not considered the main cause of the offset.

Lastly, Equation 2.74 used for calculating the measured dielectric constant uses a normalisation procedure which adjusts the measurements based on the reference gas. If the perturbation mechanisms depend in some way of the dielectric constant, then the normalisation will not compensate fully, and the error will increase for gases with a deviating dielectric constant from the reference gas. In order to solve this issue, adjustments can be done using a calibration of multiple reference gases with known dielectric constants to improve accuracy across a range of measurement conditions.

The offset $\Delta\varepsilon_r$ was also plotted with frequency on the x-axis, in order to highlight the accuracy of each resonance frequency mode, as shown in Figure 6.6. As shown, the offset is highest for the lower-order modes, and lowest for the higher-order modes. This can be explained by the offset of resonance frequency being more consistent for the higher-order modes, as explained in Section 6.1.2. The lower-order modes also generally have more outliers. However, the offset results vary slightly for each gas measurement.

As shown, there is a systematic deviation towards positive values especially for $\mathrm{CO}_{2,2}$ and Mix_2, which perhaps can be calibrated for. The offset is used as an estimate of the uncertainty, with $\pm 4 \times 10^{-4}$ for lower-order modes, and $\pm 2 \times 10^{-4}$ for higher-order modes. Combining the data from Figure 6.5 and 6.6, it is a general trend that the highest offset values occur for the lower-order modes at low pressures. Repeated measurements would be needed to confirm this hypothesis.

The decision of excluding the higher-order modes was made at a point where there was a timing issue in the data processing, causing there to be seemingly more interfering modes for the higher-order modes. In future measurements, it would be interesting to observe the behaviour of the higher-order modes, TM_{016} and TM_{017}, further.

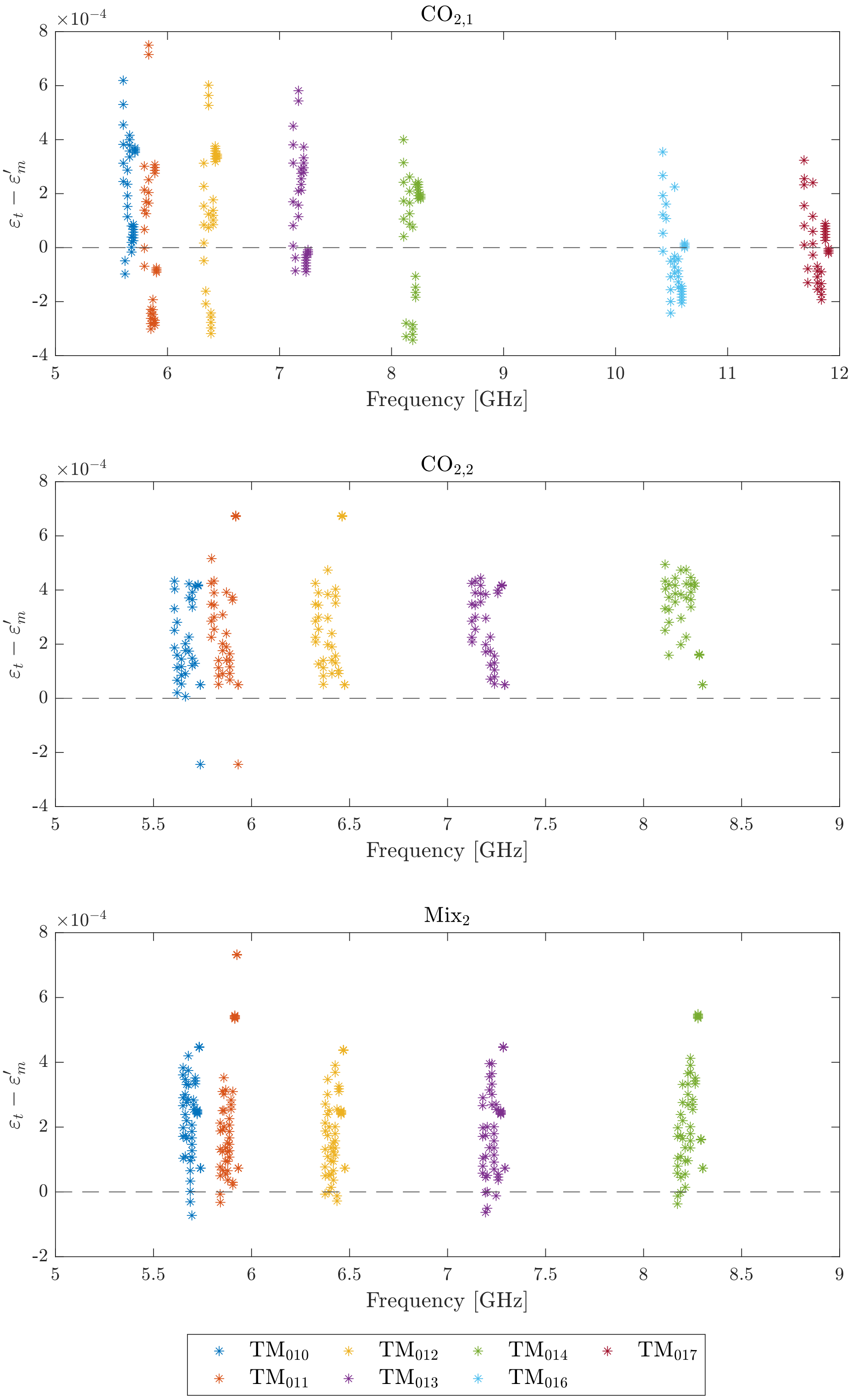

Figure 6.6: Offset between measured and theoretical permittivity for CO$_{2,1}$, CO$_{2,2}$, and Mix$_2$ for mode TM$_{010}$-TM$_{014}$ against frequency.

6.3 Increasing Measurement Accuracy

In this section, several strategies to enhance the accuracy of the dielectric constant measurements obtained through the cylindrical cavity resonator system are discussed. Given that the calculations of the dielectric constant directly depend on the resonance frequency measurements, it is important to identify the sources influencing the measured resonance frequency.

Firstly, more measurements should be conducted in order to evaluate the reproducibility of the measurement system. With more testing performed on the system, it should be confirmed or denied whether the frequency shift observed between measurement series 1 and 2 occurred solely to the remounting of the measurement system. A suggestion might be to test with and without remounting and analyse the influence on the results. This would help analyse the effect of remounting and the reproducibility of future measurements.

As noted in 6.1.2, each measurement series exhibited a remarkably consistent resonance frequency offset, indicating a consistent offset phenomenon. The sources of errors should be continuously mapped in order to identify the exact sources affecting each experiment. It could be beneficial to apply a modeling approach to systematically track and minimize these errors.

Regarding the external influences from temperature and pressure, the control and monitoring of these could be significantly improved in future measurements. By placing a thermostat nearer to the measurement cell, the temperature reading can be accounted for more accurately. The addition of a pressure vessel will also significantly reduce external disruptions, nearly eliminating the dimensional changes, thus reducing one of the potentially main sources of disturbance to the measured resonance frequency. If enough repeated measurements are conducted, then an alternative method to a pressure vessel would be to create a calibration which corrects for the pressure effects on the resonance frequency offset.

It is also important to note that the vector network analyzer used in this work is highly sensitive to temperature fluctuations, which can cause drifts in the measurements. To counteract this, a dedicated transmitter could be made in the long term. This would emit a signal at a specified frequency, with a receiver to detect the signal's strength. The frequency of the signal would then be fine-tuned until the received signal level reaches a maximum or minimum value.

6.4 Dielectric Constant of Hydrogen

As discussed in Section 4.1, the dielectric constant of H_2 at 100 bar equals the dielectric constant of N_2 at 43 bar, and of CO_2 at 22 bar. In Section 4.2, it was stated that at 100 bar and 20 °C, an increase of 0.01 mole fractions CH_4 into pure H_2 increases in the dielectric constant by 5.4×10^{-4}. As the dielectric constant offset in this study was highly consistent both for CO_2 and the N_2/CO_2 mixture, an assumption can be made for measurements on hydrogen and its impurities. It can be assumed that hydrogen mixtures also will be measured with the uncertainty of $\pm 2 \times 10^{-4}$ for higher-order modes in a high-pressure system up to 100 bar. By comparing these values, it gives an indication about the amount of an impurity that can be measured accurately in H_2. An impurity of CH_4 in H_2 can then be measured accurately down to a purity of 0.0074 mole fractions or a mole percent of 0.74%.

A remark that might affect H_2 measurements in particular is that, as pointed out in Section 5.2.3, the small size of H_2 molecules might make them more prone to leak through small gaps in the measurement cell. As pointed out, the CO_2 measurements seemed to be less affected by small leakages in the system under high pressure than N_2. The molecular structure of H_2 is even smaller than that of N_2. That might cause challenges in measuring H_2, both with an increase in the p_{diff} increasing in a singular measurement, but most importantly, the leakages might impose a hazard. The small volume of the cylindrical cavity is on the other side beneficial in measuring on H_2, imposing less of a hazard. Either way, measurements using H_2 will require high caution and impose stronger safety protocols because of the explosion danger associated with it.

In concluding remarks, this dielectric constant uncertainty found in this work is far from the impurity requirements in the international standard ISO 14687:2019 (International Organization for Standardization 2019). However, the method can still be very useful in a broader application, for example by measuring hydrogen impurities in combination with other measurement technologies.

Chapter 7

Conclusions and Future Work

7.1 Conclusion

This master's thesis has successfully developed and tested a cylindrical cavity resonator for measuring the purity of various gases. The measurement cell was made with an internal volume of 125.66 cm^3, and was constructed from aluminium alloy 6082, known for its high conductivity and resistance to hydrogen embrittlement.

The system was evaluated using N_2, CO_2, and an N_2/CO_2 mixture under pressures ranging from 1 to 50 bar at room temperature. Across two measurement series spanning frequencies of 5 – 12 GHz and 5 – 9 GHz respectively, resonance frequencies for modes TM_{010} to TM_{017} were observed, aligning well with theoretical predictions. Notably, a shift between measurement series was likely caused by the remounting of the measurement cell. The offset from theoretical values was also analysed, revealing that the lower-order modes are more pressure-dependent, likely being more affected by perturbation mechanisms such as geometric deformations and non-ideal gas behaviour. The higher-order modes were more affected by frequency-dependent perturbation mechanisms such as conductivity loss.

Reference measurements with N_2 enabled the determination of the dielectric constants for CO_2 and the N_2/CO_2 mixture with approximate uncertainties of $\pm 4 \times 10^{-4}$ for lower-order frequency modes and $\pm 2 \times 10^{-4}$ for higher-order frequency modes. Comparative studies revealed that at 100 bar, the dielectric constant of H_2 matches those of N_2 at 43 bar and CO_2 at 22 bar. Additionally, a 0.01 mole fraction increase of CH_4 in H_2 raises the dielectric constant by 5.4×10^{-4} at 100 bar and 20°C. Comparatively, when assuming a $\pm 2 \times 10^{-4}$ uncertainty in the dielectric constant of H_2, it suggests that accurate measurements of impurities in H_2 is feasible using this measurement technology.

A key remark during measurements was however, that the N_2 measurements seemed to be leaking more through the small gaps of the system. If this is the case, then is even more likely to affect H_2 measurements because of its even smaller molecular structure. This raises concerns about the environmental safety due to the explosive nature of hydrogen.

The insights gained and methodologies developed offer substantial potential for broader applications in quantifying the impurities in H_2. This research paves the way for integrating these methods with other advanced measurement technologies, potentially enhancing the precision and reliability of hydrogen quality assessment. Further strategies for improving accuracy and reducing uncertainties include mapping out errors, and controlling or calibrating for external influences.

In final words, the cylindrical cavity resonator measurement system holds promise as an effective tool for assessing impurities in H_2, given its accuracy, compact volume, and closed environment. Initial results indicate the systems capability for precise impurity detection, with potential for enhanced performance through system refinement.

7.2 Future Work

Some suggestions for future works are provided.

- More quantitative measurements need to be performed to see if the measurement errors repeats themselves and and to see if the hypothesis' proposed in this work are viable.
- Creating a calibration which corrects for the resonance frequency offset mechanisms.
- Narrowing the frequency range and decreasing the IF bandwidth will be helpful in increasing the accuracy of the resonance frequency measurements, perhaps to the frequency range 10-12 GHz, where the modes are seemingly less pressure-dependent than lower modes.
- If needed, then the system can be pressure tested again using a hydrostatic method up to 120 bar, following the procedure in Appendix B.
- After more testing on non-explosive gases, the system can be tested on H_2. A careful safety evaluation has to be made in advance, and all equipment and environments need to be approved to use in potentially explosive atmospheres. If

pressure tested up to 120 bar, the H_2 measurements can be performed with up to 75 bar if considered safe.

- Create a system with a dedicated transmitter to replace the vector network analyser, as explained in Section 6.3

In the long term, the aim for the measurement system is to use the resonator technology in combination with acoustic and optical measurements, thus giving more efficient measurements of the quality of the hydrogen and thereby contribute to meet the objectives of a long-term growth in the application of this energy bearer.

References

AIR-WAY Global Manufacturing (2024). Technical data tubing pressure ratings.

AMETEK, Inc. (2023). Precision metering pumps quizix qx series. 1M1220A (360017).

ASTM International (2007). “Standard specification for carbon and alloy steel externally threaded metric fasteners (metric)”. In: Designation: f568m 07.

Astrup (2023). Aluminium bolt. URL: https://astrup.no/Materialer-Produkter/Materialer/Aluminium/Aluminium-bolt (visited on 12/05/2023).

Autoclave Engineers (Jan. 2013). Adapters/couplings. 02-0127SE.

Bacquart, Thomas et al. (2018). “Probability of occurrence of iso 14687-2 contaminants in hydrogen: principles and examples from steam methane reforming and electrolysis (water and chlor-alkali) production processes model”. In: International journal of hydrogen energy 43.26, pp. 11872–11883.

Bentley, John P (2005). Principles of measurement systems. Pearson education.

Callister, William D et al. (2007). Materials science and engineering: an introduction. Vol. 7. John wiley & sons New York.

Chen, Lin-Feng et al. (2004). Microwave electronics. John Wiley & Sons.

Cole, Kenneth S and Robert H Cole (1941). “Dispersion and absorption in dielectrics i. alternating current characteristics”. In: The journal of chemical physics 9.4, pp. 341–351.

Debye, Peter (1929). “Polar molecules. by p. debye, ph. d., pp. 172. new york: chemical catalog co., inc., 1929. 3.50”. In: Journal of the society of chemical industry 48.43, pp. 1036–1037.

Dichtomatik (2010). Werkstoff-datenblatt material data sheet. FP 809402.

Equilibar (Apr. 2021). Mity mite back pressure regulator replacement.

European Commission (2020). “Communication from the commission to the european parliament, the council, the european economic and social committee and the committee of the regions a hydrogen strategy for a climate-neutral europe”. In.

Ewing, MB and DD Royal (2002a). “A highly stable cylindrical microwave cavity resonator for the measurement of the relative permittivities of gases”. In: The Journal of Chemical Thermodynamics 34.7, pp. 1073–1088.

– (2002b). “Relative permittivities and dielectric virial coefficients of nitrogen at t= 283.401 k and t= 303.409 k determined using a cylindrical microwave cavity resonator”. In: The journal of chemical thermodynamics 34.12, pp. 1985–1999.

Folgerø, Kjetil et al. (2019). “Combined thickness and permittivity measurement of thin layers with open-ended coaxial probes”. In: Sensors 19.8, p. 1765.

Goodwin, Anthony RH, James B Mehl, and Michael R Moldover (1996). “Reentrant radiofrequency resonator for automated phase-equilibria and dielectric measurements in fluids”. In: Review of scientific instruments 67.12, pp. 4294–4303.

Greenwood, Norman Neill and Alan Earnshaw (2012). Chemistry of the elements. Elsevier.

Griffiths, David J (2023). Introduction to electrodynamics. Cambridge University Press.

Harvey, Alan H and Eric W Lemmon (2005). “Method for estimating the dielectric constant of natural gas mixtures”. In: International journal of thermophysics 26, pp. 31–46.

Haukalid, Kjetil and Kjetil Folgerø (2016). “Broad-band permittivity measurements of formation of gas hydrate layers using open-ended coaxial probes”. In: Energy & fuels 30.9, pp. 7196–7205.

Hertz, Heinrich (1893). Electric waves. Dover Publications.

International Organization for Standardization (2019). Iso 14687: 2019.

Ishii, T Koryu (1995). Handbook of microwave technology. Elsevier.

Kandil, Mohamed E, Kenneth N Marsh, and Anthony RH Goodwin (2005). “A re-entrant resonator for the measurement of phase boundaries: dew points for {0.4026 ch4+ 0.5974 c3h8}”. In: The journal of chemical thermodynamics 37.7, pp. 684–691.

Kano, Yuya (2021). “Multi-property evaluation for a gas sample based on the acoustic and electromagnetic resonances measurement in a cylindrical cavity”. In: The journal of chemical thermodynamics 159, p. 106448.

Kemlon Products (1999). Kemtite high pressure connectors pms. URL: https://www.kemlon.com/catalogs/kemtite/pms/pms.html (visited on 05/03/2024).

Keysight Technologies (2019). “Basics of measuring the dielectric properties of materials”. In: Keysight.

Khurmi, RS and JK Gupta (2005). A textbook of machine design. S. Chand publishing, pp. 233–239.

Lee, Jonathan A and Stephen Woods (2016). “Hydrogen embrittlement”. In.

Masikh, Qayssar Saeed, Mohammad Tariq, and Prabhat Kumar Sinha (2014). "Analysis of a thin and thick walled pressure vessel for different materials". In: Int. j. mech. eng. technol 5.10, pp. 9–19.

May, EF et al. (2004). "An improved microwave apparatus for phase behaviour measurements in lean gas condensate fluids". In: Fluid phase equilibria 215.2, pp. 245–252.

May, Eric F, Michael R Moldover, and James W Schmidt (2009). "Reference measurements of hydrogen's dielectric permittivity". In: Molecular physics 107.15, pp. 1577–1585.

May, Eric F et al. (2001). "Development of an automated phase behaviour measurement system for lean hydrocarbon fluid mixtures, using re-entrant rf/microwave resonant cavities". In: Fluid phase equilibria 185.1-2, pp. 339–347.

Moss, Dennis R (2004). Pressure vessel design manual. Elsevier.

National Archives (2024). Code of federal regulations. URL: https://www.ecfr.gov/current/title-49/subtitle-B/chapter-I/subchapter-C/part-180/subpart-C/section-180.209 (visited on 01/03/2024).

Nelson, Howard G (1983). "Hydrogen embrittlement". In: Treatise on materials science & technology. Vol. 25. Elsevier, pp. 275–359.

NIST (2023). Nist chemistry webbook. URL: https://webbook.nist.gov/chemistry/.

NORCE (2023). Norwegian centre for hydrogen research (hyvalue). URL: https://www.norceresearch.no/prosjekter/norwegian-centre-for-hydrogen-research-hyvalue.

Nyfors, Ebbe Gustaf et al. (2000). Cylindrical microwave resonator sensors. Helsinki University of Technology.

Paroscientific, Inc. (Dec. 2005). Digiquartz pressure instrumentation.

Petrakopoulou, Fontina and Enrique García-Tenorio (2023). "Evaluating hydrogen-based electricity". In: Energy conversion and management 293, p. 117438.

Petrescu, Camelia (2018). "Some aspects regarding the quality factor of cylindrical waveguide resonators". In: Bul. inst. politehnic din iai 64.68, pp. 47–56.

Royal, Damian Derek (2000). Dielectric constants of simple gases. University of London, University College London (United Kingdom).

Sampson, Catherine C et al. (2019). "Dielectric permittivity, polarizability and dipole moment of refrigerants r1234ze (e) and r1234yf determined using a microwave re-entrant cavity resonator". In: The journal of chemical thermodynamics 128, pp. 148–158.

Sobko, AA (2017). "Description of the pressure and temperature dependences of permittivity of nonpolar gases by the generalized van der waals- berthelot equation". In: Doklady physics. Vol. 62. 6. Springer, pp. 299–301.

Span, R et al. (2020). Trend. thermodynamic reference and engineering data 5.0. 2020.

Swagelok (Jan. 2024). Medium- and high-pressure fittings, tubing, valves, accessories. MS-02-472.

Timmerberg, Sebastian, Martin Kaltschmitt, and Matthias Finkbeiner (2020). “Hydrogen and hydrogen-derived fuels through methane decomposition of natural gas–ghg emissions and costs”. In: Energy conversion and management: x 7, p. 100043.

Tsankova, Gergana et al. (2016). “Characterisation of a microwave re-entrant cavity resonator for phase-equilibrium measurements and new dew-point data for a (0.25 argon+ 0.75 carbon dioxide) mixture”. In: The journal of chemical thermodynamics 101, pp. 395–404.

Tsankova, Gergana et al. (2017). “Densities, dielectric permittivities, and dew points for (argon+ carbon dioxide) mixtures determined with a microwave re-entrant cavity resonator”. In: Journal of chemical and engineering data 62.9, pp. 2521–2532.

Tsankova, Gergana et al. (2019). “Dew points, dielectric permittivities, and densities for (hydrogen+ carbon dioxide) mixtures determined with a microwave re-entrant cavity resonator”. In: Industrial & engineering chemistry research 58.47, pp. 21752–21760.

Vanzura, Eric J, Richard G Geyer, and Michael D Janezic (1993). “The nist 60-millimeter diameter cylindrical cavity resonator: performance evaluation for permittivity measurements”. In.

Vehoff, H (2007). “Hydrogen related material problems”. In: Hydrogen in metals iii, pp. 215–278.

Waldron, Richard Arthur (1970). “Theory of guided electromagnetic waves”. In: (no title).

Wei, Jia et al. (2020). “A review on dielectric properties of supercritical fluids”. In: 2020 ieee electrical insulation conference (eic). IEEE, pp. 107–113.

Wetegrove, Marcel et al. (2023). “Preventing hydrogen embrittlement: the role of barrier coatings for the hydrogen economy”. In: Hydrogen 4.2, pp. 307–322.

Appendix A

Safe Job Analysis (SJA)

Safe Job Analysis (SJA)

SJA title: High pressure fluid measurements	**Project no:** Generic	**Project title:** Generic
Project manager: Kjetil Folgerø	**Responsible for SJA:** Anna Mathea Skar	**Participants in the SJA:** Anna Mathea Skar, Kjetil Folgerø
Short work description Use of pressure vessel to test permittivity of non-flammable fluids		**Premises:** NORCE Bergen

No.	Task	Possible danger	Possible consequence	Recommended action
1	Hydrostatic pressure test of measurement cell	• Deformation of equipment that cannot withstand the pressure • Water leakage	• Impact damage to personnel or equipment • Damage to electrical equipment and personnel	• Follow the order of procedure (attached) and checklist (below) • Use mechanical separation between operator and measuring cell • Use safety glasses • Carry out experiments during working hours and under the supervision of a laboratory supervisor who has sufficient training for the equipment • Ensure communication with the project team, laboratory users and those affected nearby before start (and when finished) • Check that all connections to the measuring cell are securely fastened • Consider whether the measuring cell and cables should be permanently installed • Interrupt measurement in the event of a major water leak. Have fire safety equipment available • Follow a gradual pressure build-up and continuous check of the pressure gauge • Release the pressure before removing the mechanical separator • Do not put your head over the lid when opening the cylinder • Choose measures to avoid exposure to hazards, i.e. ensure that the working environment is suitable, e.g. work room, ventilation, first aid equipment

2	Initial installation	- Gas leakage may occur - High pressure produces large forces that can destroy equipment	- Health damage to personnel by inhaling gas - Impact damage to personnel or equipment	- Follow procedure and checklist - Ensure that the operator has sufficient training/knowledge - Follow the emergency shutdown procedure (below) in case of leakage or other unwanted incidents - Consider the use of mechanical separation between operator and measuring cell - Use safety glasses - Ensure communication with the project team, laboratory users and any others affected before start (and when finished) - Check that all connections to the measuring cell are securely fastened - Make sure that the gas outlet is discharged into a fume hood - Consider whether the measuring cell should be placed under extraction - Consider whether the measuring cell and cables should be fixed
3	Gas testing	- Gas leak - Deformation of equipment	- Health damage to personnel by inhaling gas - Impact damage to personnel or equipment	- Follow procedure and checklist - Ensure that the operator has sufficient training/knowledge - Follow the emergency shutdown procedure (below) in case of leakage or other unwanted incidents - Use safety glasses - Clear sign "gas under pressure" - Consider how high a pressure is necessary for the gas being measured. A goal should be to use as low a pressure as possible - If the gas leak is out of control, leave the laboratory and notify the room manager. - In case of serious personal injury, call 113 and the NORCE emergency number (21 08 01 86)
4	Disconnection	- Gas leak - Deformation of equipment	- Health damage to personnel by inhaling gas - Impact damage to personnel or equipment	- Follow procedure and checklist - Use safety glasses - Ensure communication with the project team, laboratory users and any others affected when finished - Release the pressure and ensure that the pressure has dropped to atmospheric pressure before removing the mechanical separation between operator and measuring cell

Safe Job Analysis (SJA)

Check list:

	Yes	No	Comments
Have you informed the room manager and the person in charge of emergency response for the laboratory?			**Inform room manager well in advance of the start of the experiment. Also inform when the experiment is finished**
Will the experiment be done under supervision?			**Consider supervision at high pressures and if there is a lack of sufficient training and experience with the equipment used**
Are the fluid(s) explosive?			**Follow a different/create new SJA and always conduct experiments with supervision**
Are the fluid(s) health hazardous?			**Be careful using gas exhaust hoods during gas emissions. Use a laboratory room with adequate ventilation**
Should the fluid(s) be pressurized?			**Follow the procedure and be careful with the order of procedure**
Is the gas from the measuring cell released into the exhaust before the chamber is opened or the seperator is removed?			**Check that the pressure sensor has returned to atmospheric pressure**

Emergency shutdown procedure:

1. If the gas leak is out of control, leave the laboratory and notify the room manager.
2. In case of serious personal injury, call 113 and the NORCE emergency number: 21 08 01 86

Appendix B

Procedure

This document explains the procedures that should be followed when using the cylindrical cavity sensor. This includes a procedure for hydrostatic pressure testing, one for initial installation, and one for gas measurements under pressure. The procedures should be used in combination with the safe work analysis (Appendix A). Safety glasses must be worn during all pressurized measurements. Use a laboratory with a good ventilation system that has a fume exhaust and a suitable pressure cabinet.

Hydrostatic Pressure Test

The measuring system should be pressure tested hydrostatically with 150 % of the maximum gas operating pressure, e.g. with up to 75 bar with a maximum operating pressure of 50 bar. A hydrostatic pressure test is used because water is incompressible, meaning that given a failure or rupture, the energy released is much lower than with compressed gas. This test provides no assurance that the equipment will withstand high pressure over a long period of time.

1. Mount the measuring cell on the stand. Place the sensor setup in the cabinet. Consider if the stand should be fastened to the cabinet floor.

2. Place the gas input tube from the cylinder, out of the chamber and attach to a valve before the water pump. The pipe for the gas outlet must be led from the cylinder, out of the chamber, to a valve connected to a cross-port valve, which is connected to a back-pressure regulator and a deposit. The deposit where the water comes out should end in a cup or bucket.

3. Mount the bottom lid of the cylinder securely, with the probe attached, then fill the cavity with water, as close to the top as possible. Mount the top lid securely.

4. Make sure that all connections and screws are tight before closing the chamber. If possible, make sure you can see the measurement setup inside the chamber through the glass window.

5. Increase the pressure to 5 bar. Monitor the pressure in the cylinder. Leave for 30 minutes, or more if wanted. Increase the pressure in 10 bar increments, i.e. 15 bar, 35 bar, 45 bar, 55 bar, 65 bar, and 75 bar. Leave for 30 min for each interval and make sure that the pressure does not drop significantly. If the pressure drops too much, there might be a leak. If so, stop the test, look for visible leakage in the pipes and valves outside the chamber. If there is no leak outside, it might be inside. In that case, release the pressure, open the chamber and tighten the screws and connectors again. Start the pressure test again.

6. When the pressure test is completed, open the valve to the gas outlet, releasing the pressure, before opening the door.

7. Open the door of the chamber and screw up the top lid. Wear safety glasses and keep your face away.

8. Drain the water and dismantle the equipment. Wipe over with a cloth. Run gas through the pipes to remove water, and store safely.

Initial Installation

1. Check whether the inside of the cylinder is empty and clean. Wash and dry if necessary. Make sure no dust is inside before screwing the top and bottom lid onto the cylinder.

2. Fasten the probe and the connectors on the lids. Mount the measuring cell on the stand. Place in a suitable cabinet. Consider whether the stand should be fastened to the cabinet floor.

3. Install a pipe from the gas inlet out of the cabinet via a valve and onto the gas source. Install a pipe from the gas outlet out of the cabinet, via a valve and a pressure sensor, and out to a valve before placing it under a gas exhaust hood.

4. Place the coaxial cable from a vector network analyser (VNA) into the cabinet. The cable should be free, with no twists or pressure to it.

5. Calibrate the cable connected to the VNA with the Rhode Schwarz ZV-Z135 calibration kit. Hold the calibration kit in the same formation as it will be when it is connected to the cylinder, in order to get an accurate calibration.

6. See if the calibration is accurate by comparing the signal to a previous measurement if possible.
7. Screw the coaxial cable to the probe.
8. Make sure that all connections and screws are securely fastened and that the screws are screwed in securely. Close the cabinet.

Gas Measurements

Gas measurements can be performed several different ways, by increasing and decreasing the pressure or simply only decreasing the pressure. Severe hysteresis has not occurred previously. Check the maximum pressure on the gas source before deciding on the maximum pressure. The procedure applies to both gas connection to a wall socket and to a gas bottle.

1. Open the valve on the gas supply and fill the cavity to a pressure of 5-10 bar. Release the pressure. Repeat this 3 times to remove the air. Close the outlet valve.
2. Open the valve to the gas supply again and increase the pressure to the desired pressure.
3. Close the inlet valve and let the internal temperature settle by ensuring that the pressure is constant before continuing.
4. Start the pressure measurements and start the pressure log. Start the VNA measurements at the desired settings, taking singular or continuous measurements.
5. Let it sit until the desired amount of measurements has been reached, or start individual measurements.
6. Increase the pressure by opening the gas inlet valve and the gas supply until desired pressure or decrease the pressure by gently opening the gas outlet valve. Let the continuous measurements run or start the desired amount of individual measurements. Repeat this step for the wanted amount of pressure points.
7. After the last measurement has been finished, stop the pressure log and VNA measurements. Release the pressure by opening the gas outlet valve until the pressure measurements returns to atmospheric pressure. Let it stay open.
8. Open the cabinet door. Keep the cylindrical cavity intact, including the connected probe antenna and the gas connectors if new measurement series will be performed at a later time to avoid shifts in the resonance frequency.

Appendix C

Pressure Measurements

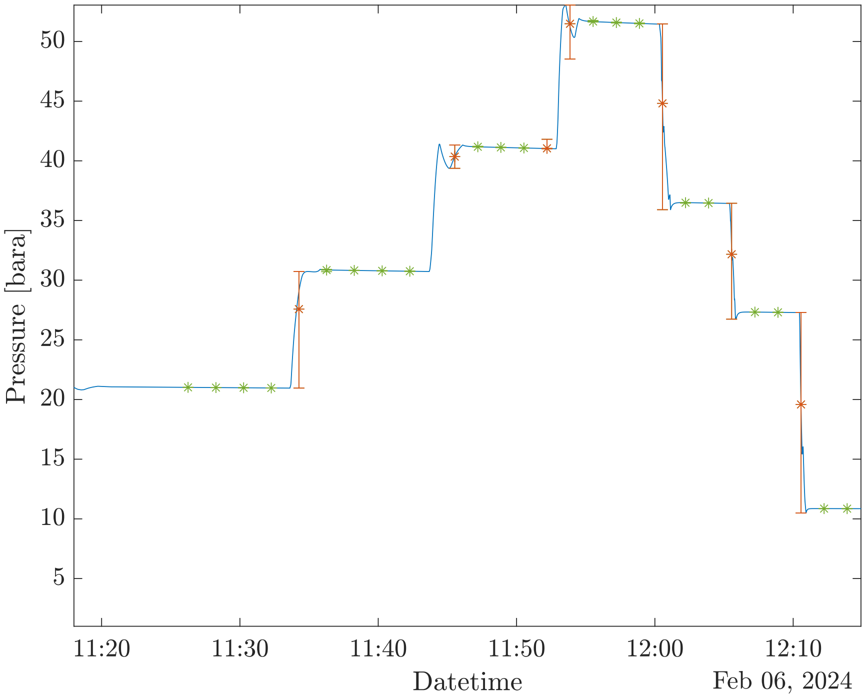

Figure C.1: Continuous pressure measurements of $N_{2,1}$ *(blue), and average pressure of measurements at half-time including error bars for minimum and maximum pressure with the included measurements (green) and the excluded measurements (red).*

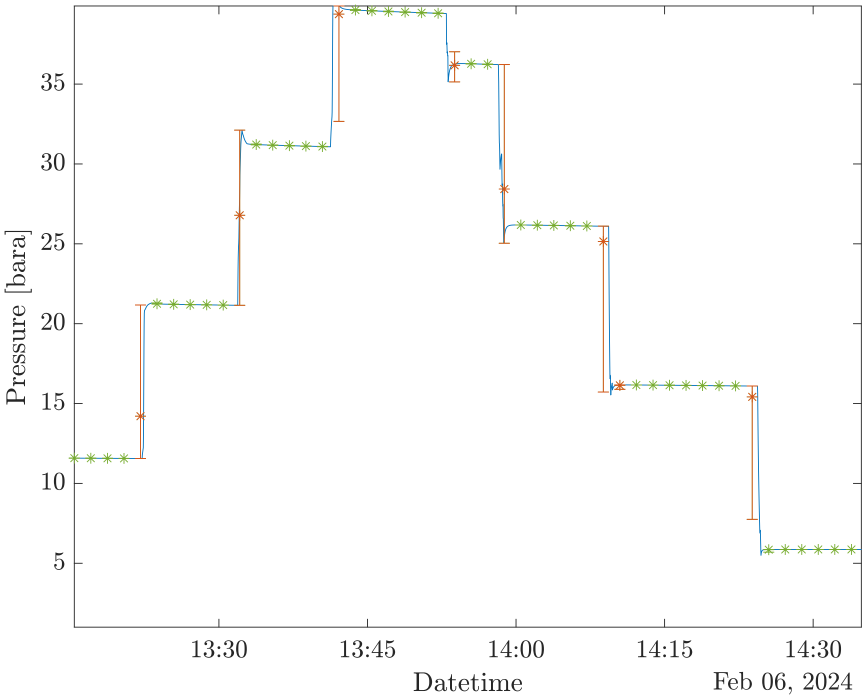

Figure C.2: Continuous pressure measurements of $CO_{2,1}$ *(blue), and average pressure of measurements at half-time including error bars for minimum and maximum pressure with the included measurements (green) and the excluded measurements (red).*

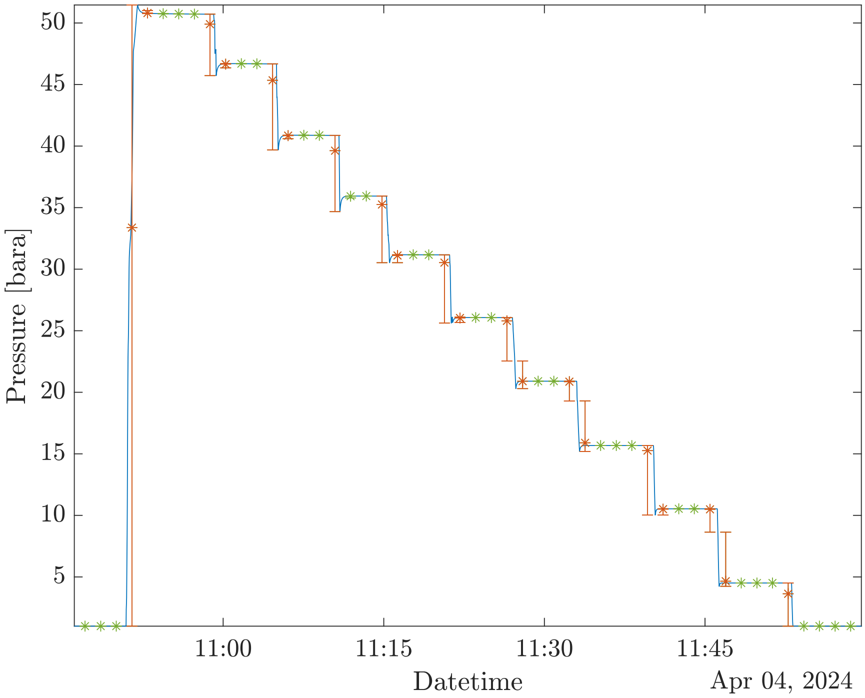

Figure C.3: Continuous pressure measurements of $N_{2,2}$ *(blue), and average pressure of measurements at half-time including error bars for minimum and maximum pressure with the included measurements (green) and the excluded measurements (red).*

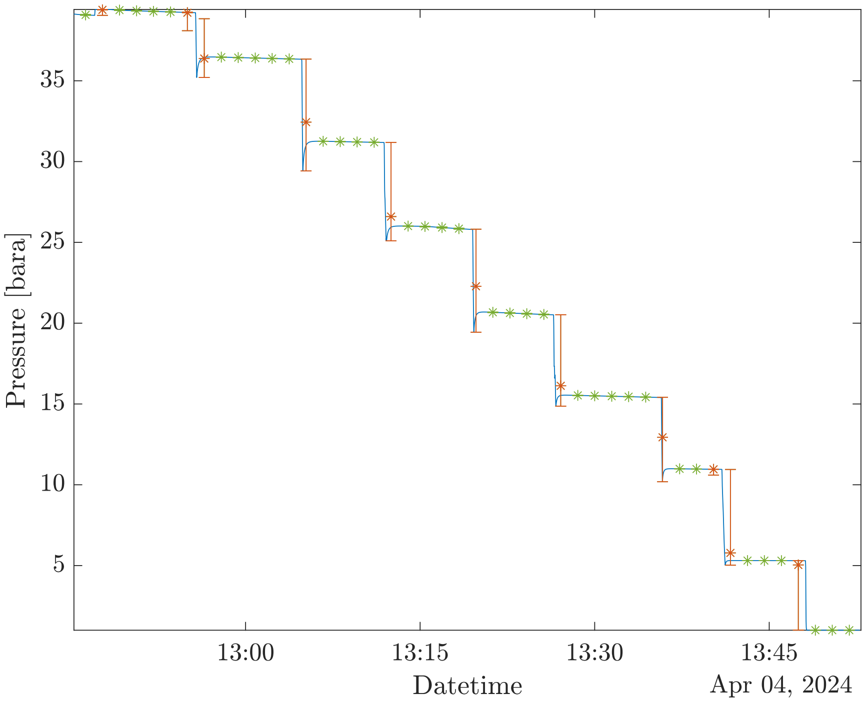

Figure C.4: Continuous pressure measurements of $CO_{2,2}$ (blue), and average pressure of measurements at half-time including error bars for minimum and maximum pressure with the included measurements (green) and the excluded measurements (red).

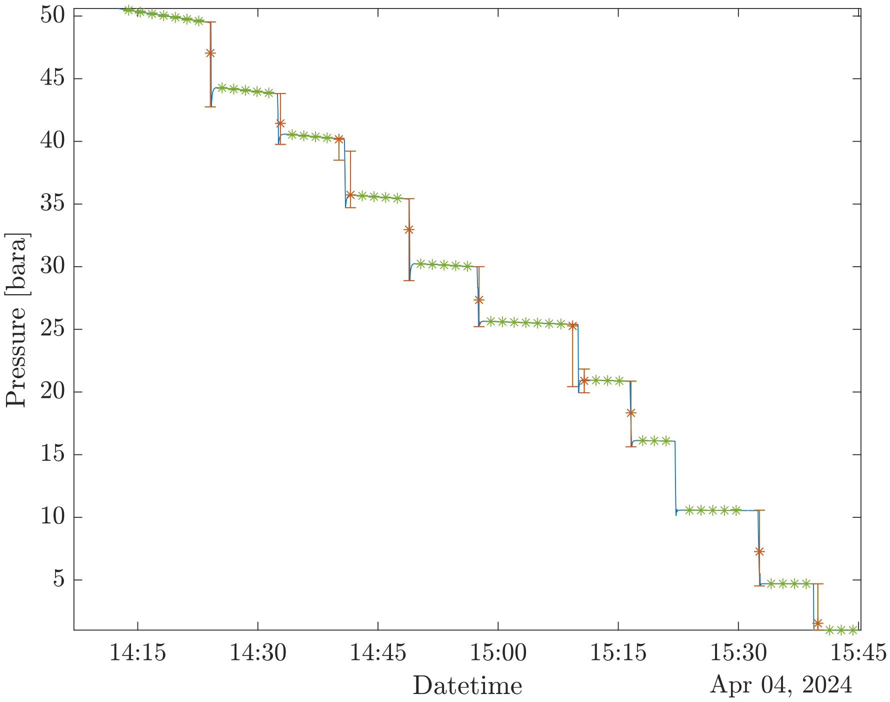

Figure C.5: Continuous pressure measurements of the N_2/CO_2 mixture (blue), and average pressure of measurements at half-time including error bars for minimum and maximum pressure with the included measurements (green) and the excluded measurements (red).

Appendix D

Reflection Coefficient Data

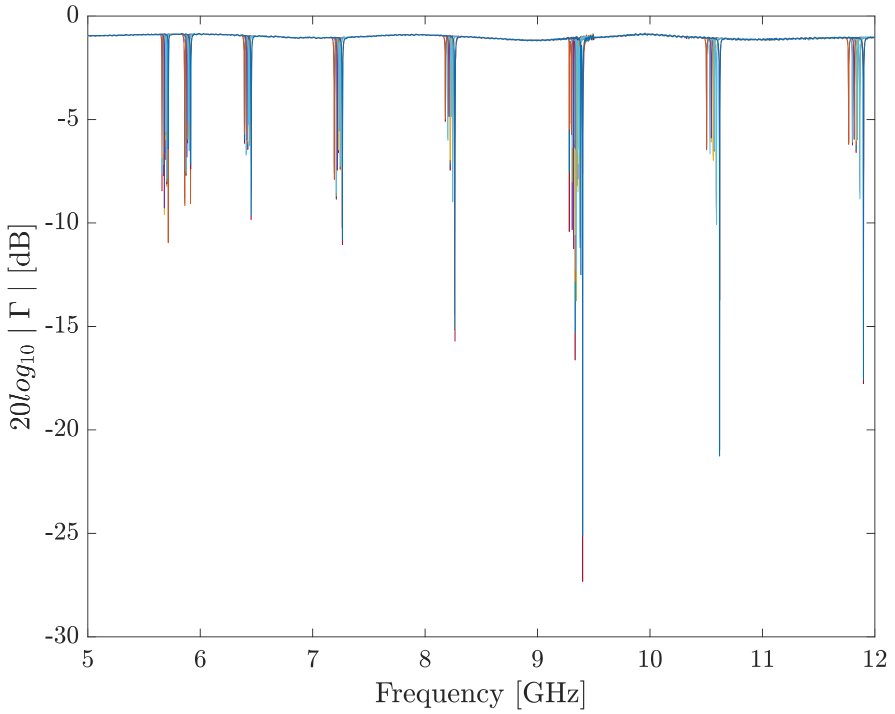

Figure D.1: Logarithmic reflection coefficient Γ *for* $N_{2,1}$ *measurements with stable pressure along the frequency range.*

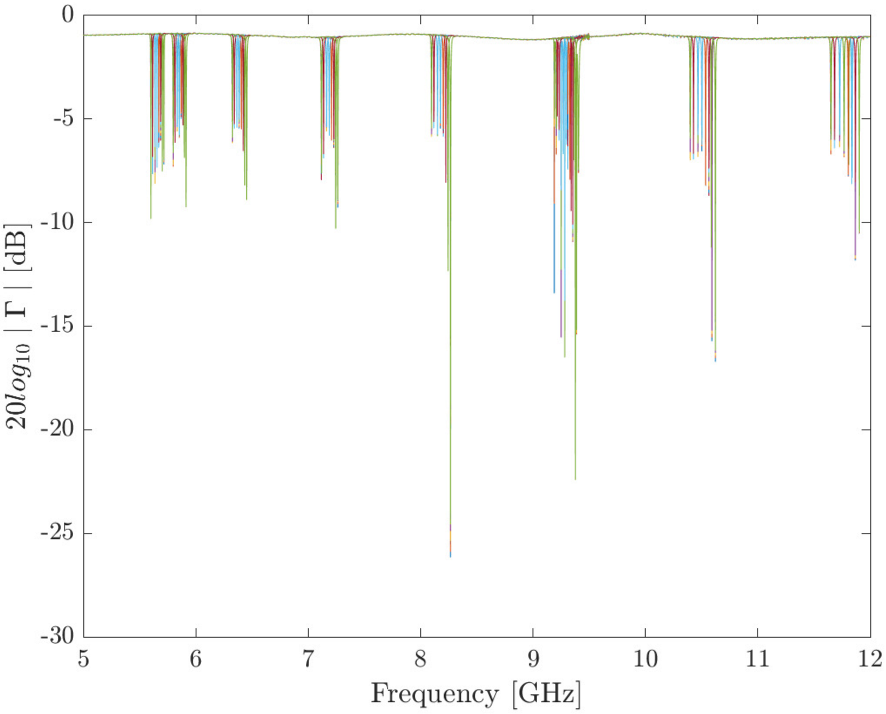

Figure D.2: Logarithmic reflection coefficient Γ for $CO_{2,1}$ measurements with stable pressure along the frequency range.

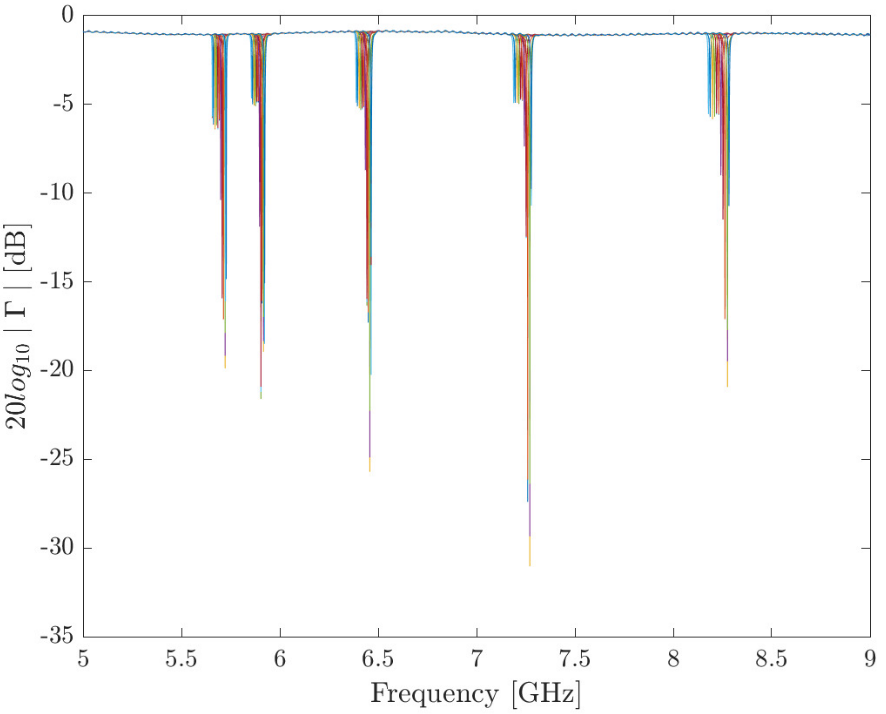

Figure D.3: Logarithmic reflection coefficient Γ for $N_{2,2}$ measurements with stable pressure along the frequency range.

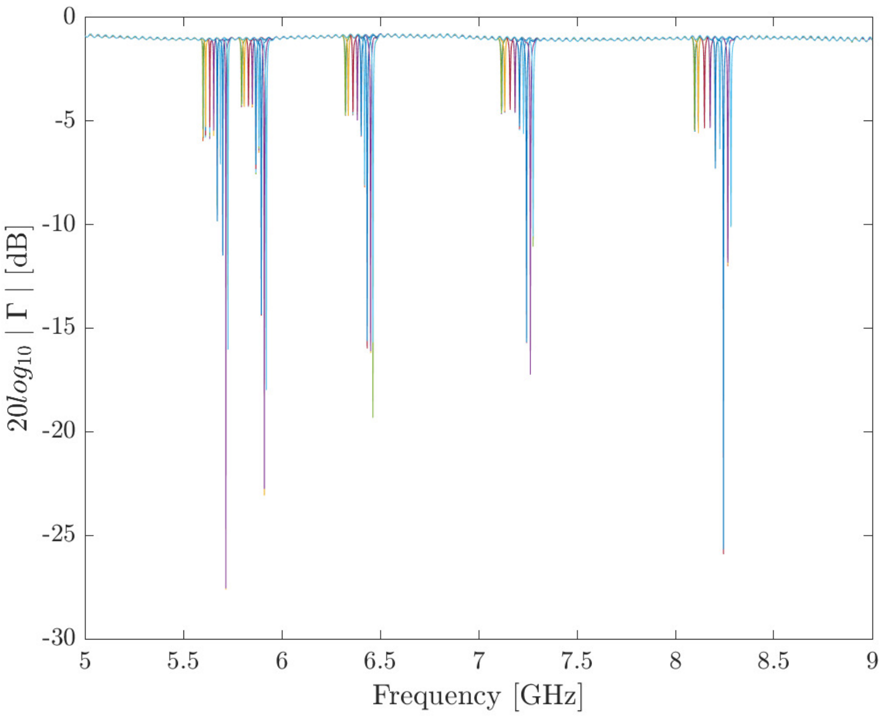

Figure D.4: Logarithmic reflection coefficient Γ for $CO_{2,2}$ measurements with stable pressure along the frequency range.

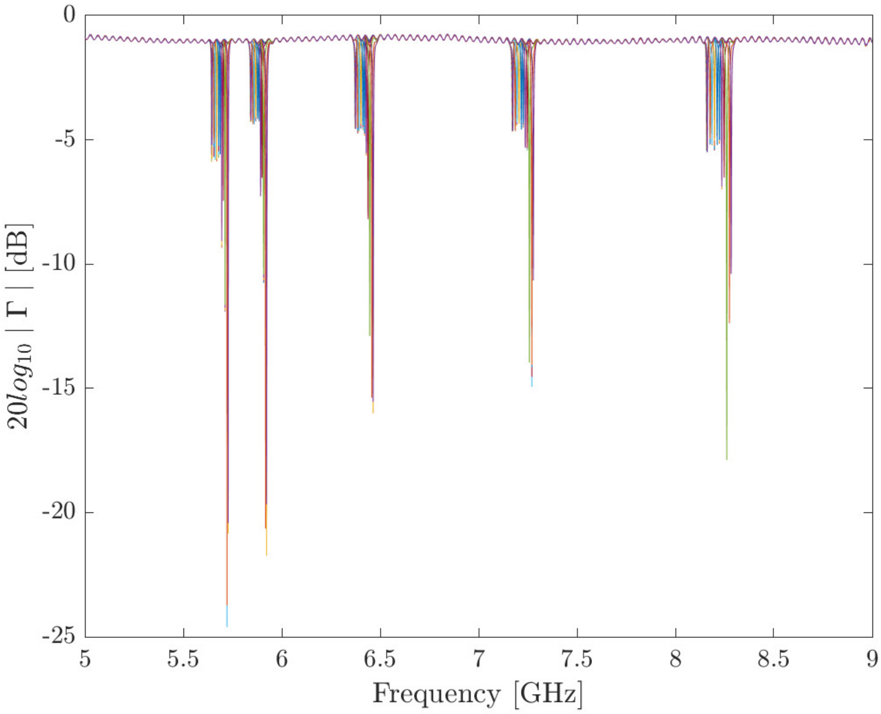

Figure D.5: Logarithmic reflection coefficient Γ for the N_2/CO_2 mixture measurements with stable pressure along the frequency range.

Appendix E

Narrow Reflection Coefficient Data

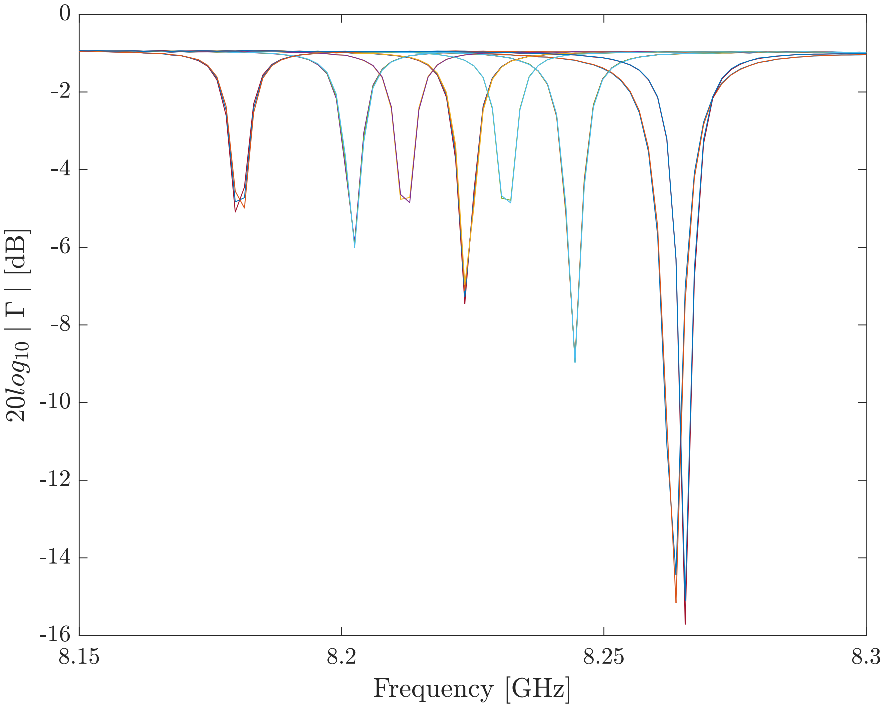

Figure E.1: Logarithmic reflection coefficient Γ *for* $N_{2,1}$ *measurements with stable pressure for a narrow frequency range, showing* TM_{014}.

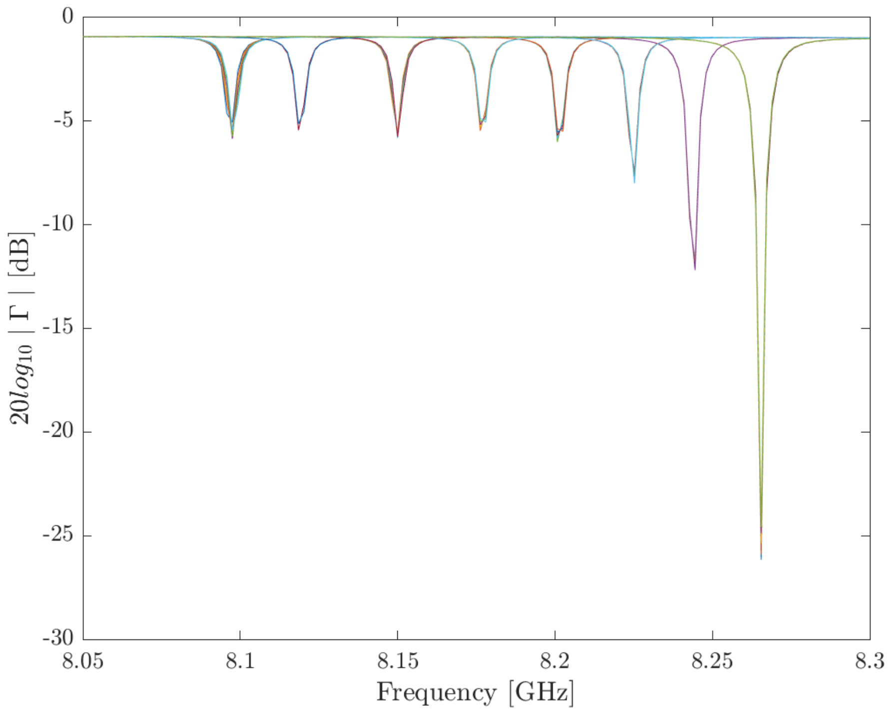

Figure E.2: Logarithmic reflection coefficient Γ *for* $CO_{2,1}$ *measurements with stable pressure for a narrow frequency range, showing* TM_{014}.

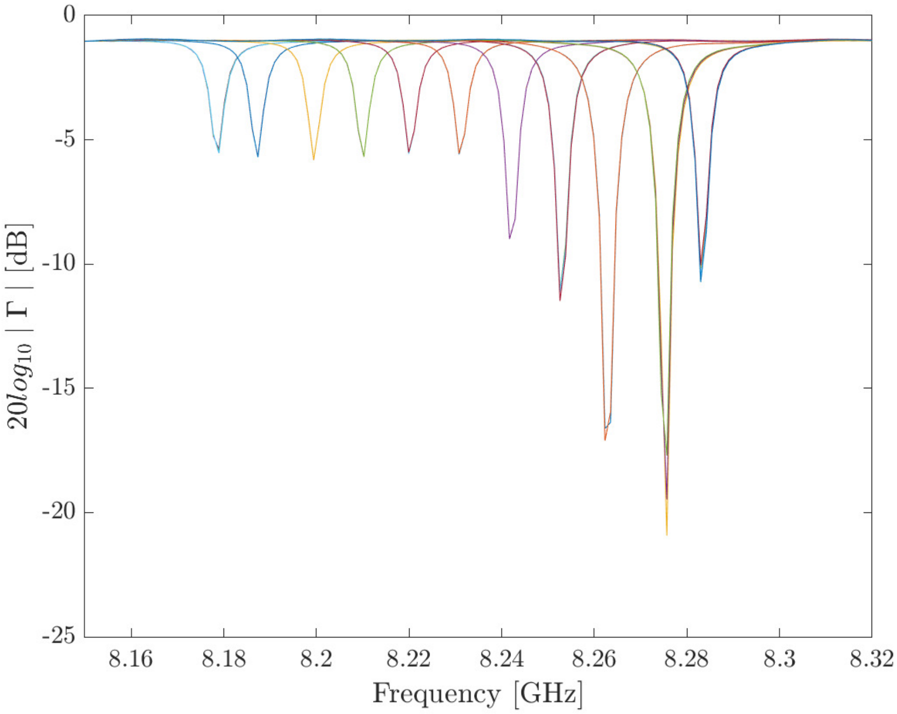

Figure E.3: Logarithmic reflection coefficient Γ *for* $N_{2,2}$ *measurements with with stable pressure for a narrow frequency range, showing* TM_{014}.

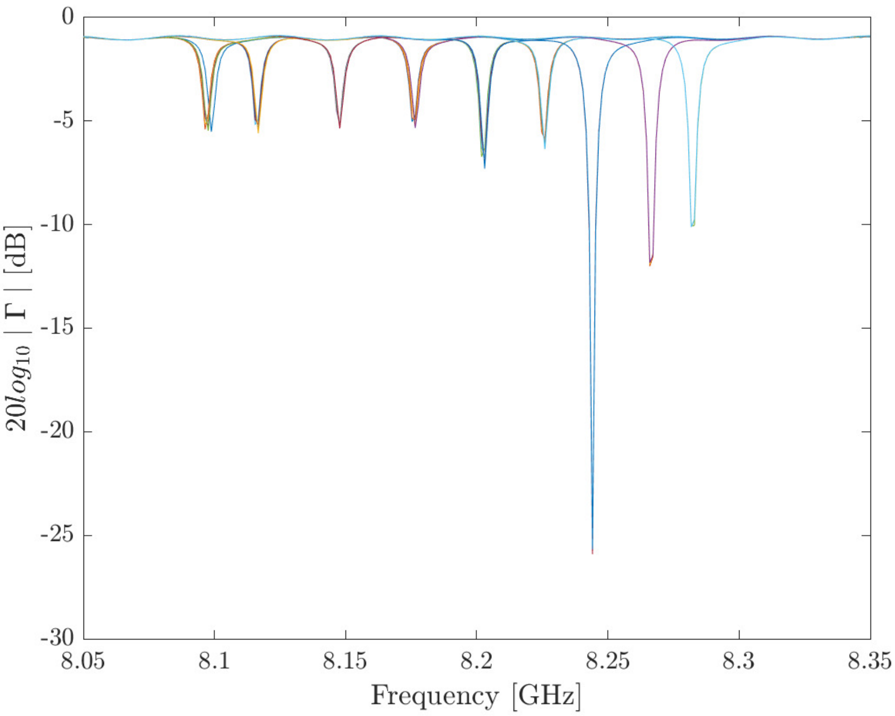

Figure E.4: Logarithmic reflection coefficient Γ for $CO_{2,2}$ measurements with stable pressure for a narrow frequency range, showing TM_{014}.

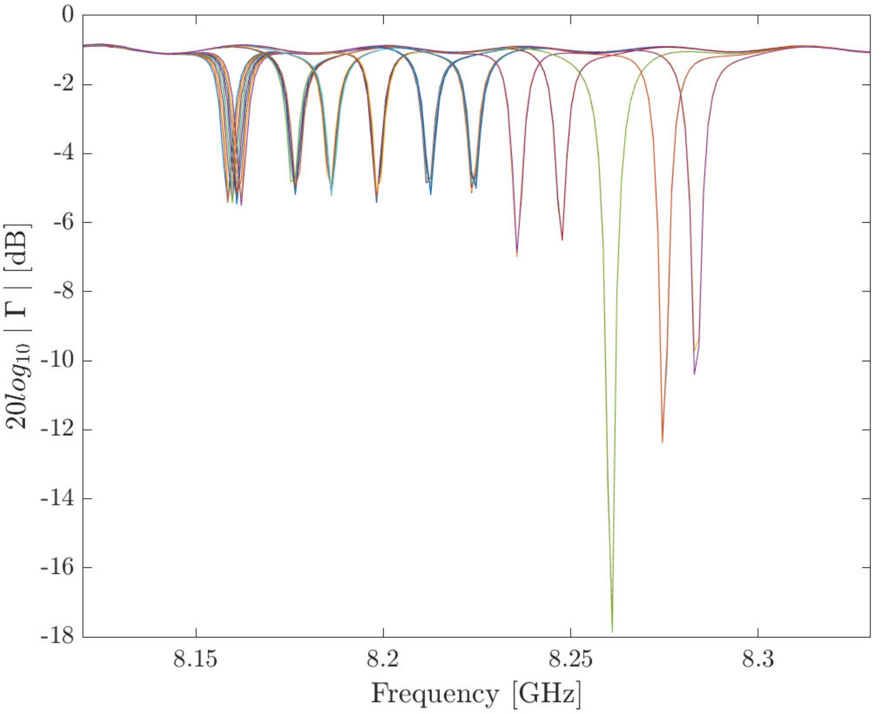

Figure E.5: Logarithmic reflection coefficient Γ for the N_2/CO_2 mixture measurements with stable pressure for a narrow frequency range, showing TM_{014}.